ENERGY EFFICIENCY AND MELT EJECTION ANALYSES OF A DUAL LASER MICROMACHINING METHOD

By

Osama Mohammad Awwad Alkhawaldeh

Thesis submitted to Loughborough University for the degree of

Doctor of Philosophy (PhD)

In the Wolfson School of Mechanical, Electrical and Manufacturing Engineering

2020

Dedication

This thesis is dedicated to my dad, mom, wife, children: Noor, Mohammad and Farah, brothers and sisters: Ali, Omar, Fatima, Asma, Nusaiba, Rufaida, Buthaina, Ahmed, Mustafa and Sara, as well as my late grandparents and my late aunt Mathail.

Acknowledgements

First and foremost, I would like to express my deepest thanks to my supervisors, Professor Jeremy Coupland and Dr Lewis Jones for their motivation, encouragement and support during my study. Without their patience and knowledge, this work would not have been achieved. Also, I thank my previous supervisor Dr Sundar Marimuthu. I truly appreciate the wonderful staff and colleagues at the Optical Engineering and Laser Lab for their help in the experimental setup especially to Mark Capers and Dave Britton. as well as for being good friends. I thank also the staff in Wolfson school and Material and Chemical Engineering Department especially to Jagpal Singh, Dawn Spencer, Samuel Davis, Scott Doak and Trevor Atkinson.

A special thanks to my wife, Basma, who has been with me every step of the way, support, patience and for her love. I am indebted to my dad, mum, grandmother (Shaikha), mother-in-law and brothers-in-law: Yousef and Jafer, for their help to continue my study.

Finally, I would like to thank my sponsor Muta University/Jordan for continuous funding me throughout my study.

Table of Contents

List of Figures

List of Tables

Abstract

This thesis is concerned with the understanding of a melt removal method which is based on combining a short laser pulse with the primary continuous laser beam called in this thesis dual laser micromachining (DLM). In this method, the continuous laser beam melts the surface and subsequently the short laser pulse ejects the molten material. In previous studies, this method has demonstrated improvements in material removal rates, however, there is a considerable range of results both in efficiency and quality. The energy consumed to produce the melt pool is the major part of the required energy budget in DLM (the sum of the energy consumed in melting and ejection processes). This important melting part has been ignored in the previous DLM studies. Moreover, there is still uncertainty in the melt ejection mechanism. This thesis considers the energy efficiency and quality characteristics also provides insight into the mechanism of melt ejection to facilitate its incorporation into the existing studies.

For the energy efficiency analysis, a contribution to the knowledge has been made through a combined analysis of theoretical and experimental result of the energy used in the DLM method. Theoretical calculations derived from a one-dimensional heating model has been performed for the melt pool size against the melting process parameters. The minimum energy required to remove the molten material was calculated from the surface energy at the liquid-solid interface that separates the liquid and creates new surfaces. It was found that the ejection energy can be considered to be negligible in comparison to the energy required to form the same mass of melt pool. Therefore, the energy model has focused on the melting process to optimise the DLM energy. The key finding was that the most efficient melting occurs at the maximum melt depth when the surface starts vaporises. The decrease in the energy required for the combined lasers is primarily due to the optimisation of the irradiation time in the melting process. At this most efficient melting process, the theoretical calculation has shown that there would be a reduction in total energy consumption of three times comparing DLM to practical conventional vaporisation found in the literature.

The relative energy efficiency of the DLM method has been demonstrated experimentally and compared to findings published in the literature. Two lasers were used, a continuous wave fibre laser to create a molten pool while a nanosecond pulse Nd:YAG laser was used to eject the molten material by vaporising the molten pool surface to generate recoil pressure. The experimental melt depths of the melting laser only were compared with the theoretical calculations. It was found that the experimental melt data align with the theoretical calculation

at low melting time values. However, after that, the experimental results depart significantly from the linear theoretical trend. The most efficient was found at experimental melting time 9 ms, however, it is less than the theoretical melting time of 15 ms. The DLM method created holes with 18-28 μm maximum depth from 20-31 μm maximum melt depths at melting times in the range of 9-60 ms at the same order. At optimised DLM method of 9 ms melting time, of the total energy, 95% of the energy was delivered in the melting process and 5% in the ejection. This key finding shows a good agreement between the experimental results with the theoretical calculation that predicted negligible energy required from ejection laser. The DLM result was compared to findings published in the literature. The results have shown that DLM method can increase material removal efficiency compared with the conventional processes by approximately 2 to 6 times. This comparison result confirms the theoretical reduction in total energy consumption of 3 times comparing DLM to vaporisation machining (ablation).

For the quality analysis, this thesis presents an analysis of the geometry and metallurgical features via sectioning and imaging of the DLM holes. Analysis of the material quality shows that were found free from microcracks and with a small amount of redeposited material at the workpiece surface along the periphery of the created hole. Moreover, the micrographs show low porosity in the solidified molten material.

Melt ejection mechanism results constitute a novel contribution in the field. It has been discovered that the material is ejected by the effect of the pressure pulse generated at the surface and travelled through the target material. This pulse is converted into a tension pulse at a certain position inside the melt pool as a result of mismatching from high to low impedance during travelling inside the material. Upon this tensile pulse, spallation can occur and eject the molten material that takes place when the tensile stress exceeds the tensile strength of the liquid material. The spallation of a laser-melted material by nanosecond laser pulse was studied experimentally and theoretically to find the magnitude and position of the tensile stress. DLM method was experimentally and theoretically demonstrated in different setup regimes. The key finding is that both the simulations and experiments showed the molten material is spalled by the tensile pulse close to the liquid-solid interface leaving behind a residual molten material along the bottom of the hole.

List of Abbreviation

CW: Continuous wave

DLM: Dual laser micromachining

ECM: Electrochemical machining

EDM: Electrical discharge machining

HAZ: Heat affected zone

MOPA: Master oscillator power amplifier

PRF: Pulse repetition frequency

TEM_{mn}: Traverse electromagnetic mode

Nomenclature

A	Area of the laser beam spot (m^2)
C	Specific heat capacity (J/kg K)
c	Speed of sound (m/s)
c_l	Speed of sound in liquid (m/s)
c_s	Speed of sound in solid (m/s)
E	Energy absorbed by the surface in the melting process $E = IA(t\text{-}t_m)$, (J)
E_0	Energy required to bring a surface area, A, to the melting temperature in the period $0 < t \leq t_m$, (J)
E_{eject}	Specific energy to eject the liquid material (the minimum specific energy required to overcome the surface energy) (J/kg)
E_m	Melting specific energy (lossless model) (J/kg)
E_{melt}	Melting specific energy (Cohen's model) (J/kg)
E_{melt_exp}	Specific energy for experimental melting (J/kg)
E_{melt_theory}	Specific energy for theoretical melting (J/kg)
$E_{milling}$	Specific energy of milling experiment (J/kg)
E_{pulse}	Absorbed pulse energy (J)
E_{total_exp}	Experimental specific energy for DLM method results (J/kg)
E_{total_theory}	Theoretical specific energy for DLM method, $E_{total\_theory} = E_{melt} + E_{eject}$ (J/kg), (J/kg)
E_v	Vaporization specific energy (J/kg)
F	Absorbed laser fluence (J/m^2)
I	Absorbed peak laser irradiance (W/m^2)
I_0	Peak laser irradiance (W/m^2)
$I_{absorbed\_eject}$	Absorbed irradiance of the ejection beam (W/m^2)
I_{eject}	Irradiance of the ejection beam (W/m^2)

I_x	Transmitted laser irradiance described by the Beer-Lambert law (W/m^2)
K	Thermal diffusivity (m^2/s)
k	Thermal conductivity at room temperature (W/m K)
k_1	Mean thermal conductivity in the liquid region (W/m K)
k_2	Mean thermal conductivity in the solid region (W/m K)
k_B	Boltzmann constant ($J.K^{-1}$)
L_l	FWHM pulse length in the liquid region (m)
L_m	Latent heat of melting (J/kg)
L_s	FWHM pulse length in the solid region (m)
L_v	Latent heat of vaporisation (J/kg)
l	Maximum DLM hole depth (m)
M	Molar mass (kg/mole)
m	Mass of melted material (kg)
N	Number of laser pulses
N_A	Avogadro constant (mol^{-1})
P	Absorbed laser power (W)
P_0	Laser power from the laser beam (W)
P_{amb}	Ambient pressure (Pa)
P_{max}	Maximum recoil pressure acts on the vapour-liquid interface at the centre of melt pool (Pa)
R	Radial coordinate from the centre of the Gaussian laser beam (m)
R_{pulse}	Pulse reflection coefficient
r_{eject}	Reflection coefficient of ejection laser
r_{melt}	Reflection coefficient of melting laser
S	Theoretical melt depth (Cohen's model) (m)
$[S]$	Dimensionless melt depth (Cohen's model)

S_{max}	Maximum melt depth before surface vaporisation (m)
T	Surface temperature (K)
$[T]$	Dimensionless surface temperature (Cohen's model)
T_0	Room temperature (K)
T_m	Melting temperature (K)
T_{pulse}	Pulse transmission coefficient
T_v	Vaporisation temperature (K)
t	Irradiation melting time (s)
t_a	Time of acoustic pulse from the ejection pulse start (s)
t_e	Electron cooling time (s)
t_i	Lattice heating time (s)
t_l	Laser duration pulse time (s)
t_{eject}	Ejection pulse duration (s)
t_{exp}	Experimental interaction time (s)
t_m	Time required for the surface to reach the melting temperature (s)
t_v	Time when the melt surface begins to vaporise (s)
V	Volume of the milled pockets (m^3)
w	Beam radius at a position where the intensity falls to $1/e$ times its maximum value (m)
X	Maximum melt depth for pressure pulse analysis (m)
x	Depth from the material surface (m)
Y	Ratio between latent heat of melting, L_m, to the specific energy required to raise the material temperature to melting temperature, $Y = L_m/(C(T_m\text{-}T_0))$
Z	Acoustic impedance ($Pa \cdot s/m^3$)
z	Maximum experimental melt depth (m)

Greek symbols

α	Material absorption coefficient (m^{-1})
γ	Surface energy (J/m^2)
$\Delta H_v(T_v)$	The vaporisation enthalpy at vaporisation temperature (J·mol/kg)
κ	Extinction coefficient
λ	Wavelength of the laser (m)
ρ	Material density at room temperature (kg/m^3)
τ	Ratio between the irradiation melting time, t, and the surface melting time, t_m, $\tau = t/t_m$

1 INTRODUCTION

1.1 Research Background and Motivation

Micro-machining is the process used to produce micro-parts or fabrication of micrometre-scale features with widespread application in sectors such as medical, aerospace, automotive, printing, and telecommunication devices (Gower, 2000; Rizvi and Apte, 2002; Muhammad *et al.*, 2010). A typical example of micro-machining is micro-drilling; used in industry to make cooling holes into turbine blades where traditional punching or twist drilling is problematic with difficult-to-machine materials leading to low machining quality and short tool life (Venkatesan, Ramanujam and Kuppan, 2014). These factors have motivated turbine blades manufacturers to find alternative methods such as electrochemical machining (ECM). However, ECM is limited to the minimum hole size of 750 μm, high costs due to tool wear, the expense of the consumables and low machining rates (Mcnally et al., 2013). For micro-milling, the challenge is to produce tools with less than 100 μm diameter, to have a high-quality finishing without burrs, and with very high quality in terms of surface roughness (Fleischer et al., 2004). Electrical discharge machining (EDM) provides this high-quality machining; however, like ECM, EDM is restricted by relatively low material removal rate (Kim et al., 2010).

Laser micro-machining provides a non-contact process, low machining costs and processing times, and a level of precision that makes them attractive for the manufacturers of micrometre-scale features (Dubey and Yadava, 2008). In addition to laser micro-drilling and micro-milling processes, high power lasers are exploited extensively in cutting and more recently turning a diverse range of materials like metals, ceramics and polymers (Mishra and Yadava, 2015). It must be remembered, however, that laser machining is primarily a thermal process in which melting and/or vaporisation are the dominant mechanisms of material removal. As a consequence, a significant proportion of the relatively high energy required for vaporisation is lost from the target area, reducing system efficiency and often producing a recognisable heat-affected zone (HAZ) (Sheng and Joshi, 1995; Madic and Radovanovic, 2012). The HAZ can influence the geometrical accuracy, change the microstructure of the material, including recast material, and in severe cases can lead to the formation of micro-cracks (Fu, Liu and Guo, 2015).

Formation of the HAZ is influenced by many parameters including laser power, focus, pulse frequency, feed rate and the number of repeat patterns (Genna *et al.*, 2010; Madic and

Radovanovic, 2012; Teixidor *et al.*, 2013). Laser micromachining using ultrashort pulsed pico- and femtosecond lasers have been shown to reduce thermal effects. In ultrashort micromachining, the pulse duration time is less than the lattice heating time. When the electron absorbs the photon energy, its temperature becomes significantly higher than the temperature of the lattice (since the electron specific heat is lower than for lattice). Ultrashort lasers, therefore, remove a layer of material equal to the optical skin depth by direct solid-vapour transition (sublimation). In this mechanism, the thermal diffusion is absent in the atomic lattice and therefore prevents the heat conduction of the substrate around the machining zone (Petkov *et al.*, 2008). However, the efficiency is less than expected (Leitz *et al.*, 2011) and even with optimised parameters, evidence of HAZ in thermal micro-machining processes are present even at femtosecond (Le Harzic *et al.*, 2005) pulse lengths.

In conventional laser ablation, the material is removed in its vapour phase. High energy is required to increase the material to its vaporisation temperature. Strategies exist to reduce energy input by removing the material in its melt phase instead of vaporisation such as gas jet (Farooq and Kar, 1998), waterjet (Tangwarodomnukun *et al.*, 2014), droplets (Ahn, Seo and Kim, 2012; López López *et al.*, 2016), and underwater processing (Kruusing, 2004).

Assist gas is used in laser drilling (Sarfraz *et al*., 2018) and laser cutting (Farooq and Kar, 1998) to decrease the specific energy of material removal. The assist gas is frequently supplied through nozzle coaxially with the laser beam to remove the molten material by increasing the shear forces on the liquid surface at low laser intensities. Oxygen and nitrogen are usually used as an assist gas in laser cutting. Oxygen reacts with metals in an exothermic reaction that decreases the specific energy but causes unwanted oxidisation that needs an extra process to remove. Nitrogen prevents oxidisation from occurring; it is less efficient than cutting using oxygen and more expensive than oxygen (Ghany and Newishy, 2005). In the non-reactive case, at high irradiance, the assist gas can usefully remove the vapour that can obstruct part of the laser beam energy (Dahotre and Harimkar, 2008) and at lower irradiance, can eject the molten material created by laser and decrease the specific energy of material removal (Farooq and Kar, 1998; Sarfraz *et al.*, 2018).

Liquid-assisted laser processes have demonstrated reductions in HAZ (Muhammad *et al.*, 2010) and recast (López López *et al.*, 2016) compared to dry laser machining. However, these processes can introduce contaminants into the workpiece, or, as with the case of underwater machining, present severe limitations to the practicality of processing.

An alternative method of assisted ejection that overcomes some of these deficiencies, proposed and demonstrated experimentally by Fox (1975), is to combine two lasers; first to melt the surface and subsequently eject the molten material. In the following work, this method will be referred to as dual laser micromachining (DLM). Fox found a decrease of irradiation time by more than a factor of two in addition to the enhancement in the quality compared to using continuous wave (CW) only. Other DLM experiments have demonstrated improvements in material removal rates in stainless steel by up to an order of magnitude (Lehane and Kwok, 2001; Walther, Brajdic and Kreutz, 2008; Wang *et al.*, 2017). However, there is a considerable range of results both in efficiency and quality. The energy consumed to produce the melt pool is the major part of the required energy budget in DLM (the sum of the energy consumed in melting and ejection processes). This important melting part has been ignored in the previous DLM studies. This thesis considers the energy efficiency through studying an energy model of the DLM method. This model focuses on the energy consumed to produce the melt pool. Moreover, comparing the DLM results with the findings published in the literature.

In addition to energy efficiency, it is important to understand the melt ejection mechanism produced by the ejection laser. The melt ejection mechanism in DLM method was investigated theoretically by Robin and Nordin (1976), Shui (1978) and recently by Yuan *et al.* (2018). Robin and Nordin estimated the minimum impulse required from ejection laser suggesting that low energy short pulses should be capable of melt ejection and above this value of peak irradiance the difference in the impulse response of different materials is insignificant (Phipps et al., 1988). Another model using Bernoulli equation based on conservation of energy was developed by Shui (1978) to estimate the pressure, effective time and specific impulse to achieve specific melt removal fraction from the molten material produced by CW laser. An unrealistic large pressure and impulse for melt ejection are predicted by Shui's model that contradicts Robin and Nordin's model and Fox's experiment.

Recently, Yuan et al., (2018) studied the influence of the spot size combination on the micromachining morphology in the DLM method which provides further insight into the melt ejection problem. Their results showed that the molten material is ejected when the ejection pulse diameter is larger than the melt pool diameter which is consistent with Fox's experiment. On the other hand, when the ejection pulse diameter is smaller than the melt pool diameter, the molten material is accumulated around the hole edges. These results contradict with the assumption made by Robin and Nordin for the ratio between the two laser spot sizes.

Yuan et al. investigated the ejection using a shadowgraph technique showing the shockwave on the melt surface that generates the recoil pressure causing the material migration. This shockwave is generated by the plasma created during the melting process that expands rapidly by the action of ejection nanosecond laser. The images show strong turbulence on the surface when the nanosecond laser covers the entire molten pool surface and the recoil pressure confines the melt flow to the sides. However, the images do not show the ejected molten material. The mechanisms involved in melt ejection using DLM method are rather complex and are at present poorly understood and there is still uncertainty in the ejection models. This thesis provides insight into the mechanism of melt ejection to facilitate its incorporation into the existing studies through studying the effect of compressive pulse generated at the melt pool surface that is converted inside the melt pool as a tensile pulse resulting in melt ejection.

1.2 Research Aim and Objectives

This thesis aims to improve our understanding of the DLM method and compare its performance with conventional laser micromachining methods.

Specific objectives are:

1. To construct a theoretical model of laser micromachining by i) vaporisation (ablation) and ii) the combined melting and ejection in DLM method, initially neglecting the effects of heat loss to the HAZ using a one-dimensional conduction model.
2. To demonstrate and compare the relative energy efficiency of DLM and laser ablation through experimentation and comparison to findings published in the literature.
3. To assess the quality of the DLM method using metallurgical techniques to show the effect of DLM on the machined workpiece.
4. To investigate the physical mechanism for the melt ejection through theoretical analysis and experimental results to provide insight into this mechanism.

1.3 Thesis Outline

Chapter 2 presents the background of laser fundamentals. A summary of the basic principles of laser operation and a background account of laser-material interaction are presented. Laser material micromachining and the defects in the machined workpiece are explained. This is followed by a detailed literature review of the state-of-the-art in the strategies used to reduce laser energy input and quality, including the previous work on the DLM method.

Chapter 3 presents the development of the theoretical energy model for the DLM method. This model focuses on the energy consumed to produce the melt pool as the most significant part of the required energy budget in DLM. The theory of the melting process is studied using a one-dimensional heat conduction model. The specific energy theoretically required for total material removal in the DLM method is calculated and compared with conventional laser vaporisation (ablation).

Chapter 4 presents the experimental investigation of the DLM method and shows an improvement in material removal efficiency compared to conventional laser micromachining. The chapter begins with a conventional laser milling experiment and laser micromachining research found in the literature to identify the specific energy of conventional laser micromachining. The chapter presents the results of surface treatment using the melting laser only, the ejection laser only, and both lasers combined in the DLM method. Details of the experimental setup and analysis technique are explained. An initial pilot "moving mode" experiment is undertaken for the DLM method in a more accessible set up to ensure the applicability of the DLM method in melt ejection. Then the DLM method is studied in a more controlled "stationary mode", setup with the energy analysis as well as the machining quality analysis using metallurgical techniques. The results of the melting process only at stationary mode are compared with the theoretical melting energy results from Chapter 3. The material removal efficiency of DLM is compared with the results from the literature of the conventional processes for similar material.

In Chapter 5, the physical mechanism for the melt ejection is studied. The chapter starts with the literature of the melt ejection mechanism in the DLM method. A hypothesis is introduced for the melt ejection by the effect of the acoustic pulse pressure generated by rapid surface vaporisation. Theoretical analysis and simulation of the acoustic pulse are conducted. The hypothesis is tested by conducting DLM in different experimental setups: by introducing the ejection pulse at the molten pool surface; on the solid back surface of a thin workpiece. Sectioning of the melt pool and machined workpiece features provides some useful insight into the ejection mechanism. The behaviour of ejected melt material is studied using high-speed camera imaging. This chapter presents a new contribution to the field of laser melt ejection.

Chapter 6 concludes the results obtained from the analysis of the energy and melt ejections mechanism for DLM method and the main contribution to the knowledge. The limitations and recommendations for possible future work are also addressed.

2 LITERATURE REVIEW

This chapter introduces a brief review of laser fundamentals, including the operating principles, components of a laser and review of the fundamentals of laser micromachining. As the major topic of the thesis, the literature concerning material removal mechanisms will be discussed in detail. Different mechanisms of melt ejection are explained and previous experimental work relevant to the DLM method is presented.

2.1 Laser Fundamentals

2.1.1 Basic Principle of Laser Operation

LASER is an acronym for Light Amplification by Stimulated Emission of Radiation. There are three processes involved in producing the laser: population inversion, stimulated emission and amplification.

When an electron absorbs energy from a light source (photon), the electron will be excited to a higher discrete energy level in a process called population inversion. The energy of the absorbed photon equals the energy difference between the levels. Population inversion in lasers generally involves three or four energy levels. Taking three energy level design (E_0, E_1 and E_2) as an example, the photon energy is first absorbed by the atom. The photon has enough energy to pump the electron from ground level E_0 to the energy level E_2. Shortly afterwards, the electron rapidly decays into the metastable energy level E_1 without any radiation.

However, after a very short time, the excited electron will decay to a lower energy level by emitting a photon equals the energy difference between the levels in a process called spontaneous emission. When the atom absorbs a photon, and after a short time another photon is absorbed, stimulated emission will be the result. The newly created photon has the same phase, frequency, polarisation and direction of travel as another photon.

A typical laser system consists of a gain medium material in solid (e.g. Nd:YAG), liquid (e.g. dye) or gas (e.g. CO_2) states and the pump source which can either be in the form of a flash lamp or a diode laser or an electrical discharge mechanism. A pair of mirrors with high reflectivity is used to bounce the light between them passing through the gain medium to be amplified each time, resulting in a high-intensity laser beam. The mirrors are a totally reflecting back mirror and a partially reflecting front mirror to let the light to escape.

Laser radiation ranges from ultraviolet to far-infrared with properties of monochromaticity, directionality, coherence and high energy density. Since high power lasers were first demonstrated in the late 1960s, they have been used in a wide range of applications such as metrology and material processing.

2.1.2 Spatial Modes

The cross-section of the laser beam can be described by its traverse electromagnetic mode (TEM_{mn}), where m and n are integer numbers represent the number of vertical and horizontal nodes in the direction orthogonal to the direction of the propagating beam. In this thesis, the lasers used have the fundamental mode TEM_{00} with an approximately Gaussian spatial distribution of the beam irradiance as given by (Russel L. McCally, 1984),

$$I_{(R)} = Ie^{\frac{-R^2}{w^2}} \tag{2-1}$$

where I is the peak absorbed irradiance at the centre of the laser beam given in Equation (2-2), R is the radial coordinate from the centre of the Gaussian laser beam, and w is the beam radius at a position where the intensity falls to $1/e$ times its maximum value.

$$I = \frac{P}{\pi w^2} \tag{2-2}$$

where P is the total absorbed power from the laser beam.

2.1.3 Pulse Duration

Lasers can be operated either in CW or pulsed mode. In the CW, constant laser energy is discharged for a long time. Pulsed outputs are produced by different techniques, such as power switching of stored CW in pulse duration up to milliseconds or Q-switching when the population inversion reaches maximum level allows the switch to open and deliver an intense and regular pulse beam in pulse duration as short as a nanosecond. For ultrashort pulse pico- and femtosecond durations, the mode-locking technique is used.

Each pulse delivers specific energy to the processed material as a function of peak power and pulse duration in the range of milliseconds (ms), microseconds (μs), nanoseconds (ns), picoseconds (ps) and femtoseconds (fs).

2.1.4 Laser Irradiance and Laser Fluence

Laser irradiance (I) is defined as the measurement of absorbed laser power (P) per area of the laser beam spot (A):

$$I = \frac{P}{A} \tag{2-3}$$

Laser fluence (F) is the measurement of absorbed pulse energy (E) per A:

$$F = \frac{E}{A} \tag{2-4}$$

Laser irradiance (I) and laser fluence (F) are essential in determining the machining process and accordingly the amount of the machined volume and the thermal damage (Dubey and Yadava, 2008), as will be explained later in this thesis.

2.1.5 Types of Lasers

Lasers are generally classified into three main types depending on the state of the active medium used: solid, liquid and gas. In this research, fibre and Nd: YAG lasers were used. A fibre laser is a solid-state laser doped with rare earth elements of Erbium (Er), Ytterbium (Y), and Neodymium (Nd) in a glass using a diode laser as a pumping source. The wavelength of the fibre laser used here is around 1.070 μm. An Nd: YAG (neodymium-doped yttrium aluminium garnet) laser is one of the most common lasers used in micromachining. Nd:YAG lasers emit light with wavelength such as 1064 nm but can be doubled, tripled or quadrupled in frequency to wavelengths, 532, 355 or 266 nm. Fibre and Nd: YAG Lasers can be operated either in continuous CW or pulse mode. In this research, the fibre laser will be used in both modes while Nd: YAG will be used in only pulsed mode.

2.2 Laser Material Interaction

When the laser beam reaches the material surface, the energy will be divided by the processes of reflection, transmission, scattering, and absorption. An absorbed photon generally excites free electrons in the material and produces heat (Meijer, 2004). The absorbed irradiance by opaque material I reduces to the transmitted laser irradiance I_x (*i.e,* $1/e^2$ times I) as described by the Beer-Lambert's law (Swinehart, 1962):

$$I_x = Ie^{-\alpha x} \tag{2-5}$$

where α is the material absorption coefficient (m^{-1}) given in Equation (2-6) where $1/\alpha$ is absorption length or the skin depth of optical penetration and x is the depth from the material surface (m).

$$\alpha = \frac{4\pi\kappa}{\lambda} \tag{2-6}$$

where κ is the extinction coefficient and λ is the wavelength of the laser.

For the 316 stainless steel used in this research, the value for iron was taken (highest content in 316 stainless steel) with an extinction coefficient, κ, of 2.9179 and 3.9977 for 532 and 1064 nm wavelengths (Johnson and Christy, 1974) resulting in skin depths, $1/\alpha$, to be 14.5 and 21.2 nm, respectively. This penetration depth is important in surface material modification, as the surface is to be altered without affecting the bulk of the material (Sugioka, et al., 2010).

Laser material interaction is governed by the characteristics of electromagnetic radiation emitted by the laser and the thermophysical properties of the material. The laser characteristics are the wavelength, angle of incidence, polarisation and irradiation time. The thermophysical properties of the material are the absorptivity, thermal conductivity, density, and specific heat capacity.

The absorptivity of metallic surfaces is a function of the laser wavelength (Indhu et al., 2018), as shown in Figure 2-1. Despite Nd: YAG laser of 1.064 µm wavelength generally having a higher absorptivity than a CO_2 laser of 10.6 µm wavelength, the CO_2 laser is widely used due to its relatively lower cost (Ghany, Rafea and Newishy, 2006). Bergstrom, Powell, & Kaplan (2007) stated that the for stainless steel the absorptivity increases with the increase in S_a roughness values above 1.5 µm. High absorption efficiency leads to a higher material removal rate which can be increased by changing the surface finish (Pham *et al.*, 2002). The absorptivity also depends on the temperature and phase of the metal such that the absorptivity increases with the surface temperature as can be seen in Figure 2-2 (Xie *et al*., 1997). The absorptivity values for the two lasers and stainless steel used in this research will be presented in the following chapter.

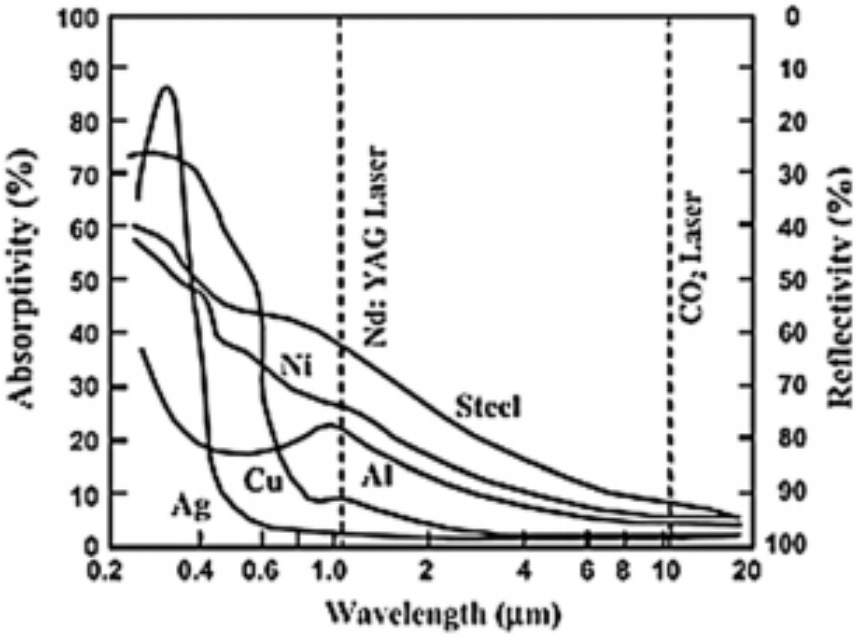

Figure 2-1 Absorptivity and reflectivity of a selection of metals as a function of wavelength (Indhu et al., 2018)

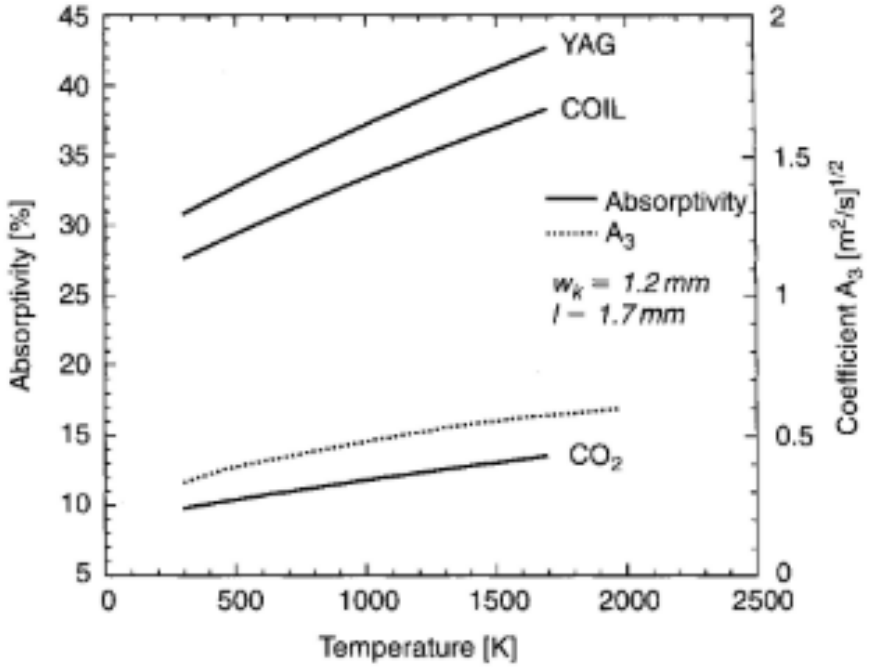

Figure 2-2 Absorptivity of CO2 (10.6 μm), chemical oxygen-iodine laser (COIL) (1.315 μm) and Nd:YAG (1.06 μm) lasers for 304 stainless steel as a function of temperature (Xie et al., 1997)

The optical energy is transformed into thermal energy followed by heat conduction from the surface of the material. The energy transferred to the material defines the temperature distribution inside the material. This heat is diffused from the surface to the bulk material.

The depth of diffusion is given by $d = (4Kt)^{1/2}$ where K is the thermal diffusivity and t is the irradiation time (Thompson, Ren and Parel, 1992).

As defined in the previous chapter the ultrashort lasers remove a layer of material commensurate to the optical skin depth by a direct solid-vapour transition (sublimation) without heat conduction inside the substrate around the machining zone (Petkov et al., (2008).

Laser-material interaction is divided into three stages. Firstly, the solid material is heated with no melting or vaporisation. Secondly, as time increases the absorbed energy makes the surface of the material start melting at the centre of the beam where the temperature is the highest. During the second stage, a solid-liquid interface is formed. The interface propagates into the material until reaching the third stage when the surface starts to vaporise. Further, the ionisation of vapour may generate plasma above the substrate surface during the laser-material interaction. The locations of the interfaces depend on the irradiance and the irradiation time (Zhang and Faghri, 1999). The schematic diagram in Figure 2-3 shows the various effects of laser-material interactions (Dahotre and Harimkar, 2008). Figure 2-3e shows the material removed after the action of the laser. In this conventional laser process, the material is removed via vaporisation and melt ejection. The molten material is ejected by the effect of recoil pressure generated by surface vaporisation. The energy needed to vaporise the material is about three times that required to melt the same mass. This means if the material is melted and then is ejected by mechanical means, the energy required to remove the material will be reduced. Although conventional process showed a contribution of melt ejection in the material removal, still, part of the energy is consumed in the vaporisation. In this thesis, in the upcoming work, a method is used to remove the material in its liquid phase without the need to supply the latent heat of vaporisation.

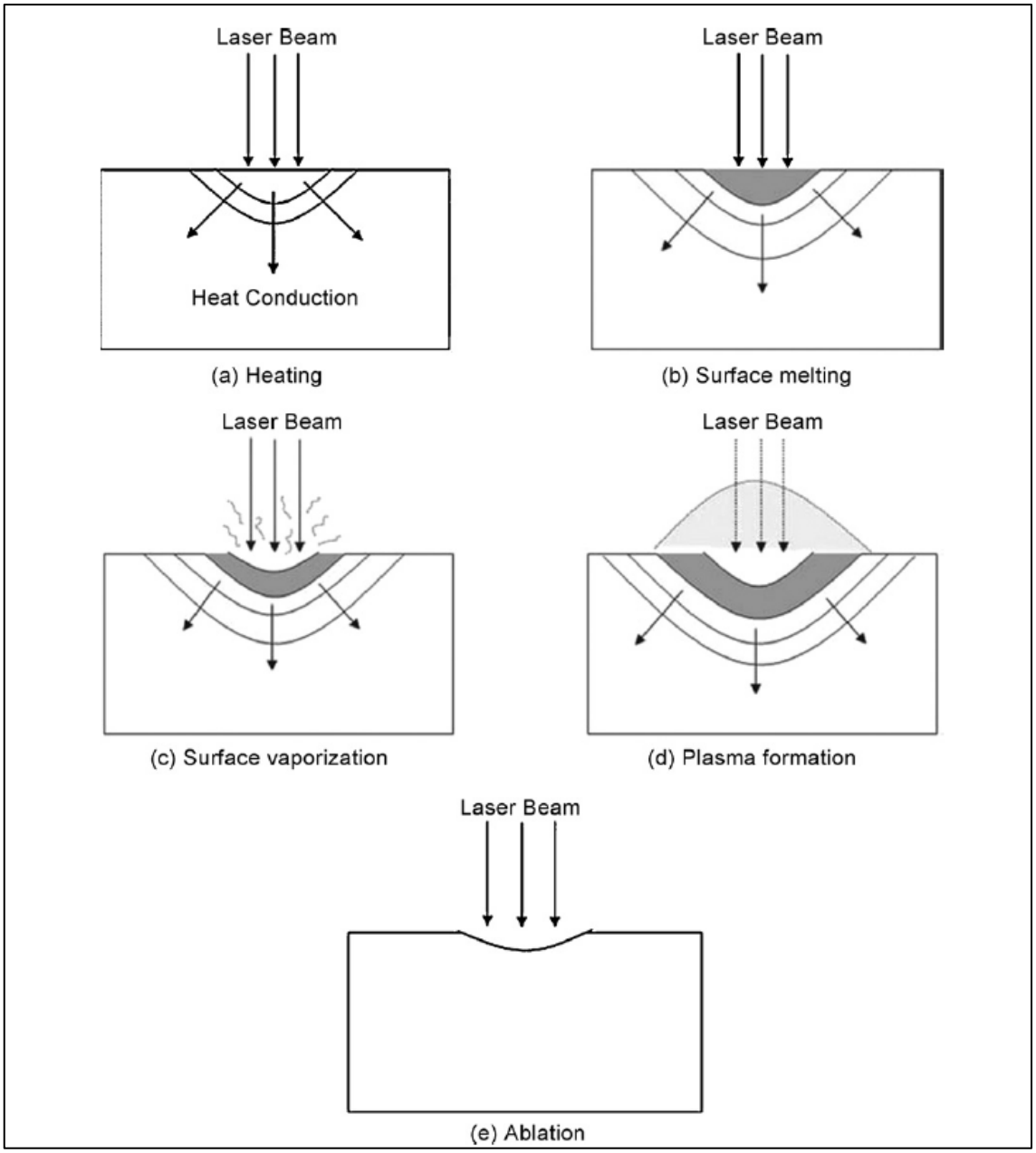

Figure 2-3 Physical phenomena during laser micromachining (ablation) (Dahotre and Harimkar, 2008)

Lasers are exploited extensively in material processing as a non-contacting means to alter the material properties, weld, cut, mill and drill a diverse range of materials (Mishra and Yadava, 2015). The range of possible laser processes as a function of irradiance (power density) and interaction time is illustrated in Figure 2-4.

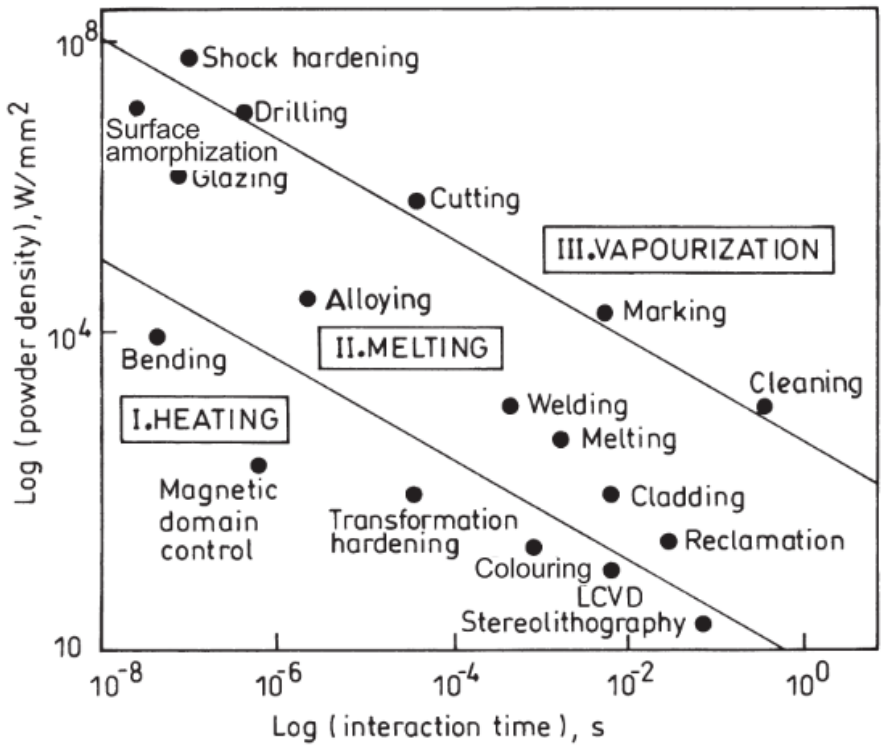

Figure 2-4 Range of processes mapped against irradiance (power density) and interaction time (Majumdar and Manna, 2003)

Lasers are used with a long-time duration and low irradiance (power density) in cladding and welding processes to deposit and join materials, respectively. On the other hand, with high irradiance (power density) and relatively short irradiation time, the laser can be used to remove material via rapid vaporisation and melt ejection to cut or drill the workpiece.

This thesis investigates laser melting and laser micromachining with different irradiance (power density). The melting process is conducted at an irradiance of 350 W/mm^2 with up to a few tens of milliseconds irradiation time in CW mode using fibre laser. This power density and irradiation time is in the melting range defined in Figure 2-4. An irradiance of 1×10^8 W/mm^2 is used in this research for the 5 ns Nd: YAG melt ejection laser and 1-3 $\times10^7$ W/mm^2 using fibre laser in pulse mode at 9-115 ns irradiation time for conventional milling experiment as will be explained in detail in the following chapter. These irradiances at their irradiation times are located approximately on the vaporisation line in Figure 2-4 and will be explained later in detail in this thesis.

2.3 Laser Micromachining (Ablation)

2.3.1 Material Removal in Laser Micromachining (Ablation)

From the previous section it is clear that when the irradiated material is heated first to the melting point and then to vaporisation point, the material can be removed in the vapour or liquid phase or more generally a combination of the two (Dubey and Yadava, 2008). In conventional laser micromachining with a single laser, the pulse (of a few nanoseconds duration) is relatively intense and short, the rapid vaporisation of a thin surface layer in the material generates a recoil pressure that ejects a thin layer of the molten material away (Knight, 1979). It is generally accepted that melt ejection is influenced by the effect of surface tension gradient and mainly by the recoil pressure (Von Allmen, 1976; Chan and Mazumder, 1987; Solana *et al.*, 2001). The ejection occurs when the applied force, generated by the recoil pressure, is significantly higher than the surface tension force (Basu and DebRoy, 1992). Chan and Mazumder (1987) used a mathematical model to analyse the evaporation and melt ejection rates in metals when subjected to intense surface heating. It was found that melt ejection is the dominant mechanism of material removal at low laser irradiance. While at very high laser irradiance, vaporisation is the dominant material removal mechanism. The rate of material removal as liquid or vapour calculated in Chan and Mazumder's model is shown in Figure 2-5 and Figure 2-6 for aluminium and superalloy, respectively. In these figures, the total removal rate equals the sum of the vaporisation rate and the melt ejection rate.

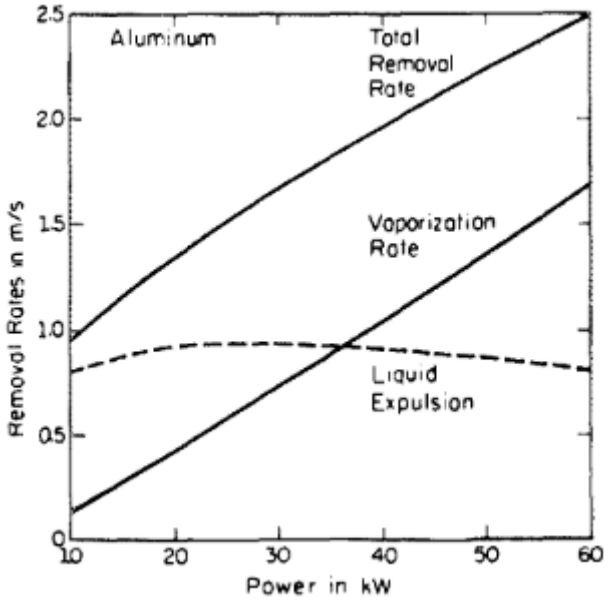

Figure 2-5 Vaporisation, liquid expulsion and total material removal rates for aluminium versus laser beam power (Chan and Mazumder, 1987).

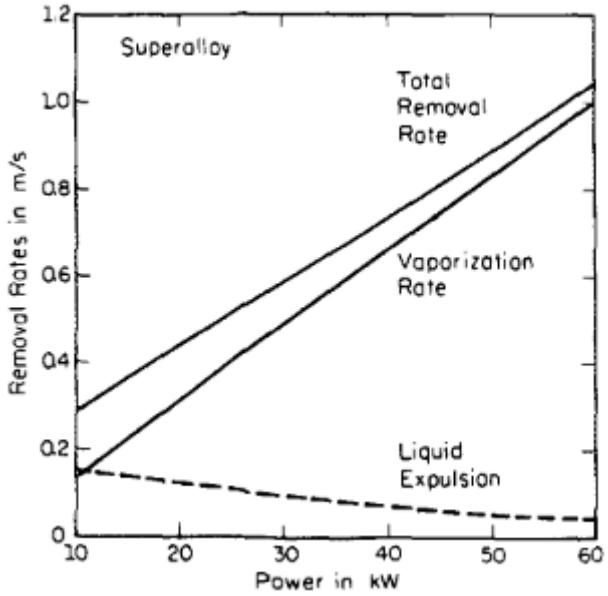

Figure 2-6 Vaporisation, liquid expulsion and total material removal rates for superalloy versus laser beam power (Chan and Mazumder, 1987).

For both materials, the vaporisation rate increases with the increase in the irradiance. However, the melt ejection rate behaves differently for different materials for the same laser irradiance. In the case of aluminium, the rate of melt ejection increases until 20 kW and then decreases with the increase in the laser power. This plot presents the melt ejection, not the melt thickness as the actual melt thickness decreases with increase in power, but the recoil

pressure created by the vaporisation is not enough to eject the material at low power below 20 kW for aluminium. At high power, the created melt layer thickness is small, and therefore the melt ejection contribution becomes smaller. For aluminium, melt ejection is the dominant material removal at low power while at high power vaporisation is dominant. In the case of superalloy, the melt ejection decreases with an increase in power while the vaporisation increases. From the analysis of Chan & Mazumder (1987), it can be concluded that the irradiance must be carefully chosen to exploit melt ejection. This is because the energy required to remove the material in its liquid state is much less than vaporising the material as will be explained later in this thesis. These findings were supported by experimental work conducted by Voisey *et al.*, (2003) through studying the fraction of melt ejection to the created holes in laser drilling for different metals at a range of laser irradiance. It was found that the melt ejection fraction depends significantly on the laser irradiance and the material properties. The melt fraction increases with the increase in irradiance that results in the increase in the pressure that is capable to eject the molten material in addition to the increase in the melt layer thickness. However, a further increase in the irradiance increases temperature gradient on the material surface that makes the surface vaporises and increases the vaporisation rate at the same time decreases the melt layer thickness leading to decrease in the melt fraction. The materials behave the same but at different irradiance range. For the same irradiance, the different materials show different fraction of melt ejection.

From the perspective of laser machining efficiency, decreasing the specific energy of material removal is one of the major concerns. The specific energy is defined as the capacity for laser energy to remove a certain mass of material. It is necessary to control the laser process parameters to achieve low specific energy according to temperature distribution inside the material, induced recoil pressure, the contribution of each melt ejection and vapour removal from the total removed material.

2.3.2 Defects in Conventional Laser Micromachining

In addition to improving laser material removal efficiency, the machining quality also needs to be considered. It must be remembered that laser machining is primarily a thermal process in which melting and/or vaporisation are the dominant mechanisms of material removal. As a consequence, a significant proportion of the energy is lost from the target area, reducing system efficiency and often producing a recognisable HAZ (Sheng and Joshi, 1995; Madic and Radovanovic, 2012).

Not all the absorbed energy is used in melting and/or vaporisation; however, the fraction of absorbed energy lost in the material through conduction is significantly controlled by the contact time. Low-intensity CW laser processes lose more energy through conduction than high-intensity pulsed lasers. Zhang and Faghri (1999) found in a one-dimensional thermal model that the fraction of the energy lost through conduction to the solid, in microsecond pulse time, is very small and its effect on the vaporisation process is not significant. It was found in the model that heat conduction significantly reduces the amount of melt material that becomes a recast material at the end of the process.

HAZ can influence the geometrical accuracy, change the microstructure of the material and produce recast material and in severe cases can lead to the formation of micro-cracks (Fu *et al.,* 2015). These microcracks affect the strength of the material. Zhang *et al*. (1996) evaluated the flexural strength of the ceramic's surface machined by a laser with a reduction to 40% of its original value. It is vital to reduce the effect of heating on materials machined by lasers.

HAZ reduction is influenced by many parameters including laser irradiation time, power, focus, pulse frequency feed rate and the number of repeat patterns (Madic and Radovanovic, 2012; Genna *et al.*, 2010; Teixidor *et al.*, 2013). Using short pulse duration requires low average power to machine in the material but with a HAZ (Brown and Arnold, 2010). Alternatively, in the ultrashort pulse, pico- and femtosecond duration regime, where the peak power is relatively very high, nonlinear absorption limits the effect on the material surrounding the machined zone, this means this regime is characterised by less HAZ and is suitable for precise applications (Le Harzic *et al.*, 2005). Table 2-1 compares between the short (nanosecond and longer pulses) and ultrashort regimes (pico- and femtosecond). In the table, the material-dependent time constants regarding the material and laser are considered. Where t_e is the electron cooling time, t_i is the lattice heating time and t_l is the laser duration pulse time.

Table 2-1 Comparison between short and ultrashort laser micromachining

Regime	Relationship between material-dependent time constants to material and laser	Peak intensity (W/cm^2)	Material removal rate	Machining Quality	Cost
Nanosecond and longer (short)	$t_e < t_i < t_l$	10^7 (Chang et al., 1998)	High	Low	Low
Picosecond (ultrashort)	$t_e < t_l < t_i$	10^8-10^{12}	Low	High	High
Femtosecond (ultrashort)	$t_l < t_e < t_i$	10^{12}-10^{14} (Peshko, 2012)			

Figure 2-7 shows the differences in the effect of using short and ultrashort laser pulses regimes on the machined material. Compared with short laser micromachining, the machined material using ultrashort laser micromachining is characterised by no recast melt layer, no microcracks, no surface debris or shockwaves surface damage.

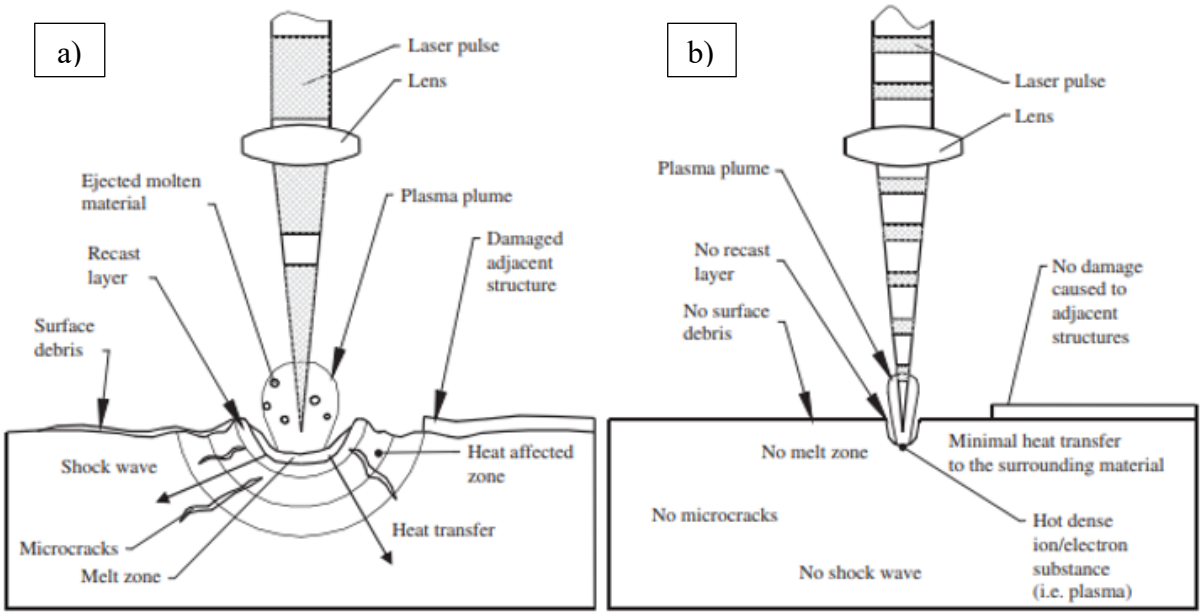

Figure 2-7 a) Short pulse laser and b) Ultrashort pulse laser (Petkov et al., 2008)

Micromachining using ultrashort pulse pico- and femtosecond lasers has been shown to reduce thermal effects. These lasers remove a layer of material commensurate to the skin depth by rapidly increasing the temperature beyond the boiling point. However, the efficiency is less than expected (Leitz, et al., 2011) and even with optimised parameters, evidence of HAZ in thermal micromachining processes are present at femtosecond (Le

Harzic *et al.*, 2005) pulse lengths. Figure 2-7 shows no shock wave in the process, however, the shock wave exists in the ultrashort laser micromachining that is generated as a consequence of high-pressure plasma absorption and expansion (Cheng *et al.*, 2013). Moreover, the pico- and femtosecond lasers are more expensive than conventional lasers (Meijer, 2004).

2.3.3 Liquid-Assisted Melt Ejection

Assist liquid has been used to improve the material removal rate and machining quality. Water is generally used as a liquid assistant due to its low cost, no environmental impact and recyclability. Several techniques have been used to supply water to the workpiece surface during laser beam machining process, e.g., underwater laser beam machining (Choubey *et al.*, 2015), spray and steam (Kruusing 2004) spraying a thin water film (Silvennoinen *et al*., 2013) and waterjet-guided lasers (Li and Kovacevic, 2003).

The most common method in liquid-assisted micromachining used for material removal is immersing the target material in a stagnated liquid. This method has been used for different types of material and different laser applications, including micromachining, cutting, drilling, and engraving. The effect of heat accumulation in conventional laser micromachining can be avoided by adding water to the machined zone, which exploits the high thermal conductivity of water (0.6 W/mK at room temperature) compared with ambient air (0.025 W/mK at ambient temperature) (Krstulović *et al.*, 2013).

In Liquid-assisted laser micromachining, laser heats the liquid at the interface causing water vaporisation. Vaporisation generates bubbles, which divide into two groups: one group grows in water and disappears; the others impact the target material by adding photomechanical pressure causing shockwaves to contribute to laser micromachining. Moreover, the transmitted laser energy leads to heating, melting and vaporisation; explosion and removal of the target material (Behera and Sankar, 2015). The rapid cooling of the ablated material by water makes it redeposit at a reduced temperature, as well as reducing the excess heat that surrounds the ablated area. The motion of the bubbles increases the time for the ablated material to stabilises in the water, away from the machined zone (Kang, Lee and Welch, 2008).

In water-jet-guided laser processing, the laser beam is guided to the workpiece to total internal reflection. This process is a combination of a thermal process from the laser and cooling process from water. Both play an important role in removing the material: the laser

melt the material and the water-jet removes the material (Richerzhagen *et al.*, 2003). The main advantages of using water jets are that no gas assistance is required, there is no need to re-adjust the focal position after the machining of each later because the system does not have a focal point. Comparing this technique to conventional laser machining, an enhancement in material removal and quality is observed (Kray *et al.*, 2007). The technique has disadvantages, however. The laser beam is disturbed inside the water jet due to a wall adhering mould compound. This means that the laser beam needs time to return, which results in the loss of laser energy during that time. The wavelength of the used laser must be compatible with the water transmission spectrum.

The technology of hybrid laser-waterjet micromachining was also used to decrease the specific energy needed to remove the material and enhance the quality. The laser beam head and water-jet nozzle are separated by a specific offset distance with the same traverse speed. The high-pressure waterjet shears and expels the laser-heated or softened material by the laser beam, as well as the waterjet working as a coolant by reducing the thermal damage during the process (Tangwarodomnukun *et al.*, 2014). The results showed the effect of processing parameters on the machining depth and the width of the grooves. The material removal rate and the quality of the machined material were both enhanced with minimal HAZ using this technique that is better than conventional dry micromachining.

The droplet-assisted technique is based on shooting droplets a hundred of micrometres in size using a droplet injector on the laser-irradiated zone at a specific frequency, synchronised with a laser pulse frequency (Ahn, Seo and Kim, 2012; López López *et al.*, 2016). This process leads to the formation of high-speed microdroplets, which are generated upon the interaction of the laser with the ejected droplet. When the laser interacts with the water droplet, the droplet temperature suddenly increases; this is accompanied by high-temperature evaporation that leads to high-intensity shock waves. The time needed to generate the forward microdroplet and hit it to the machining zone is less than the time of material melting and resolidification in the molten pool (Ahn, Seo and Kim, 2012). This transmitted laser energy (melting) and the effect of droplets microjet (melt ejection) make a combination suitable for micromachining.

Liquid-assisted laser processes have demonstrated reductions in HAZ (Muhammad *et al.*, 2010) and recast (López López *et al.*, 2016) compared to dry laser machining. However, these processes can introduce contaminants into work, or as with the case of underwater machining, create limitations to the practicality of processing.

2.3.4 Pulse Shaping in Laser Drilling

There are two main techniques of laser drilling, percussion and trepanning. In percussion drilling, multiple laser pulses are shot at the same target point to vaporise and eject layer by layer of the material until creating the required hole with diameter depends on the laser beam diameter. If the hole required is large, a trepanning technique is used by rotating the laser beam around the perimeter of the hole. Trepanning can obtain high-quality holes compared to percussion drilling (Mishra and Yadava, 2015); however, trepanning is much more time consuming and expensive compared to percussion drilling (Dhar, Saini and Purohit, 2006).

In laser drilling, the material is removed via vaporization and melt ejection depending on laser pulse time and irradiance. Temporal pulse shaping has been used during laser percussion drilling to increase the material removal efficiency via increase the melt ejection fraction and improve hole quality. This method is used where the molten material is created during the pulse time and ejected by the effect of surface vaporisation according to the change in the laser irradiance during the drilling process. Treusch and Herziger (1986) found that in laser drilling the hole geometry is influenced pulse shaping. French *et al.* (2006) used pulse shaping to improve the laser-drilled hole quality such as roundness, hole taper and recast layer. Markcoons and Voisey (2018) investigated the effect of temporal pulse shaping using pulse train shaping on the laser drilling efficiency. It was found an increase in the material removal efficiency using this method by 29% more than single pulse of the same energy, however, pulse shaping does not improve the hole quality. Method of temporal pulse train modulation to improve the percussion drilling quality has been used. This method is based on increasing linearly the laser pulse energies throughout the pulse train without changing the individual temporal pulse shape. In this method, the material ejection process could be controlled to enhance the machined workpiece quality. Compared to a normal delivery pattern, a decrease in the spatter deposition area on the workpiece surface is found; however, the recast material is increased (Low, Li and Byrd, 2001).

Experiments conducted by Gay *et al.* (2009) to study the effect of temporal nanosecond pulse shaping on the material removal efficiency and machining quality using aluminum and stainless steel materials. For aluminium material, the results showed that the material removal efficiency depends strongly on the pulse shaping and can be maximised to increase the efficiency of the laser milling process. But, the quality of the machined material (surface roughness) cannot be correlated with good quality. For stainless steel, no significant improvement in the material removal efficiency for the different pulse shapes. Moreover, no

clear correlation between material removal efficiency and surface roughness. These results have shown that the most efficient pulse shape is not necessary to be efficient for another material. In the following section, a related technique using multiple pulses to control the melt ejection in order to increase material removal efficiency and enhance the machining quality is introduced.

2.3.5 Dual Laser Micromachining

An alternative method of assisted ejection that overcomes some of the deficiencies in laser micromachining is to combine two lasers; first to melt the surface and subsequently eject the molten material. Fox (1975) was first to report the DLM method using a CW laser with a pulsed laser to cut 40 mm thick 316 stainless steel. Prior to the complete breakthrough of the CW laser, a single 25 ns pulse, peak irradiance of 10^9 W/cm^2, was introduced to the surface to push out the molten material. Fox found a decrease of irradiation time by more than a factor of two in addition to the increase in the quality by producing cleaner holes comparing to using CW only. This is because the ejection laser is only used to vaporise the molten material surface and had not yet consumed the latent heat of vaporization. Without the impulse from the ns ejection laser, the surface tension of the molten material tends to keep the molten material in its place and preventing removing the molten material to create the hole.

Other DLM experiments have demonstrated improvements in material removal rates in metals by up to an order of magnitude. Lehane and Kwok (2001) combined a long pulse (3.5 ms) and a followed short pulse (0.15 ms) to drill stainless steel plate. The DLM method showed the capability to drill 3.2-mm-thick. Walther, Brajdic and Kreutz (2008) used 0.5 ms Nd:YAG superposed with 17 ns diode-pumped solid-state pulses in percussion drilling through holes in stainless steel with 1.4, 5, 8 and 10 mm thickness. The material removal efficiency was improved by the spatial and temporal superimposed radiation of the combined two laser beams. Holes with a high aspect ratio as high as 60 were created. Recently, Wang *et al.* (2017) used 2 ms and 10 ns pulses in drilling aluminium. The results showed improvement in material removal efficiency and hole quality.

The influence of the delay time between the two pulses on the material removal efficiency was studied. The optimum time was found when the maximum melt depth occurs during the melting process from the first laser (Lehane and Kwok, 2001; Wang *et al.*, 2017; Lv *et al.*, 2018). A summary of the DLM method found in the literature is listed in Table 2-2.

The DLM method was used for drilling metals in the previous studies. In the conventional percussion drilling, the material is removed in its vapour and liquid phase. The amount of liquid or vapour is influenced by pulse duration and laser fluence. In this DLM method, the contribution of removed material in the liquid phase is dominant and it is controllable. The DLM method in this research is designed for one melting process and one pulse from ejection laser. However, this method can be designed so that successive pulses can be applied to remove the same quantity of molten material at a repetition rate equals the melting time.

Table 2-2 Summary of the DLM method in literature

Reference	Material	Laser used in melting	Laser used in melt ejection
Fox (1975)	1006 low- carbon steel and 316 stainless steel	CW CO_2 (10.6 μm) 3-4 s	Nd: glass (1.06 μm) 25 ns
Lehane and Kwok (2001)	303 stainless steel	Nd:YAG 3.5 ms	Nd:YAG 150 μs
Walther, Brajdic and Kreutz (2008)	Stainless steel	Nd:YAG (1.064 μm) 500 μs	Solid-state (DPSS) (1.064 μm) 25 ns
Wang *et al.* (2017)	Aluminum	(1.06 μm) 1-2.5 ms	(1.06 μm) 10 ns

The DLM experiments from previous studies have demonstrated improvements in laser material removal efficiency. There is a considerable range of results both in quality and efficiency. This thesis considers these characteristics. Theoretical and experimental results are compared to conventional laser vaporisation process, found in the literature, and improvement in the material removal rates and machining quality are discussed.

2.4 Summary and Conclusion

In this chapter, the background of laser fundamentals and the basic principles of laser operation were presented. The background account of laser-material interaction and laser processing parameters were defined. Laser material micromachining and the defects in the machined workpiece were explained. The literature review of the DLM was introduced. In the following chapter, the theoretical analysis of the energy used in DLM is introduced to show the benefit of using this DLM method in increasing material removal efficiency.

3 THEORY OF DLM

In the previous chapters, melt ejection methods to reduce energy input (and therefore HAZ formation) were presented with their limitations for micromachining processes. The literature on alternative DLM methods was also presented; these demonstrated improvements in material removal efficiency and quality. In this chapter, the development of the theoretical energy model for the DLM method is introduced. This model focuses on the energy consumed to produce the melt pool as the significant part of the required energy budget in DLM. The theory of the melting process is studied using a one-dimensional heat conduction model. The theoretical specific energy of total material removal for the DLM method is identified and compared with conventional laser vaporisation.

3.1 Theory

The potential benefits of DLM are made clear by comparing the energy required to remove material by direct vaporisation (ablation) to that required to melt and remove the same volume of material by mechanical means. Let us first consider the removal of material from the surface of a homogenous substrate under the assumption of uniform heating and no heat loss. If it is assumed that the specific heat capacity, C, is temperature-independent and taken at room temperature, the specific energy, E_v, required to vaporise the material is:

$$E_\mathrm{v} = C\,(T_\mathrm{v} - T_0) + L_\mathrm{m} + L_\mathrm{v} \tag{3-1}$$

where L_m and L_v are the latent heat capacities of melting and vaporisation, respectively, T_v is the vaporisation temperature and T_0 is room temperature. Similarly, the specific energy, E_m, required to melt the material is given by:

$$E_\mathrm{m} = C\,(T_\mathrm{m} - T_0) + L_\mathrm{m} \tag{3-2}$$

where T_m is the melting temperature.

Taking room temperature, $T_0 = 294$ K and using the physical properties for 316 stainless steel shown in Table 3-1, Equations (3-1) and (3-2) give $E_\mathrm{v} = 9.14\times10^6$ J/kg and $E_\mathrm{m} = 9.76\times10^5$ J/kg, respectively. For typical values such as these, it is noted that the specific energy E_v is dominated by the latent heat of vaporisation, while the specific energy E_m is largely determined by the energy necessary to raise the layer to the melting temperature, such that:

$$\frac{E_{\mathrm{v}}}{E_{\mathrm{m}}} \sim \frac{L_{\mathrm{v}}}{C\ (T_{\mathrm{m}} - T_0)} \sim 10 \qquad (3\text{-}3)$$

Table 3-1 Physical properties of materials

Property	Symbol	Unit abbreviation	316 stainless steel (Leibowitz et al., 1976)	Aluminium (Chan and Mazumder, 1987)	Superalloy (Chan and Mazumder, 1987)	Titanium (Chan and Mazumder, 1987)
Melting temperature	T_{m}	K	1700	933	1728	1940
Vaporisation temperature	T_{v}	K	3090	2793	3188	3558
Latent heat of melting	L_{m}	J/kg	2.7033×10^5	3.88×10^5	2.92×10^5	3.65×10^5
Latent heat of vaporisation	L_{v}	J/kg	7.46417×10^6	1.19×10^6	6.4×10^6	8.89×10^6
Density (at 294 K)	ρ	kg/m^3	7956.9	2700	8900	4500
Thermal conductivity[a]	k	W/m K	13.87 (at 294 K) 24.96 (at 1000 K) 20.12 (at 2350 K)	238 (at 294 K)	88.5 (at 294 K)	21.6 (at 294 K)
Specific heat capacity (at 294 K)	C	J/kg K	502	917	452	528

[a]Thermal conductivity for 316 stainless steel is presented at different temperatures that will be used later in the calculation of the theoretical melting process.

These basic calculations suggest that material removal via melt ejection is potentially around ten times more efficient than vaporisation for 316 stainless steel, however, Equations (3-1), (3-2) and (3-3) represent the minimum energy required to remove material and are based on lossless heating with no regard to the heat source or ejection process and do not represent the complex laser process sufficiently well.

The potential for energy improvement in melting and ejection if an alternative mechanical ejection mechanism is used on the melt pool, then energy could be saved compared to pure vaporisation. Calculations of $E_{\mathrm{v}}/E_{\mathrm{m}}$ were performed for 316 stainless steel, aluminium, superalloy and titanium. Their physical properties are tabulated in Table 3-1. 316 stainless steel shows the greatest potential saving in the energy (9.4) followed by titanium (8.9) and then superalloy (8.5). However, aluminium shows low saving in energy (4). It can be

concluded that the energy-saving by melting and then ejection depends strongly on the material properties.

The heat loss to the substrate can be estimated from the work of Cohen (1967). Using the analogue computing facilities available to him in 1967, Cohen investigated the propagation of the liquid/solid boundary for the case of a semi-infinite body subjected to constant heat input. He showed that in the period following surface melting and before surface vaporisation, the melt pool depth increased in an approximately linear manner until the surface reached the vaporisation temperature after which the melting process slowed substantially. The results from Cohen's analysis were compared favourably for the penetration depth as a function of melting time with the other theoretical analyses. It was found that no significant difference between Cohen's model and the other analyses (Bertolottl and Concetta, 1981). Although the non-linear, coupled differential equations governing the propagation can be solved more precisely (Xie and Kar, 1997), the graphical data provided by Cohen and the resulting empirical relationships are more useful as a means to estimate the efficiency of the melting process. Cohen's results allow us to estimate the melt depth, S:

$$S = \frac{0.14I(t - t_{\mathrm{m}})}{\rho L_{\mathrm{m}}} \tag{3-4}$$

where I is the absorbed irradiance defined by absorbed power, P, per unit area, A, t is the time required to achieve the melt depth from the start of the laser material irradiation, t_{m} is the time required for the surface to reach the melting temperature given in Equation (3-5), and ρ is the material density at room temperature. Equation (3-4) is valid for time $t \leq t_{\mathrm{v}}$, where t_{v} is the time when the surface begins to vaporise.

$$t_{\mathrm{m}} = \pi k \rho C \left[\frac{T_{\mathrm{m}} - T_0}{2I}\right]^2 \tag{3-5}$$

where k is the thermal conductivity at room temperature

The typical general case from Cohen's analysis presented in Cohen and Epperson (1968) to estimate the melt depth, $S = 0.16I(t\text{-}t_{\mathrm{m}})/\rho L_{\mathrm{m}}$, is not suitable for thermal properties of the 316 stainless steel. The specific calculation of constant 0.14 in Equation (3-4) was derived from Cohen's analysis for the unique thermal properties of the 316 stainless steel material used in this work.

It is noted that Cohen's analysis assumes that the material's properties in the molten phase are identical to those of the solid phase at room temperature except for the thermal

conductivity. A ratio k_1/k_2 was used, where k_1 and k_2 are the mean thermal conductivities in the liquid and solid regions, respectively. Although this is not strictly true; as the density, specific heat capacity and thermal conductivity are significantly temperature-dependent with a discontinuity at the melting point. To calculate the ratio k_1/k_2, the mean thermal conductivities in the liquid and solid regions was taken for 316 stainless steel to be 24.96 W/m K at 1000 K and 20.12 at 2350 K respectively (Leibowitz et al., 1976) to give $k_1/k_2 = 0.81$ and the following approximations were made from the nearest of Cohen's results ($k_1/k_2 = 0.75$).

The 0.14 constant is generated from Figure 8 in Cohen which shows the results of dimensionless depth, $[S]$, as a function of τ for several values of the ratios Y and k_1/k_2. Where $\tau = t/t_m$, Y is the ratio between latent heat of melting to the specific energy required to raise the material temperature to melting temperature: $Y = L_m/(C(T_m-T_0))$.

From the thermophysical properties of 316 stainless steel shown in Table 3-1, it was found that $Y = 0.38$. The dimensionless depth curve for $Y = 0.38$ was interpolated between the values of $Y = 0.3$ and 0.5 at the ratio $k_1/k_2 = 0.75$ found in Figure 8-a in Cohen's analysis (See Figure 3-1). To optimise the energy use in Equation (3-4), the maximum melt depth before surface vaporisation, S_{max}, was identified from Figure 8-a in Cohen's analysis (See Figure 3-1). For 316 stainless steel properties, the dimensionless surface temperature $[T]$ given by $[T] = 40(T- T_0) /(T_m-T_0) \approx 80$ where T is the surface temperature. Using this data it is evident that the surface temperature reaches the vaporisation temperature at a time, $t_v \approx 3t_m$.

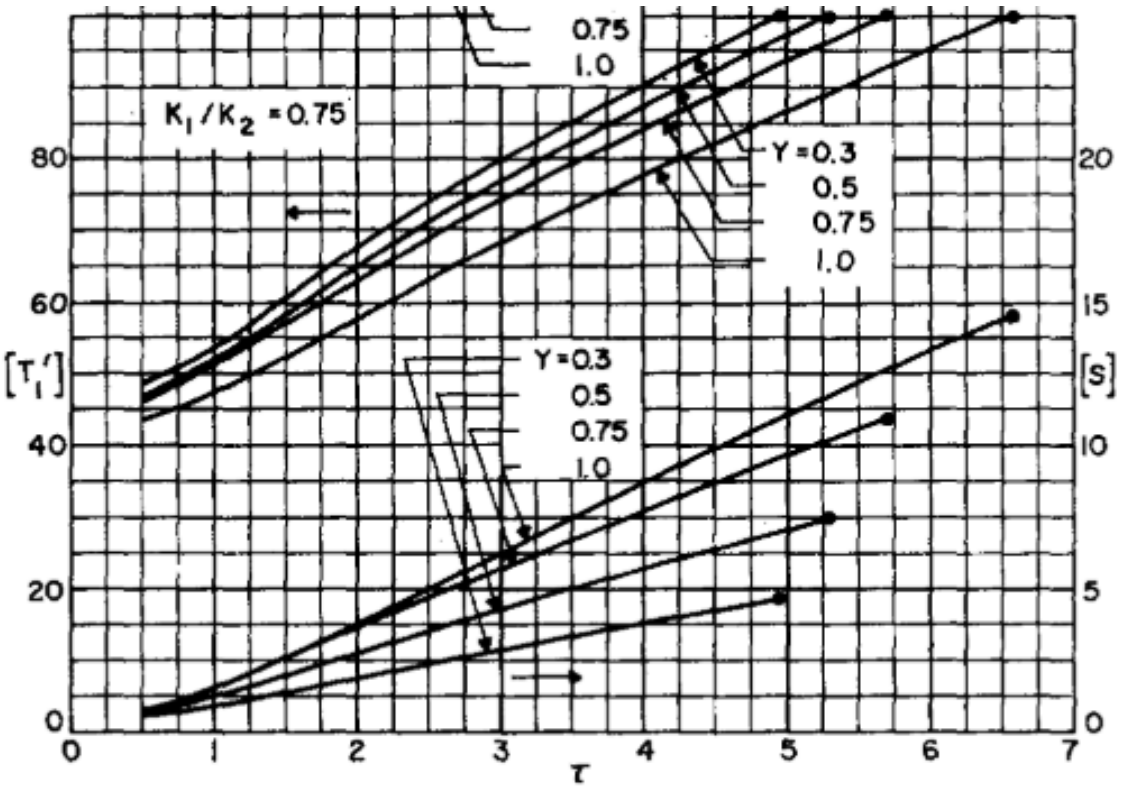

Figure 3-1 Dimensionless surface temperature and dimensionless depth of melting as a function of τ from Cohen's analysis for a wide range of parameter Y at the ratio $k_1/k_2 = 0.75$ (Cohen (1967)).

Now, the energy required to create the melt pool is considered. Let the energy required to bring a surface area, A, to the melting temperature in the period $0 < t \leq t_m$ be E_0. In the time interval that follows, $t_m < t < t_v$, the energy absorbed by the surface is $E = IA(t\text{-}t_m)$, and the melted mass is given by $m = A\rho S$. Accordingly, the specific energy E_{melt} required to create the melt pool is given by:

$$E_{\text{melt}} = \frac{E_0 + IA(t - t_{\text{m}})}{A\rho S} \tag{3-6}$$

Substituting from Equations (3-4) and (3-5):

$$E_{\text{melt}} = \frac{\pi}{4}\frac{kC}{SI}[T_{\text{m}} - T_0]^2 + 7.14L_{\text{m}} \tag{3-7}$$

In comparison with the lossless case described by Equation (3-2), it is noted that the terms in Equation (3-7) can be associated with pre- and post-melting in a similar way. The first term is the specific energy required to bring the surface to the melting temperature; the second term is simply a multiple of the latent heat of melting. An increase in desired melt depth and/or irradiance will reduce the value of the first term; reducing the proportion of total energy used

to raise the surface to T_m. As noted before, for the case of 316 stainless steel discussed in this chapter, under constant heating, the time taken to increase the surface temperature from room temperature to boiling is approximately three times that required to melt the surface and the first term is minimised when $S = S_{max} = 0.14I(t_v\text{-}t_m)/\rho L_m$ where it is found:

$$E_{\text{melt}} \approx 11L_m \tag{3-8}$$

Returning to the lossless case of Equation (3-2), it is noted that the first term is the energy required to bring a unit mass to the melting temperature and consequently has a finite value and for stainless steel $C(T_m\text{-}T_0) \approx 2.6L_m$, and combining the terms in Equation (3-2) in a similar manner it is noted that in this idealized case:

$$E_m \approx 3.6L_m \tag{3-9}$$

Therefore, it is concluded that the specific energy required to form a melt pool through surface conduction heating, E_{melt}, of 316 stainless steel is approximately 3 times that required to do so by direct lossless heating, E_m.

Finally, the specific energy to eject the liquid material must be considered, E_{eject}, to find the total specific energy for the DLM method, $E_{total\_theory} = E_{melt} + E_{eject}$. In theory, the minimum energy is that required to overcome the surface energy, γ, at the liquid-solid interface to separate the liquid and create new surface such that:

$$E_{\text{eject}} = \frac{2\gamma}{S\rho} \tag{3-10}$$

For stainless steel, $\gamma = 1.784$ J/m^2 at 1823 K (Su, Li and Mills, 2005), $E_{eject} = 5$ J/kg by taking the melt depth before surface vaporisation, S_{max}, when the energy is optimized as mentioned before using Equation (3-4) using the absorbed laser irradiance of 13 kW/cm^2 giving $S_{max} = 85$ μm. This laser irradiance will be explained how it is calculated in the following section. At least, in theory, the energy necessary to eject material can be considered to be negligible in comparison to the specific energy to form the melt pool ($E_{melt} = 2.9\times10^6$ J/kg). In the DLM method, this energy is provided by the nanosecond pulse from a second laser of which rapidly increases the surface temperature, vaporises a thin layer (vaporisation depth << melt depth) and in doing so, imparts a pressure equal to the vapour pressure at the elevated temperature (Knight, 1979). Although this process is less than ideal,

as it will be seen later the energy required by the ejection laser remains a small fraction of the total.

In Section 3.3, the results of this theory will be presented, however, it is first needed to identify the irradiance of the melting process in addition to the known physical properties of 316 stainless steel listed in Table 3-1.

3.2 Calculation of Melting Laser Irradiance

For the melting process, a fibre laser with a wavelength of 1.064 µm, was used for melting in CW mode as will be detailed in the following chapter. Using the fibre melting laser operating at maximum power (18.9 W) the onset of surface melting was found to occur with at a pulse duration of 5 ms and a tiny spot melt evidence was found at the centre of the Gaussian beam as can be seen in Figure 3-2. As has been noted by Steen and Mazumder (2010) with knowledge of the properties of the material this data point can be used to calculate the peak irradiance and the radius of the laser beam. Rearranging Equation (3-5), the absorbed irradiance required to bring the surface up to the melting temperature under the assumption of uniform heating in an infinitesimal area in the centre of the Gaussian laser beam is given by,

$$I = \sqrt{\frac{\pi k \rho c \, (T_m - T_0)^2}{4 t_m}} \tag{3-11}$$

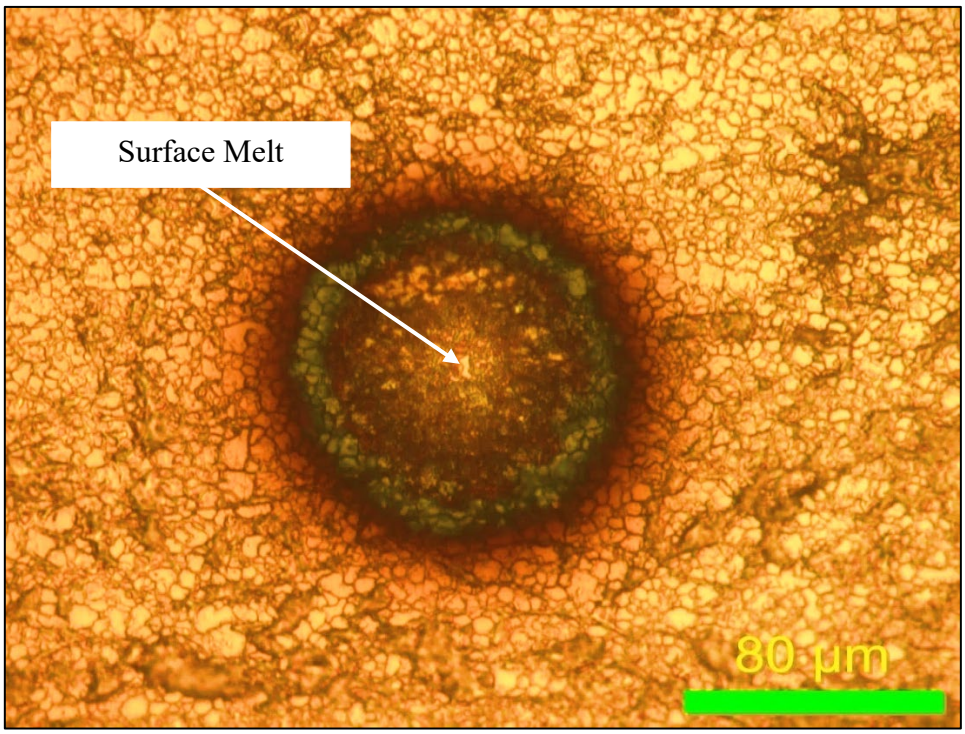

Figure 3-2 Top view of melting at 5 ms.

Using the material properties for 316 stainless steel from Table 3-1, it is found that the absorbed irradiance is approximately 13 kW/cm^2. The corresponding laser irradiance can be calculated using knowledge of the reflection coefficient, r_{melt}, such that,

$$I_0 = \frac{I}{(1 - r_{\text{melt}})} \tag{3-12}$$

The reflectance value used in the calculations is taken from measurements by Bergstrom, Powell and Kaplan (2007) for 316 stainless steel. These results are valid for Nd: YAG (1.064 μm) laser at room temperature. Although it is known that reflectivity decreases with temperature increase (Xie *et al.*, 1997) as result of the increase in the phonon population causing more phonon-electron energy exchange, the value for reflectivity will be assumed at room temperature. The roughness has a significant effect on the reflectivity due to the multiple reflections inside the undulations (Steen and Mazumder, 2010). The roughness of the workpieces used in this work (S_a: 0.142 and S_q: 0.194 μm), measured using an Alicona Infinite-Focus microscope, are similar to those used by Bergstrom, Powell and Kaplan (2007) (S_a: 0.15 μm and S_q: 0.19 μm). The reflectivity values used was 62.8% for the melting laser 1064 nm. Using $r_{\text{melt}} = 0.628$, the peak irradiance of the melting laser was found to be 35 kW/cm^2. If it is assumed that the laser beam has a Gaussian profile then the beam radius, at a position where the intensity falls to 1/*e* times its maximum value, is given by,

$$w = \sqrt{\frac{P_0}{\pi I_0}} \tag{3-13}$$

where P_0 is the total power transmitted by the beam. From the power measurements (18.9 W) and $I_0 = 35$ kW/cm^2 it is found that the beam radius is $w = 131$ μm. This corresponds well with typical burn marks.

3.3 Theoretical Results

The trends showing the energy required for lossless vaporisation and melting of a given mass (depth) are shown alongside melting from Cohen's theory, where $I = 13$ kW/cm^2, (Equations (3-1), (3-2) and (3-7) respectively) are plotted in Figure 3-3. It is noted that the lossless curves pass through the origin (Equation (3-1) and (3-2)) whereas the Cohen's theory has an offset corresponding to the energy lost bringing the surface temperature to the melting point with zero melt depth. Figure 3-3 shows that for energies below the cross-over point A, the

energy required to vaporise a given mass of material is less than that required to melt the same quantity of material. Above point (A) it becomes progressively more efficient to remove material by melting rather than vaporization (if a small amount of energy is used in melt ejection) even if the latter is assumed lossless. The maximum efficiency occurs at the maximum melt depth when the surface temperature has just reached the vaporisation point at time t_v; the point at which Cohen's theory is no longer valid (point B). From the figure, at point (B), the energy required to melt the material (Cohen's model) is approximately one third that required to vaporise the same mass of the material.

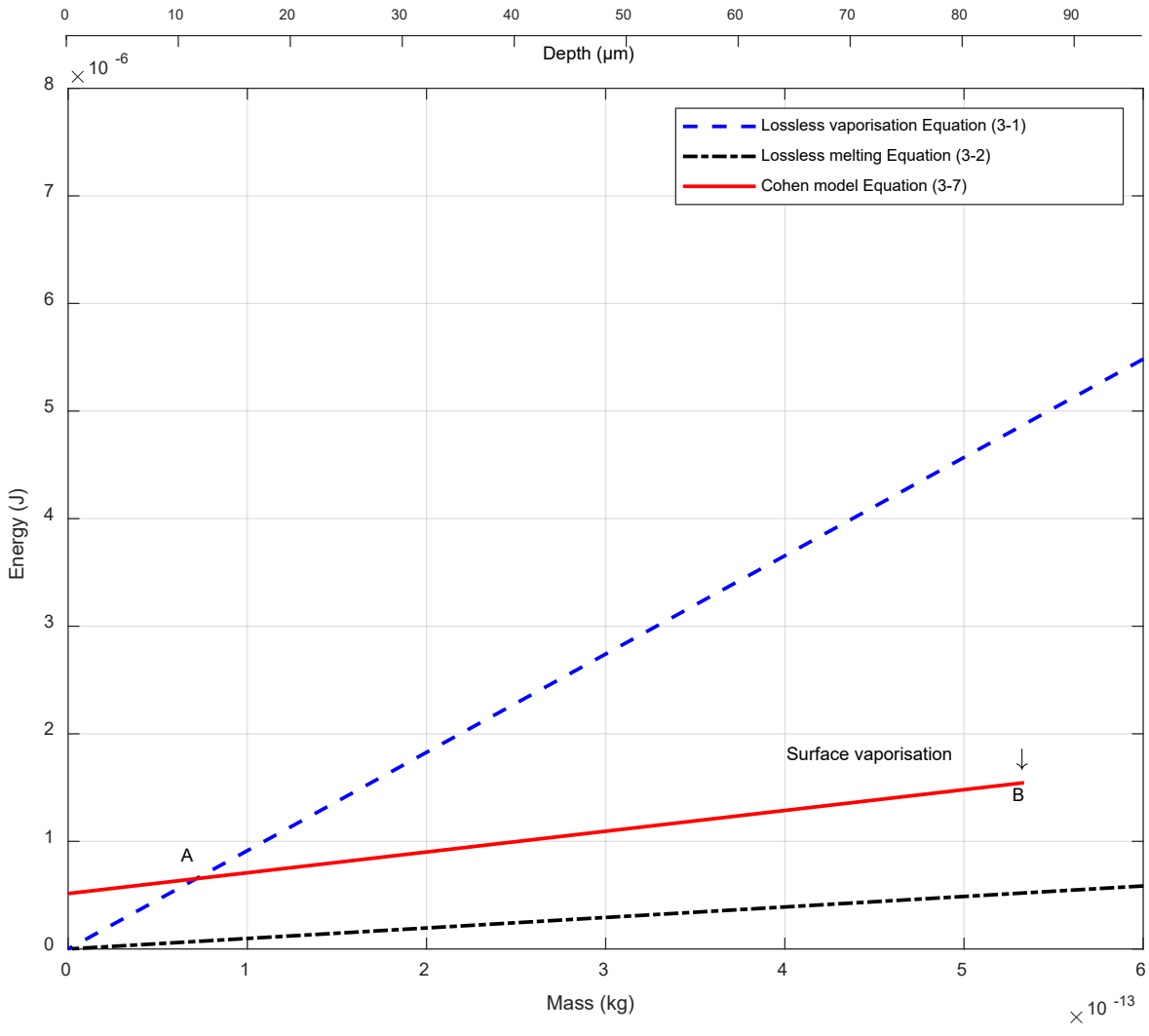

Figure 3-3 Comparing energy consumption for mass removal by lossless vaporisation, lossless melting, and Cohen's theoretical melting models for 316 stainless steel.

Finally, it is noted that ablative removal of material by way of lossless vaporisation is significantly less efficient than that suggested by Equation (3-1) and depends strongly on

pulse energy, duration (Herfurth *et al.*, 2007; Gay *et al.*, 2009). Experimentally it has been shown that in practice micromachining processes are at best 16% efficient (Leitz *et al.*, 2011). The one-dimensional model in Equation (3-1) presented has described a single pulse surface heating, similar to a piercing, drilling, or micromachining process.

3.4 Summary and Conclusion

The model described here provides some useful understanding of the energy used in the DLM method and clearly shows how the energy can be optimised. However, this theoretical model needs experimental support. The following chapter explores these findings experimentally and compares the efficiency of DLM method with the removal of material in the micromachining processes.

4 DLM IN PRACTICE

This chapter presents work to implement the theory of the DLM method in practice and compares the material removal specific energy with conventional micromachining (ablation).

4.1 Method

The work in this chapter starts by defining the material removal efficiency in the conventional laser processes. The specific energy of material removal is found through conducting conventional milling experiment using fibre laser in pulse mode in addition to the results of the conventional ablative machining found in the literature for similar materials. The specific energy of the conventional milling experiment is calculated, and the quality of the machined workpiece is assessed using metallurgical techniques. Then the DLM experiment is conducted to implement the DLM method in practice and compares the material removal specific energy with conventional micromachining (ablation). Two laser beams are used in the DLM method a fibre laser in CW mode to create the melt pool combined with a nanosecond Nd:YAG laser to eject the molten material as listed in Table 4-1.

Table 4-1 Specifications of the lasers used in the DLM method.

Laser	Melting laser (fibre)	Ejection laser (Nd:YAG)
Wavelength	1064 nm	532 nm
Pulse duration	CW	4-6 ns
Output power	18.9 W	-
Collimated beam diameter	-	7 mm
M^2	1.6	1.3
Focus size	131 µm (radius, 1/e)	Elliptic of 400 µm major and 300 µm minor axes
Irradiance	35 kW/cm^2	10 GW/cm^2
Pulse energy	-	50 mJ
Fluence	-	53 J/cm^2
Focal length	160 mm	120 mm
Repetition rate	-	20 Hz

Making use of a previous configuration the DLM method was initially set-up with a moving workpiece (moving mode) but was subsequently analysed with a static set-up (stationary mode) to allow straightforward comparison with theory. The quality of the DLM method is also assessed using metallurgical techniques. Three experimental set-ups are conducted to investigate the DLM in practice. First molten pool generation using only the CW laser beam is explored to investigate how the melt pool develops with time. The effect of nanosecond

pulsed laser on the material surface without pre-melting was then considered to examine its machining capability. Finally, the combination of both lasers in the DLM method was investigated as a means to achieve liquid phase ejection.

4.2 Conventional Laser Micromachining

In this section, conventional laser micromachining is applied to stainless steel. The specific energy for laser micromachining experiments and available experimental data of stainless steel from the literature is identified and compared that will be compared later with the specific energy results of the DLM method. The results revealed from these conventional processes will be compared with the results of the DLM method.

4.2.1 Laser Milling Experiment

The laser milling process has been used by many researchers as an example of laser micromachining to study the effect of different laser processing parameters on the specific energy and the machining quality or to compare the laser processes with the traditional mechanical processes by performing a 3-D features pockets (Herfurth *et al.*, 2007; Ciurana, Arias and Ozel, 2009; Orazi *et al.*, 2010).

4.2.1.1 Experimental setup

The experiments were carried out by milling 3mm x 3mm squares into the surface of the 316 stainless steel workpiece using an SPI G4 Fibre Laser Module, with a wavelength of 1.064 µm. Multiple layers of parallel linear patterns were scanned using the direct laser writing 2D galvanometer device, as illustrated in Figure 4-1. The scanner head is fitted with an F-Theta lens with a focal length of 160 mm. The final focused beam diameter, D, is 30 µm measured on the substrate and verified by optical measurement of the spot created on laser mode burn paper. The laser beam was focused to provide a laser fluence from 10 to 141 J/cm^2 for pulse energy ranges. This laser fluence is above the vaporisation threshold for metals (Xu, 2002). The scanning speed, S_S, was chosen to achieve 0% overlap calculated in $S_S = fD$, where f is the pulse repetition frequency and D is the diameter of the focused laser beam on the workpiece surface.

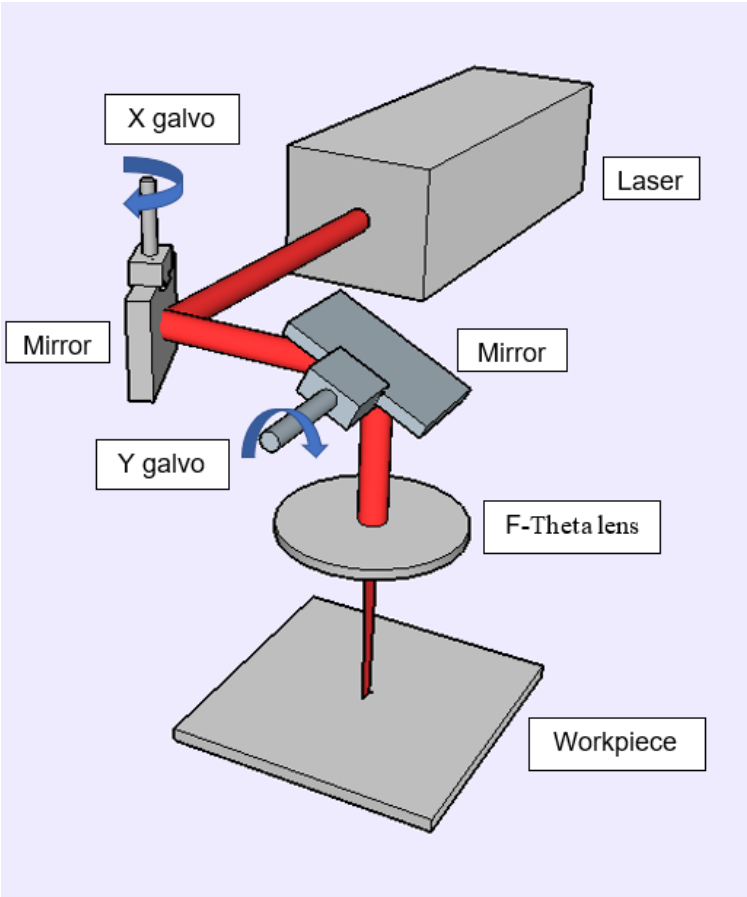

Figure 4-1 Experimental setup of the fibre laser. The beam is reflected by the rotary mirrors on the workpiece surface

The key laser parameters are pulse duration of 9-115 ns, the maximum repetition rate of 70-1000 kHz pulse and pulse energy of 0.07-1.0 mJ. The spatial beam profile is with an M^2 <1.6. This laser is based on optical amplifier called master oscillator power amplifier (MOPA) that gives the laser to have a relatively broad range of pulse durations and maintaining full average power despite the increase in repetition rate. The laser has pulse tuning technology allows tuning the pulses in different programmed waveforms with optimised peak power at a pulse repetition frequency called "PRF0". Some examples of different waveforms, out of 36 waveforms available in the laser, are detailed in Table 4-2.

Table 4-2 Waveforms and their corresponding PRF0, maximum pulse energy and pulse duration.

Waveform number	PRF0 (kHz)	Maximum pulse energy (mJ) at PRF0	Pulse duration (ns)
0	70	1.0	46
6	119	0.61	35
25	490	0.15	16
28	1000	0.07	9
36	70	1.0	115

Within each waveform, the pulse energy and the average power are a function of pulse repetition rate as illustrated in Figure 4-2. The average output power (dashed curve) decreases linearly with the decrease in pulse repetition frequency (PRF) below PRF_0. At PRF above PRF_0 the average power of the laser is maintained at its maximum whilst pulse energy (solid curve) decreases with increasing PRF. As the PRF increases, the pulse energy decreases as $E_{max} \times PRF/PRF_0$.

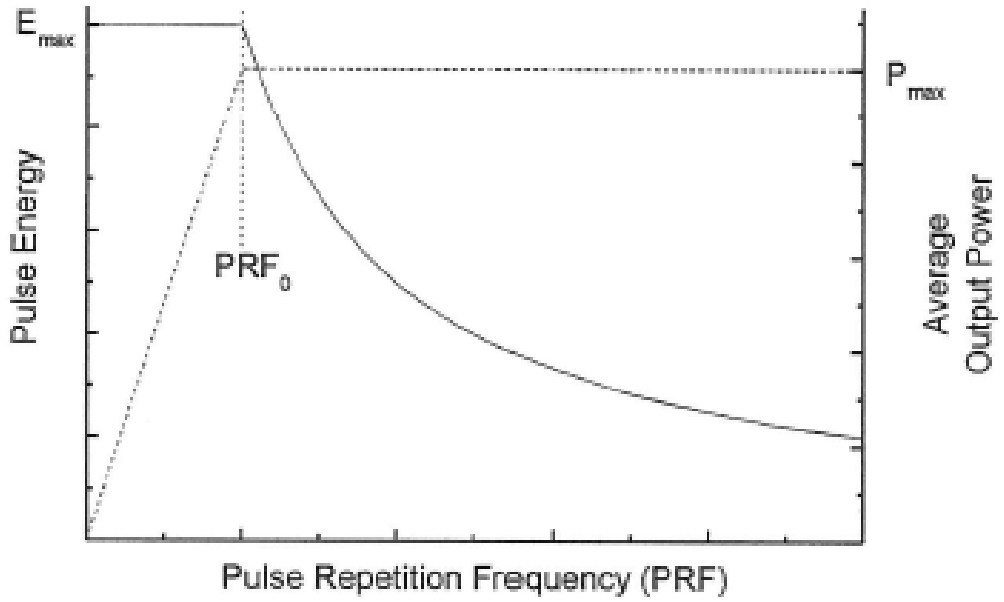

Figure 4-2 The change in the pulse energy and the average output power with respect to the pulse repetition frequency (Source: SPI G4 Fibre Laser manual).

The material used in this study is 316 stainless steel with 3 mm thicknesses. This material was chosen to make suitable comparisons to the literature on conventional nanosecond laser micromachining efficiency (Herfurth *et al.*, 2007; Gay *et al.*, 2009; Leitz *et al.*, 2011) as will be presented in Section 4.2.2. This alloy is an engineering material with many applications industry (Yilbas, Davies and Yilbas, 1992; Baddoo, 2008).

4.2.1.2 Results

Trial experiments were carried out to find the specific energy of different parameters of the waveforms. The 3D surface measurement device Infinite-Focus (Alicona) was used to take images of the pockets then the volume was measured using TalyMap Platinum 5.0 software by generating a series of profiles from the scanned surface. The volume was multiplied by the

material density in the solid phase to show the result of the removed material in mass as all the results of this thesis are presented in the mass term.

The optimum result was found to be waveform 0 at PRF0. The specific energy of milling experiment E_{milling} of the pulse duration of 46 ns, a repetition rate of 70 kHz pulse and pulse energy of 1.0 mJ was found to be 1.4×10^8 J/kg as calculated in Equation (4-1).

$$E_{\text{milling}} = \frac{NE_{\text{pulse}}}{V\rho} \tag{4-1}$$

where N is the number of laser pulses, E_{pulse} is the single pulse absorbed energy, V is the volume of the milled pockets and ρ is the material density at room temperature.

In the following section, the results are compared to those found in the literature.

4.2.2 Previous Work of Stainless Steel Micromachining

Although laser micromachining applied to stainless steel in many articles, only relatively few references relate material removal rates to laser energy. The results of these references are presented in this section.

Leitz *et al.* (2011) presented a comparative study of the laser micromachining of stainless steel by microsecond, nanosecond, picosecond and femtosecond laser pulse durations. In terms of the specific energy, it was found that the nanosecond regime was the most efficient due to the contribution of the melt ejection in the total material removal that requires less energy as discussed before in Section 3.1. However, the picosecond regime is more representative of material removal via vaporisation and will be used for comparison with milling result. In Leitz's picosecond experiments, a laser of 1064 nm wavelength, 10 ps pulse duration, 150 μJ pulse energy, and peak laser fluence 6 J/cm^2 was used. Different depths of drilling were achieved by varying the number of pulses (300-500,000 pulses). For favourable comparison with milling experiment results, the most efficient result created by 300 pulses of picosecond regime was chosen. The result is presented in Figure 4-3, using the same reflectivity (0.628) used for 316 stainless steel. The specific energy of material removal was found to be 3.8×10^7 J/kg.

Work done by Gay *et al.* (2009) using different pulse characteristics to improve the material removal per unit energy of similar material (304 stainless steel) at 4.4 μJ pulse energy in 30 ns pulse time scale at peak irradiance of 140 MW/cm^2 and a repetition rate of 200 kHz. The results of the micro-milling experiment in terms of material removal mass per unit energy

were calculated and are also presented in Figure 4-3. Although the data of material removal efficiency does not state the reflectivity, the same reflectivity (0.628) used for 316 stainless steel was used to calculate the absorbed energy. The mean specific energy was found to be 4.7×10^7 J/kg.

Herfurth *et al.* (2007) established optimal processing parameters for different materials include 304 stainless steel by milling 1.8 x 1.8 mm squares into the surface. A nanosecond MOPA based fibre laser was used with a wavelength of 1.064 μm, pulse duration ranging from 20 to 640 ns, maximum pulse energy 0.5 mJ, average intensity of 44.2 MW/cm^2 and different pulses overlap percentages that governed by the spot diameter of 25 and 45 μm, the scanning speeds of 100 to 800 mm/s and pulse repetition rates of 20 to 100 kHz. The highest material removal efficiency was found at 20 kHz repetition rate, 320 ns pulse duration and 150 mm/s scanning speed and presented in Figure 4-3. The same reflectivity (0.628) used for 316 stainless steel was used to calculate the absorbed specific energy for the result of Herfurth *et al.* (2007) to be 1.4×10^7 J/kg.

The theoretical model of the lossless vaporisation presented in Figure 4-3 is used to describe the energy required for mass removal by direct vaporisation (ablation). The curve is presented for 316 stainless steel and other types of stainless steel despite a slight difference in the material properties. This lossless vaporisation curve was compared to the results from literature in the following order from high to low specific energy Gay *et al.* (2009), Leitz *et al.* (2011) and Herfurth *et al.* (2007).

It is clear from Figure 4-3 that there is a significant difference in specific energy between these processes from literature. This may be justified by the difference in the laser irradiance that determines the dominant mechanism to be vaporisation or melt ejection (Chan and Mazumder, 1987). For the same laser milling process and the same material, Herfurth *et al.* (2007) used less laser irradiance than Gay *et al.* (2009). Other parameters play an important role in the material removal efficiency such as frequency, scanning speed (Herfurth *et al.,* 2007), and pulse duration determines the energy lost via conduction and the amount of melt material that becomes a recast material at the end of the process (Zhang and Faghri, 1999).

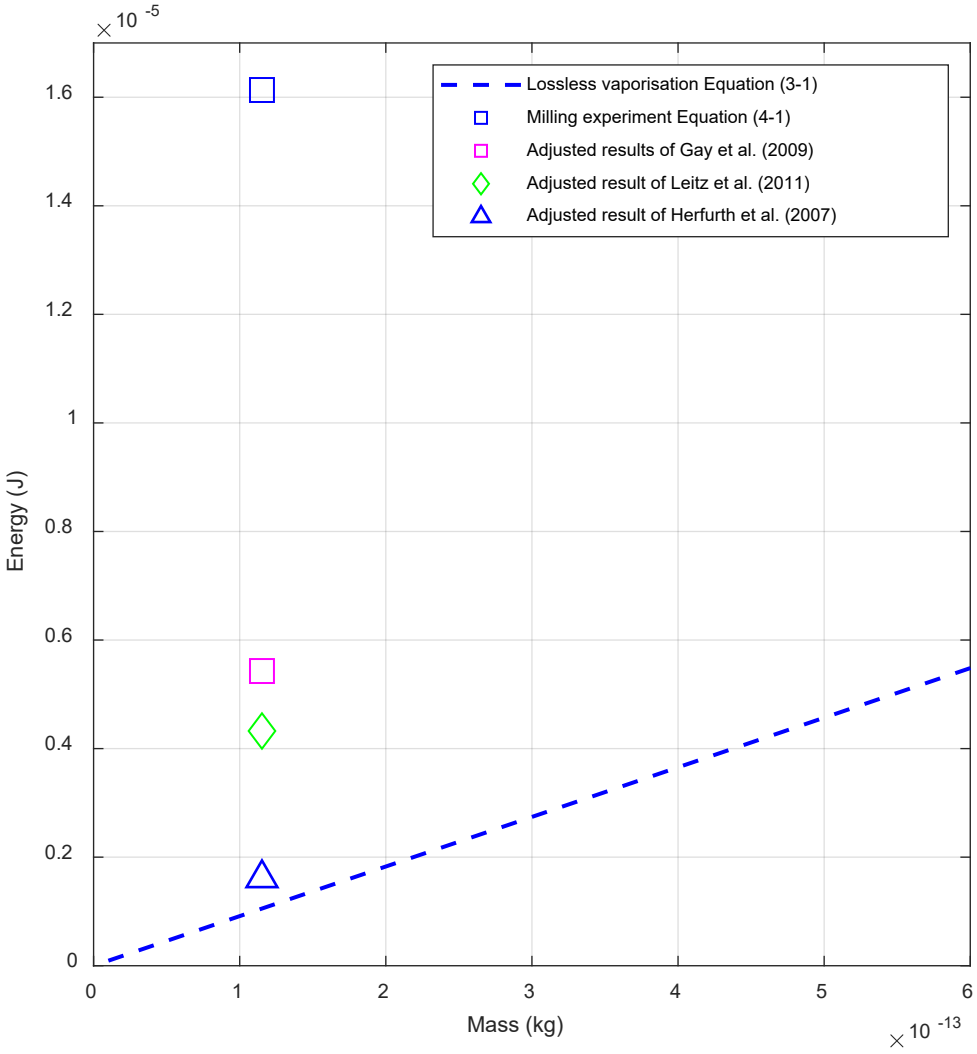

Figure 4-3 The absorbed energy against the removed mass for previous work, milling experiment and the lossless vaporisation model.

The results of the conventional milling process in this work were compared to the results from the literature. All the results from literature in the following order from high to low-efficiency Herfurth et al. (2007), Leitz et al. (2011) and Gay et al. (2009) was more efficient than milling experiment by approximately 9, 4 and 3 times in the same order. However, the milling process done in this thesis is not optimised for all the parameters and is limited by the available maximum pulse energy that may increase with the increase in the laser fluence.

The specific energy of the milling experiment has been found and compared with conventional laser micromachining from the literature. In the following section, the quality of milling experiment will be assessed.

4.2.3 Defects Observed in Conventional Laser Milling

The quality of the milling process was assessed by metallurgical techniques. The recast molten material and HAZ are used in the analysis as a quality indicator. The metallurgical features created by the milling process were analysed by taking scanning electron microscope (SEM) image as can be seen in Figure 4-4 using a FEGSEM Jeol 7100. The cross-section of the pocket was taken from its centre. Samples were prepared for microstructural analysis by mounting using "KonductoMet" bakelite, mechanically grinding using series of sandpapers of 400, 800, 1200 grit, SiC grades, polishing using 9, 3 and 1 µm diamond suspension and finally vibratory polishing with Colloidal Silica chemo-mechanically polished for 2 hours.

Analysis of the material quality shows that the created pocket was found with residual molten material along the bottom as can be seen in Figure 4-4-b. The thickness of residual material was measured about 14 µm along the pocket bottom. Comparing the residual molten material in relation to the material removal depth, the amount of un-ejected material was about 5% from the mean melt depth of the pocket. Moreover, the micrograph shows clearly the formation of pores in the recast material formed mainly due to the entrapment of gases by surface turbulence. In addition, non-joined solidified melt material was found in the recast material due to the high solidification rate that increases the thermal shrinkage strain and the stress gradient at a high rate without the opportunity to be refilled by the molten material. On the other hand, no phase transformation was observed in the HAZ since the austenitic stainless steel is not transformable (Pouranvari and Marashi, 2009). The micrographs were with no change in grain size content in the areas around the hole relative to the base metal, implying that metallurgical changes do not have a dominant effect in the HAZ.

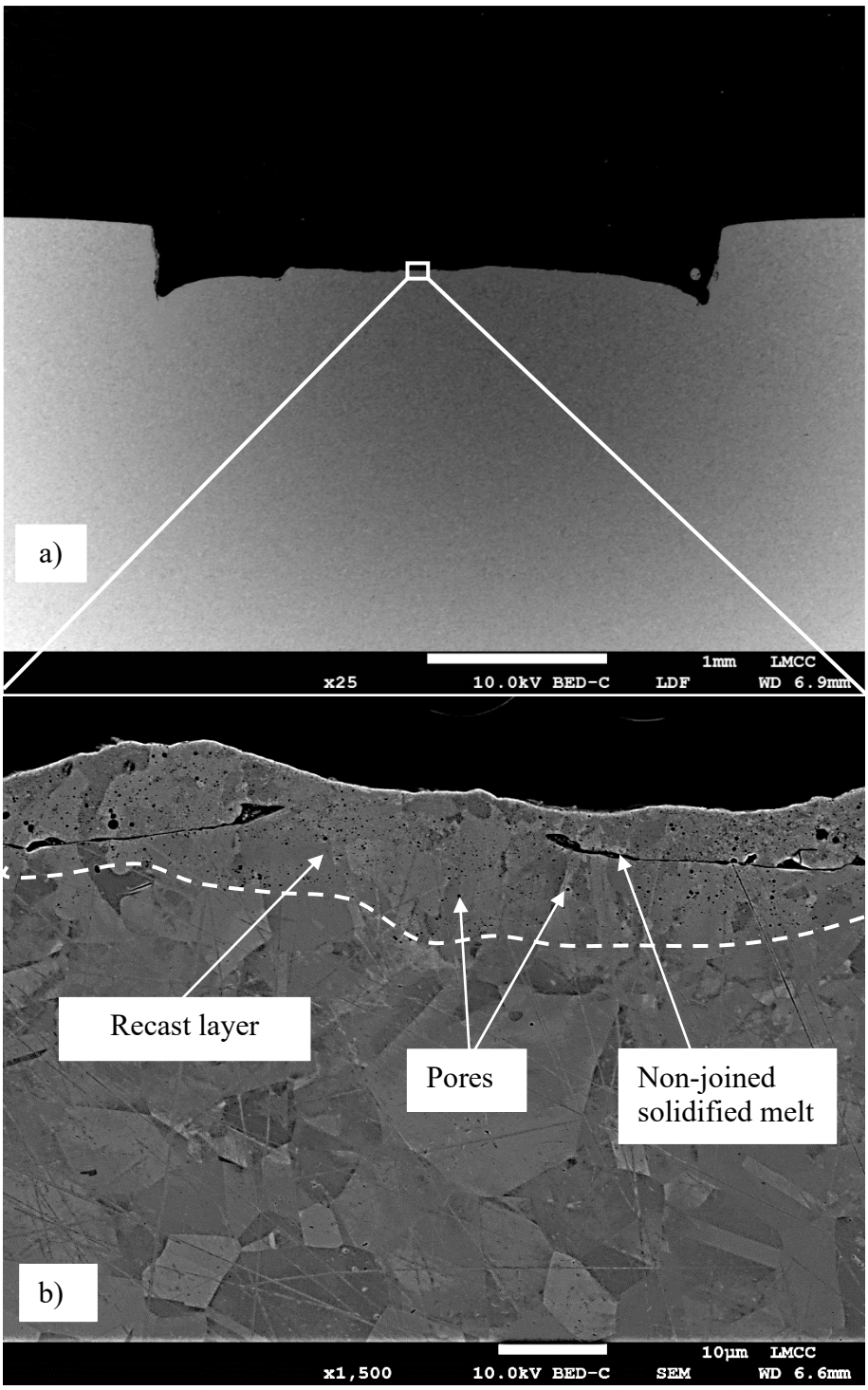

Figure 4-4 Milling cross-sectional images, a) the geometry from the centre of the pocket square and b) the recast material and the defects at high magnification.

The conventional milling experiment was presented and evaluated by the material removal efficiency and analysed from the quality side. In the following section, an initial experiment will be presented for the DLM method in a moving mode and subsequently in a stationary mode.

4.3 DLM in Moving Mode: Experimental Setup and Results

This section presents work to implement the DLM method in practice. The DLM experiment was conducted 316 stainless steel (3 mm thickness) at moving mode. The quality of the DLM method is assessed using metallurgical techniques. Three experimental set-ups were investigated to investigate the applicability of DLM in practice. Firstly, molten pool generation using only the CW laser beam was explored to investigate how the melt pool develops with time (velocity). The effect of a nanosecond pulsed laser on the material surface was then considered to examine its machining capability. Finally, the combination of both lasers in the DLM method was investigated as a means to achieve liquid phase ejection.

4.3.1 Experimental Setup

Two lasers were used in this study: A CW fibre laser, the "melting laser" to create a molten pool; a Q-switched Nd: YAG laser, the "ejection laser", provided the necessary impulse required to eject the molten material. The same laser used for milling process SPI G4 Fibre Laser Module, with a wavelength of 1.064 μm, was used for melting in CW mode. The power of the laser was measured to be 18.9 W using a Coherent LM-200 power meter. The beam is focused using a galvanometer scanning head fitted with a 160 mm focal length F-theta lens. The beam was defocused to enlarge the beam size to provide a constant peak irradiance of approximately 35 kW/cm^2. This laser irradiance is in the conduction-limited mode without vaporisation in the melting process (Sun and Ion, 1995). A Q-switched Continuum Surelite Nd: YAG laser with a 4-6 ns pulse width, 532 nm wavelength, 10 Hz repetition rate was used for melt ejection. The pulse energy of 50 mJ was measured using Gentec-EO Model SOLO 2 (R2).

A set of dielectric mirrors were used to deliver the Nd: YAG laser beam to the same position as the fibre laser beam spot on the target workpiece surface. A lens of focal length 120 mm was used to focus the ejection laser beam. The focal plane position could be manually adjusted by a Newport precision stage until achieving the minimum Nd: YAG laser spot size. The fibre laser, illuminated the object at normal incidence while for practical convenience, the ejection laser beam was focused with an incidence angle of approximately 40˚ that makes the beam on the workpiece becomes an elliptic shape whose major and minor axes are 400 and 300 μm respectively, giving a laser fluence of 53 J/cm^2 that is above the vaporisation threshold for metals (Xu, 2002). The experimental setup of the DLM in moving mode is illustrated in Figure 4-5. 316 stainless steel with 3 mm thicknesses was used in this study.

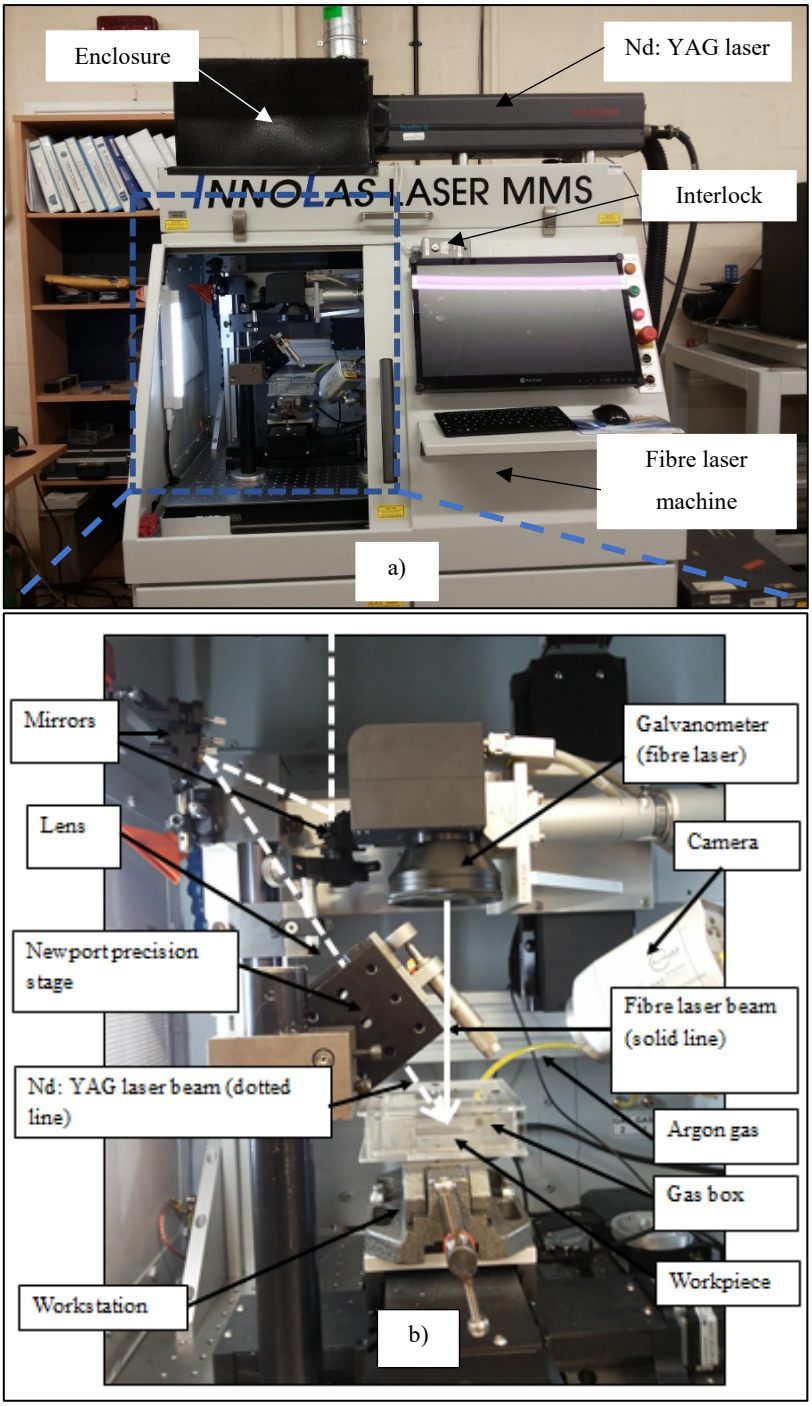

Figure 4-5 DLM method setup at moving mode a) the two lasers and b) inside the fibre laser cabinet

The DLM method set up was in a class 1 laser fibre laser cabinet. An interlock was used to operate the Nd: YAG laser. From a health and safety perspective, the Nd: YAG laser was connected to the fibre laser interlock system to stop the process once the fibre laser door opens. The Nd: YAG laser works only if the fibre laser door is shut, the emergency stop is off, the shutter in Nd:YAG laser is on and the shutter control switch is on. The process was monitored by external TV screen connected with a camera inside the cabinet instead of the

built-in glass window that is not suitable for Nd:YAG laser wavelength (532 nm) and its power density.

In these experiments, the workpiece is mounted on X, Y-translation workstation stage (Aerotech pro115). While both laser beams are stationary, the workpiece was moved relative to the beams at a constant velocity in the *y* direction as illustrated in Figure 4-6. The melting process was evaluated to determine the melt depth for the melting velocity range. The relative offset distance between the centre points of the two laser beams on the surface was varied between -300 and 300 µm as shown in Figure 4-6 to identify the position of maximum melt depth. The reason behind the offset distance will be explained later in the results section.

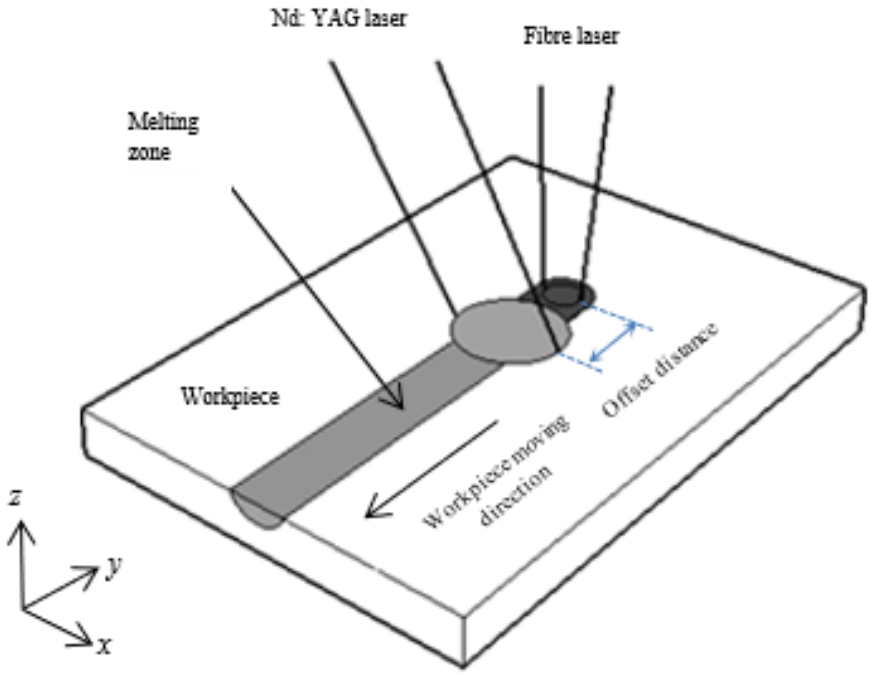

Figure 4-6 Schematic diagram of DLM method setup. This diagram shows the direction of motion and the offset distance between the centre of the two laser beams.

The melting process was conducted at a power of 18.9 and 1 to 42.5 mm/s moving velocity range to determine the melt depth. To prevent oxidation, all the experiments in this study were carried out with argon shielding gas. The argon gas was introduced into an open-top box where the workpiece was located. The optimum gas flow rate and the pressure of 4 L/min and 1.5 bar, respectively, were found to achieve the minimum oxygen percentage of 3% at the workpiece surface, verified using a Kane 510 single gas analyser. It is noted that this flow rate is insufficient to remove any molten material.

4.3.2 Analysis Technique

The metallurgical features created by DLM method and the melt cross-section in the melting process were analysed by taking scanning electron microscope (SEM) images using a FEGSEM Jeol 7100. The cross-section of the holes was taken from their centres. Workpieces were prepared for microstructural analysis by mounting using "KonductoMet" bakelite, mechanically grinding using series of papers of 400, 800, 1200 grit SiC grades, polishing using 9, 3 and 1 μm diamond suspension and finally vibratory polishing with Colloidal Silica chemo-mechanically polish for 2 hours. The recast molten material and HAZ are used in the analysis as a quality indicator.

4.3.3 Results

The following sections present the results of surface treatment using the melting laser only, the (Nd:YAG) ejection laser only and both lasers combined in the DLM method.

4.3.3.1 Effect of Melting without Ejection

To find the range of velocities used for melting, initial tests were carried out first with the relevant irradiance parameter in a wide range of laser melting velocity and maintaining a constant laser irradiance at 35 kW/cm^2.

Figure 4-7 shows the depth of melt pools created with 1 – 37.5 mm/s melting velocities to a maximum melt depth of 33.1 μm at a velocity of 1 mm/s. The maximum depths were measured from the workpiece surface. The onset of surface melting was found to occur with at a velocity of 42.5 mm/s. The melt depth increases with the decrease in the velocity until the velocity of 25 mm/s and then slightly increases, suggesting that the melt pool has completely developed. It is expected flow generated by surface tension driven convection known as the Marangoni effect, with a small contribution from the buoyancy force (Basu and DebRoy, 1992) and more efficient heat transfer the heat from the centre to the edge (Mazumder, 1991). Significant increase in the melt depth is observed at velocities below 10 mm/s. For the low velocities (high irradiation time), the new vapour-liquid interface is created and moving down inside the material at the same time the melt-solid interface moves inside the material making the measured depth of this melt-solid interface that is represented in the graph as melt depth.

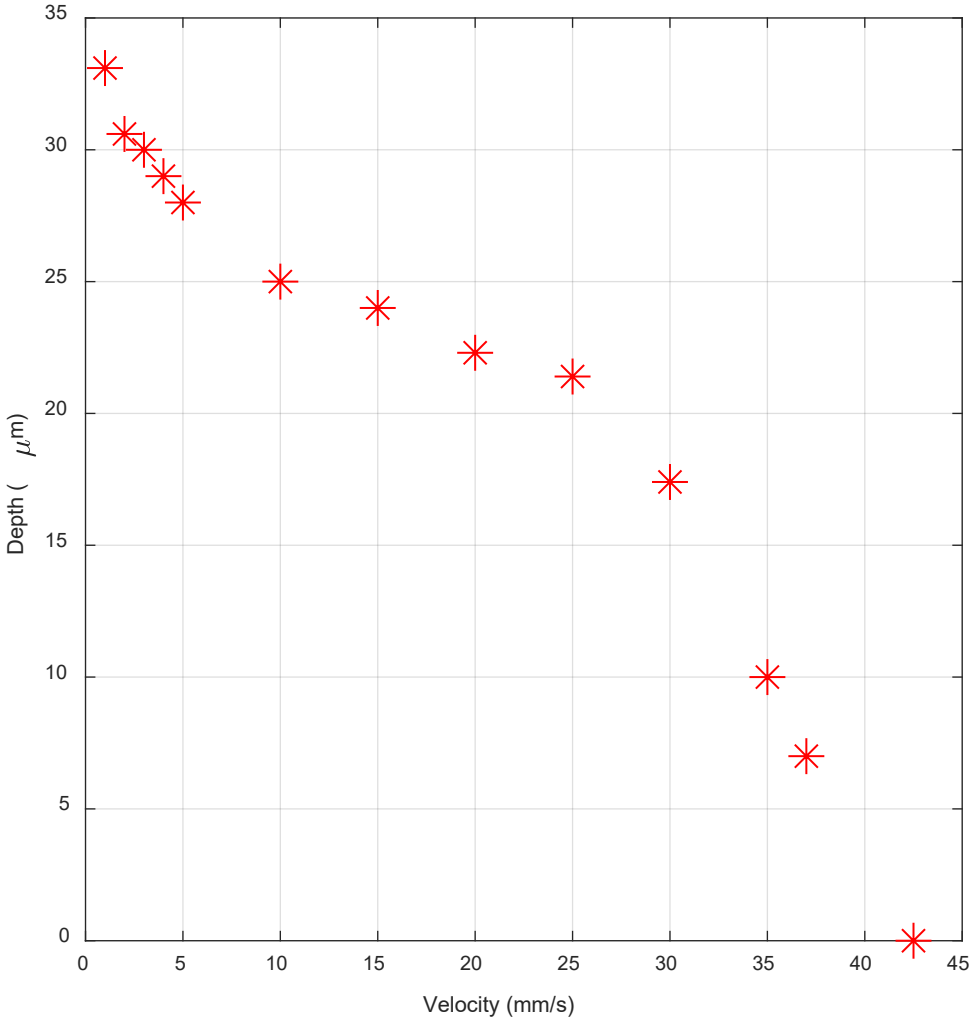

Figure 4-7 The maximum melt depth of different velocities at an irradiance of 35 kW/cm^2.

Figure 4-8 shows cross-sections of the solidified melt pools obtained at high (25 mm/s) and low (1, 2 and 3 mm/s) velocities. A relatively flat surface can be seen at high velocity whereas a significant change to the melt surface cross-sectional shape can be seen at 3 mm/s. The cross-sections of very low velocities ≤ 2mm/s show the formation of a new liquid-vapour interface as a result of material removal via vaporisation.

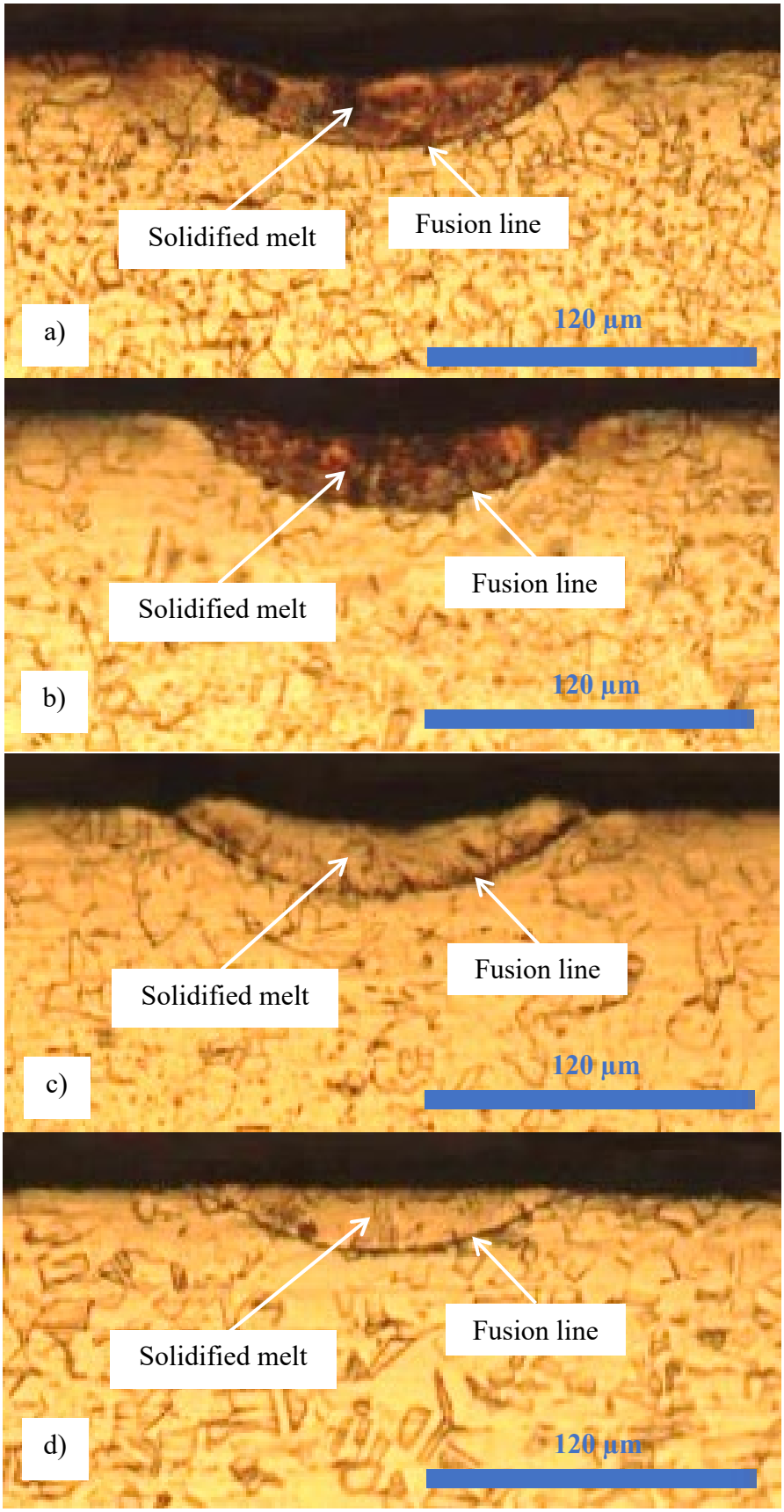

Figure 4-8 Melting cross section at velocities of a) 1 mm/s, b) 2 mm/s, c) 3 mm/s and d) 25 mm/s

4.3.3.2 *Effect of Ejection Pulse without Melting*

The effect of only the ejection laser, without pre-laser melting, was observed. The experiment was conducted using a single pulse at 50 mJ energy on the workpiece at room temperature. 2D surface profiles were measured using an Alicona Infinite-Focus. The features of the profile were calculated using TalyMap Platinum 5.0 software. Figure 4-9 shows material removal with only 1.94 µm maximum depth below the workpiece surface. The 2D line roughness parameters R_p and R_v were measured using Talymap software along with the x–z plane to show the change in the surface feature for the machined material and the parent material. For the machined material, the R_p and R_v values were 1.4 and 1.51µm respectively while the R_p and R_v for the parent material were 0.324 and 0.557, respectively.

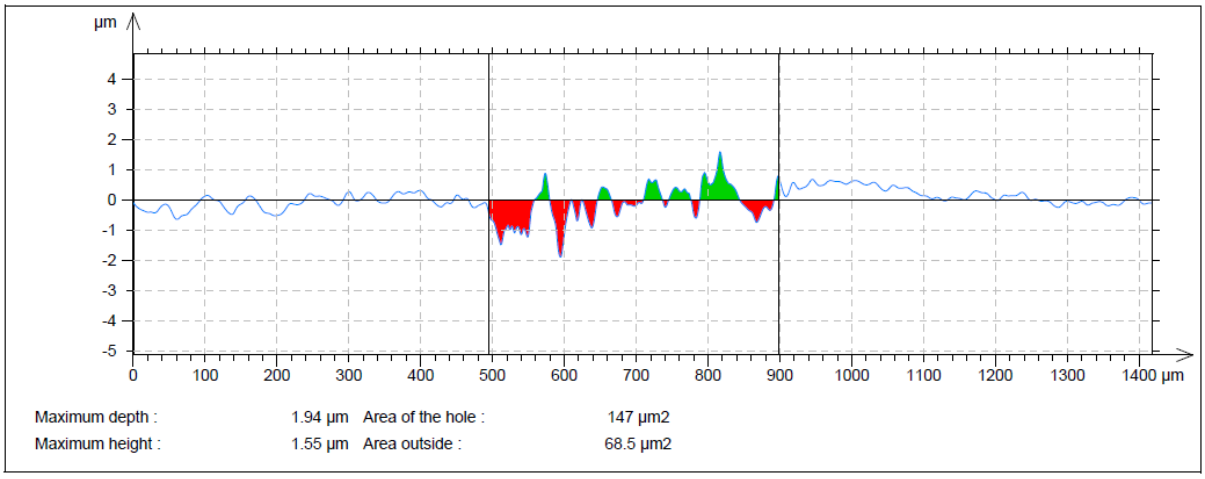

Figure 4-9 2D surface profile of only the nanosecond melt ejection pulse of the Nd: YAG laser.

Figure 4-9 shows the difference between the ejected and redeposited material as cross-sectional area. The total area of the removed material is 146 µm while approximately half, 68.5 µm, of this value, is redeposited on the top of the workpiece surface. It is evident from the profile that the nanosecond pulse alone does not remove a significant amount of material. However, as will be shown in the following section the same pulse applied to a melt pool is sufficient to remove most of the molten material.

4.3.3.3 *Initial DLM Experiment*

The DLM method was conducted at relatively deep melt depth of melting velocities 3 mm/s and also at the most efficient melting velocity of 25 mm/s. The results of melting at a velocity of 3 mm/s are shown in Figure 4-10-a. There is some redistribution during melting but no significant material removal.

The combined DLM method in Figure 4-10-b shows that the molten material was ejected by the effect of molten pool surface vaporisation using the ejection laser, with no evidence of redeposited material on the workpiece surface.

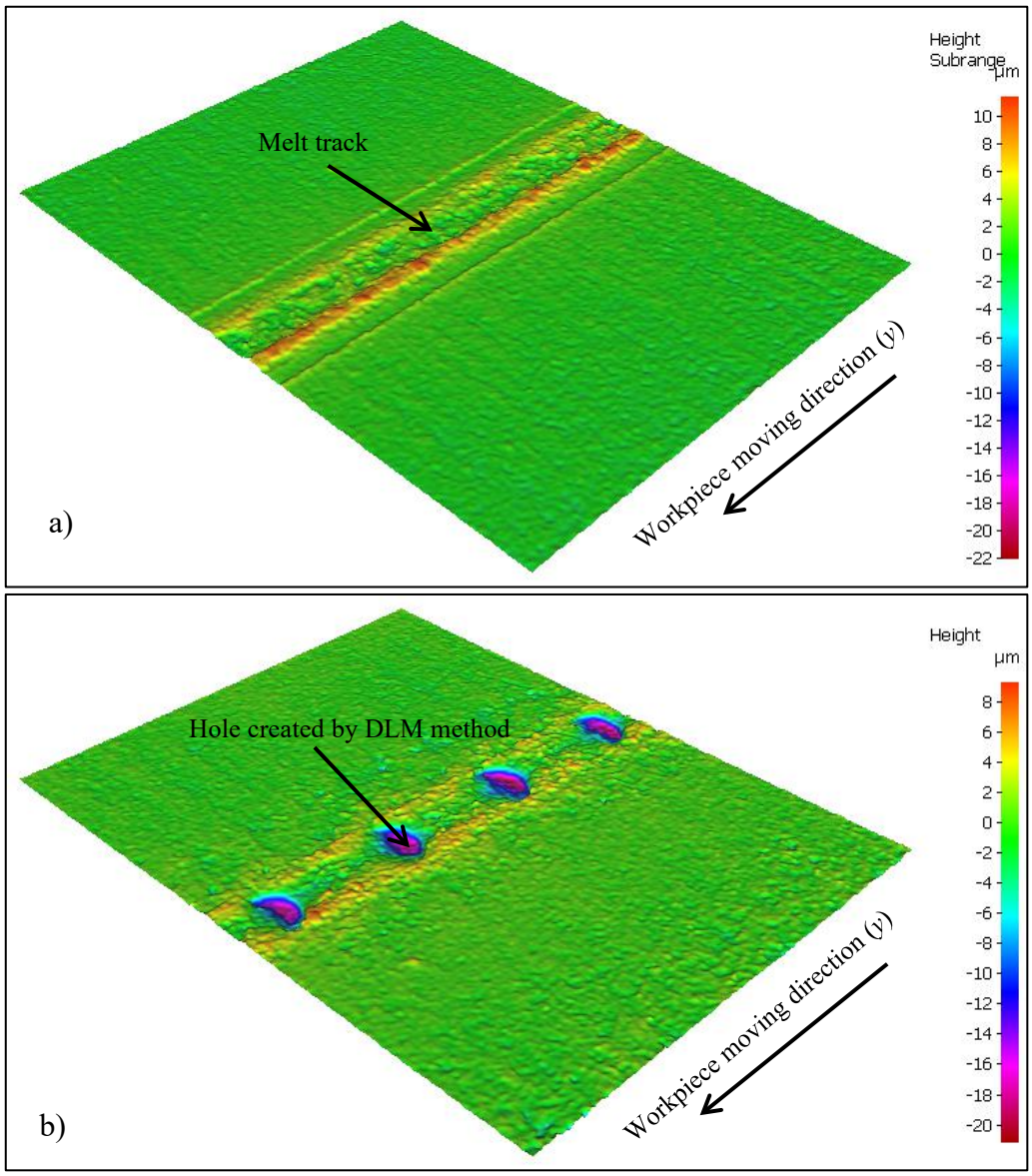

Figure 4-10 3D surface profiles a) melting only at 3 mm/s, b) DLM method at 3 mm/s

The offset distance between the two laser beams centres was studied when the melt ejection laser beam centre was relatively located behind (- sign) and ahead (+ sign) of the melting laser spot centre. The effect of offset distances on the maximum hole depth is shown in Figure 4-11. The molten pool depth is governed by the cooling time and the conduction time. This affects the time required for maximum molten material depth when the ejection pulse is delivered. The maximum depth shifts behind the moving spot centre (Cline and Anthony, 1977).

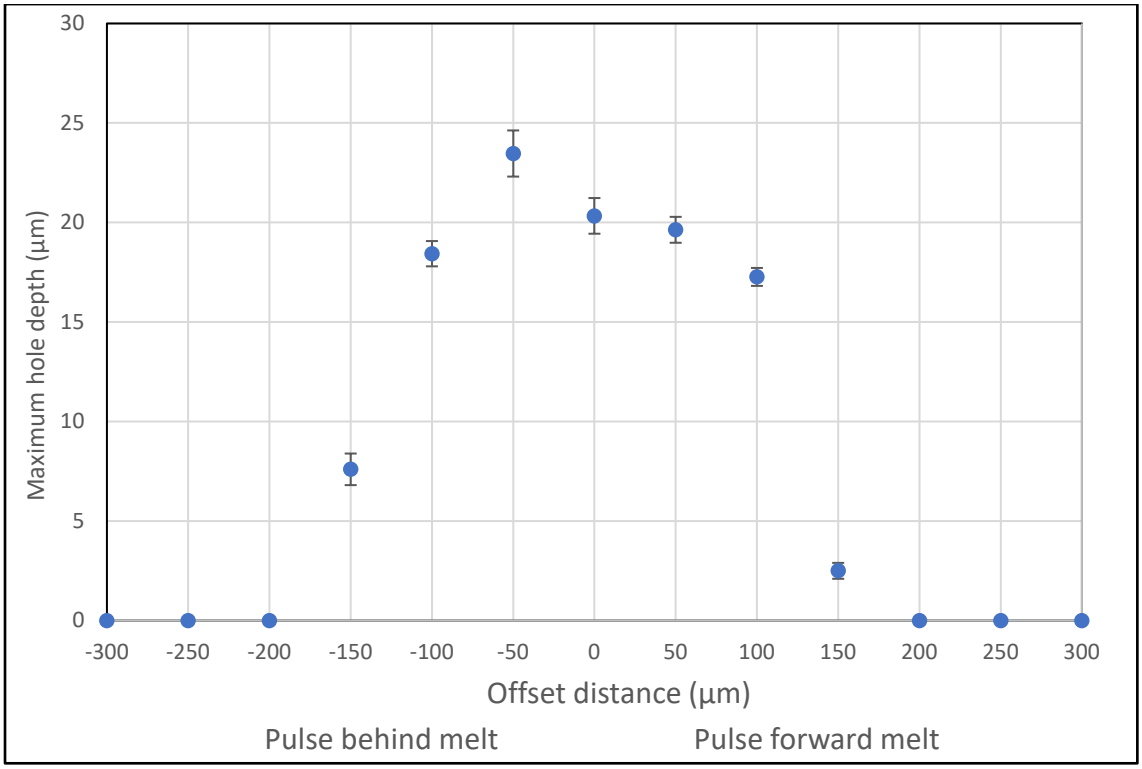

Figure 4-11 The effect of offset distance in DLM method on the maximum hole depths at 3mm/s velocity.

Material ejection occurred at distances between -150 to +150 µm with the maximum 23.5 µm hole depth at -50 µm offset distance. The hole depth decreases significantly when the offset distance increases more than ±100 µm. No holes were formed beyond ±200 µm as the molten material will have fully solidified by this point and therefore cannot be ejected.

Cross-sectional images of the DLM holes are shown in Figure 4-12-b and Figure 4-13-b for melting velocities of 3 and 25 mm/s respectively. The hole depths are 23.5 µm at 3 mm/s velocity, and 19.4 µm at 25 mm/s velocity. These figures provide additional evidence of clean material ejection to the 3D surface profiles. There is no deposition of material at the edges of the features as would be expected by the existing quasi-steady state liquid ejection models of these types of processes (Robin and Nordin, 1976; Shui, 1978).

Not all of the molten material was ejected, however, and residual molten material along the bottom of the hole can be seen in Figure 4-12-c and Figure 4-13-c. The maximum thickness of residual material was measured as 8.0 and 1.6 µm for velocities 3 and 25 mm/s respectively. The pulsed laser applied to the molten pool surface in the DLM method results in an ejection of 73% and 93% of the molten material at melting velocities of 3 mm/s and 25 mm/s, respectively.

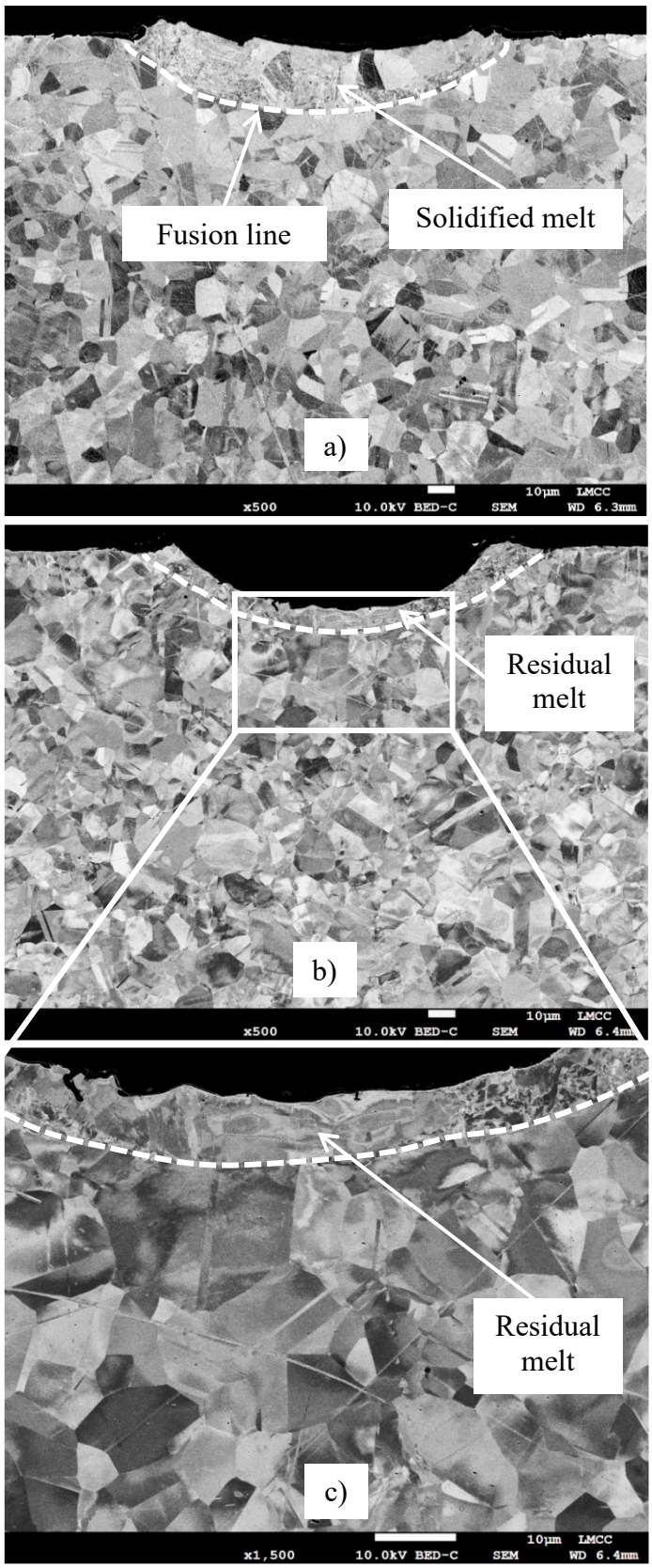

Figure 4-12 SEM micrograph cross-section of DLM method for 3 mm/s velocity. a) melt cross-section with melt depth 30 µm (b) and the hole created by DLM method with depth 23.5 µm (c) the residual melt material.

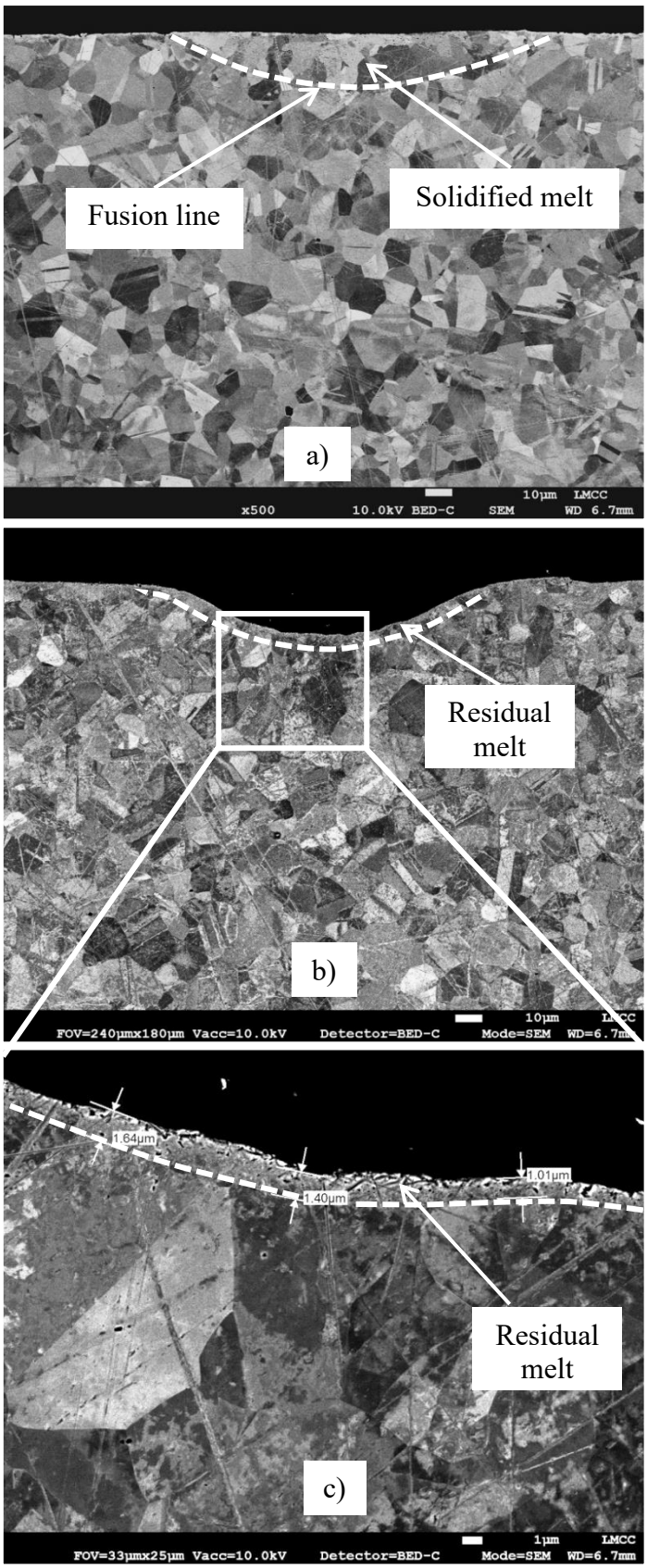

Figure 4-13 SEM micrograph cross-section of DLM method for 25 mm/s velocity. a) melt cross-section with melt depth 21.4 µm (b) and the hole created by DLM method with depth 19.4 µm (c) the residual melt material.

Analysis of the quality shows that the DLM holes were found to be free from microcracks and without any re-deposited material on the surface. Moreover, the micrographs show low porosity in the solidified molten material. The micrographs show no change in grain size content in the areas around the hole relative to the base metal. This is because no phase transformation was observed in the HAZ since the austenitic stainless steel is not transformable (Pouranvari and Marashi, 2009). The molten pool is mainly of columnar grain nucleated at the fusion line and grown towards its centre.

It is concluded from the initial experiment for DLM method at moving mode that DLM method can eject the molten material. DLM will be conducted on the more applicable stationary mode and to allow comparison with theory in the following section.

4.4 DLM in Stationary Mode: Experimental Setup and Results

This section presents work to implement the DLM method in practice and compares the energy efficiency with conventional ablative machining found in the literature. The quality of the DLM method is assessed using metallurgical techniques. Two experimental set-ups are conducted to investigate the efficiency of DLM in practice. First molten pool generation using only the CW laser beam is explored to investigate how the melt pool develops with time. Secondly, the combination of both lasers in DLM method is investigated as a means to achieve liquid phase ejection and optimum efficiency. Section 4.3.3.2 presented the effect of nanosecond pulsed laser on the material surface without melting to examine its machining capability.

4.4.1 Experimental Setup

The same two lasers used at moving mode was used in this stationary mode (see Section 4.3.1). A CW fibre laser, the “melting laser” to create a molten pool and a Q-switched Nd: YAG laser, the “ejection laser”, provided the necessary impulse required to eject the molten material.

The fibre laser was internally triggered to provide a 10 Hz pulse stream of variable pulse width. The light scattered from the workpiece surface was detected by a PIN photodiode. The signal from the photodiode was sent to a pulse generator to trigger the ejection laser with a programmable delay. The experimental setup of the time synchronisation is illustrated in Figure 4-14.

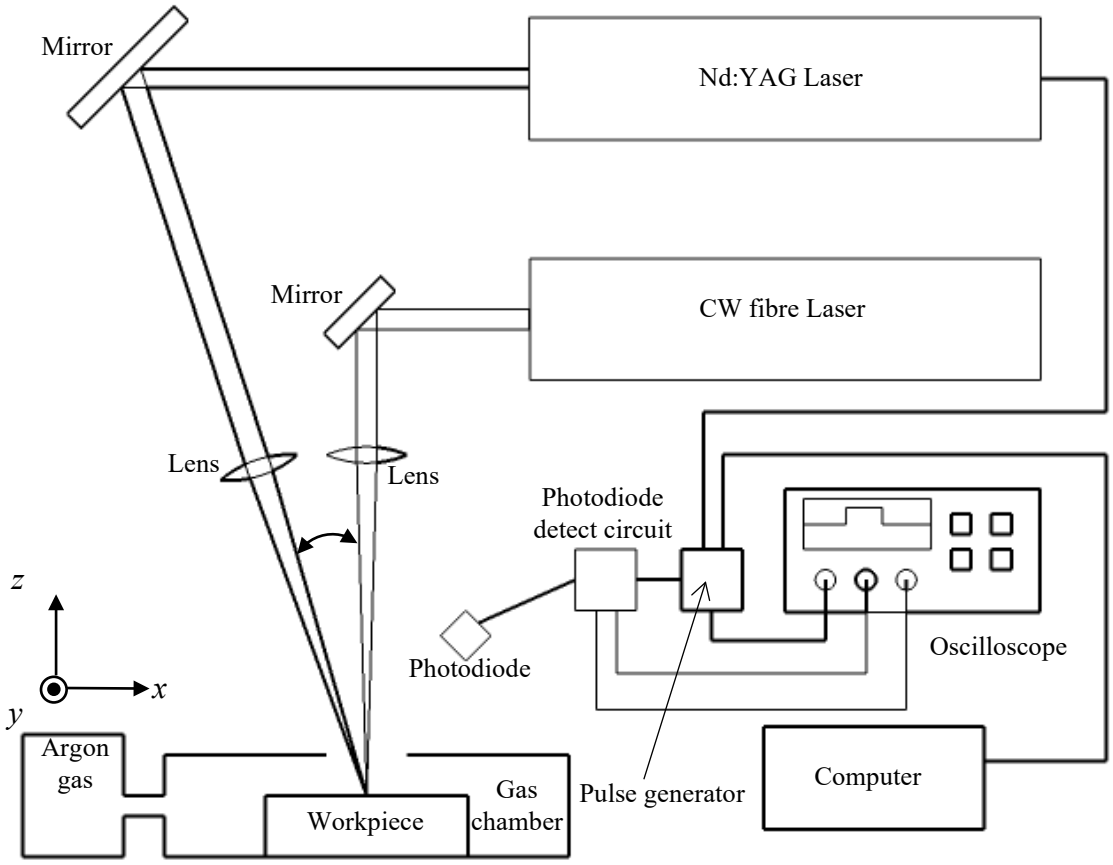

Figure 4-14 Schematic of the DLM setup shows the synchronisation between the two lasers.

The actual delay time is defined as the interval between the start of the melting and ejection pulse. The delay time was monitored by the photodiode and measured using an oscilloscope. In these experiments, the workpiece is mounted on a stationary workstation stage and the two stationary laser beams are focused at the same position as shown in Figure 4-15.

The melting process was conducted at a power of 18.9 and 5 to 68.1 ms melting time range to determine the melt depth. 316 stainless steel with 3 mm thicknesses was used in this study to make suitable comparisons to the literature on conventional nanosecond laser processing efficiency (Herfurth *et al.*, 2007; Gay *et al.*, 2009; Leitz *et al.*, 2011). To prevent oxidation, all the experiments in this study were carried out with argon shielding gas. The argon gas was introduced into an open-top box where the workpiece was located with the same flow rate and the pressure described in Section 4.3.1.

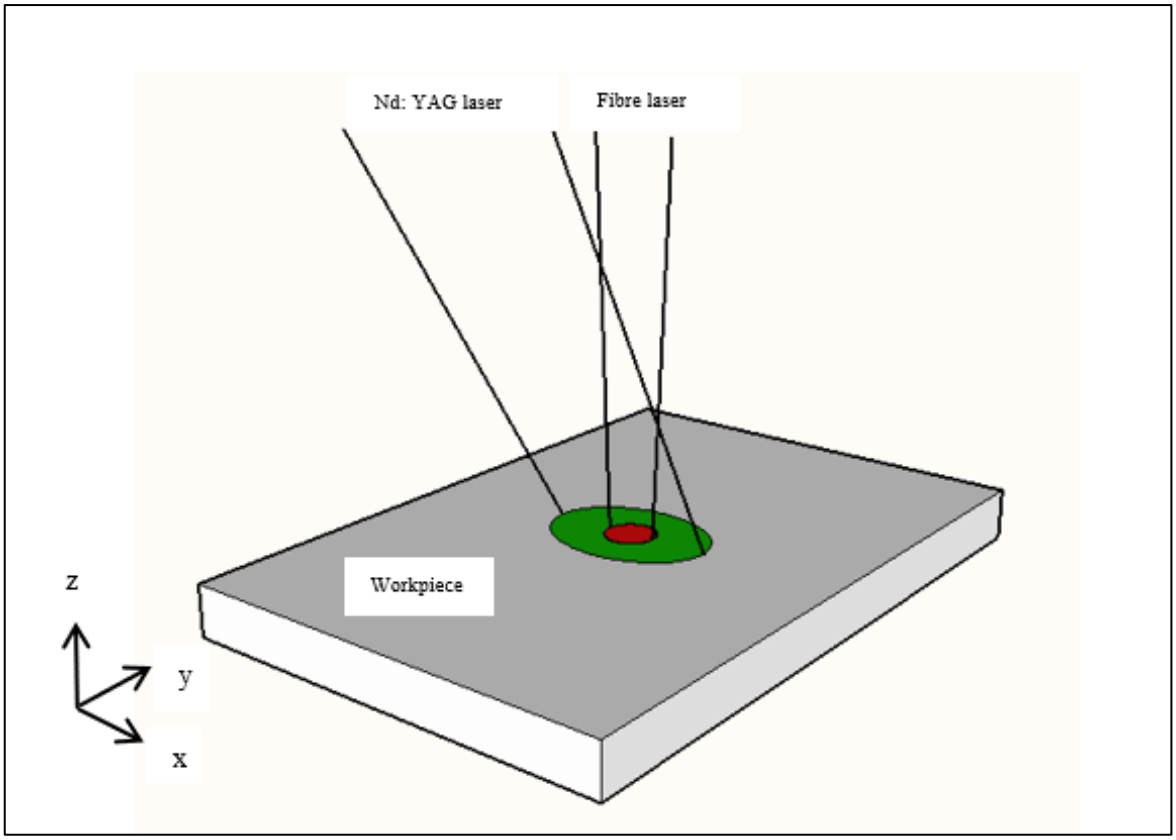

Figure 4-15 Schematic diagram of DLM method setup.

In each case, the geometry and metallurgical features of melt cross-sections were analysed using an optical microscope. All images were taken from central cross-sections and in each show the maximum melt depth achieved. Workpieces were prepared for microstructural analysis by mounting the workpiece in conducting bakelite, mechanically grinding using series of papers of 320, 600, 1200 and 4000 grit SiC grades, polishing using 9, 3 and 0.050 µm diamond suspension and etching using Kalling's No. 2 for approximately 5 s. The recast molten material and HAZ are used in the analysis as a quality indicator.

4.4.2 Results

4.4.2.1 Effect of Melting without Ejection

Figure 4-16 shows the depth of melt pools created with 5 – 68.1 ms melting times to a maximum melt depth of 31 µm. The theoretical results, calculated using the laser irradiance 35 kW/cm^2 above, align with the experimental melt data at small melt depths but depart significantly from the linear theoretical trend when the melt pool depth increases beyond 20 µm. It is noted that Cohen's model is a one-dimensional model of uniform heating, and heat transfer is affected only by conduction. In this experiment, a Gaussian beam is used, and at

$S > 20$ µm, the melt depth is a significant proportion of the beam radius, w=131 µm. Consequently flow generated by surface tension driven convection known as the Marangoni effect can be expected with a small contribution from the buoyancy force (Basu and DebRoy, 1992) and more efficient heat transfers the heat from the centre to the edge (Mazumder, 1991).

Figure 4-17 shows cross-sections of the solidified melt pools obtained at low (9 ms) and high (27.2 ms) interaction times. A relatively flat surface can be seen at low interaction times, whereas a significant change to the melt surface cross-sectional shape can be seen at 13.6 ms (and beyond). This suggests that the process at this point closely resembles the uniform model of conduction limited melting defined by Cohen. At high interaction times, the surface starts vaporising and taking the latent heat of vaporisation that results in a slight increase in the melt depth. These results show similar trend to the results of melting at moving mode presented in Figure 4-7. The laser irradiation time of this stationary mode can be compared by the interaction time, $t = 2w/v$ for the case of the melting in moving mode, where w = 131 µm is the laser beam radius at a position where the intensity falls to $1/e$ times its maximum value and v is the laser melting velocity.

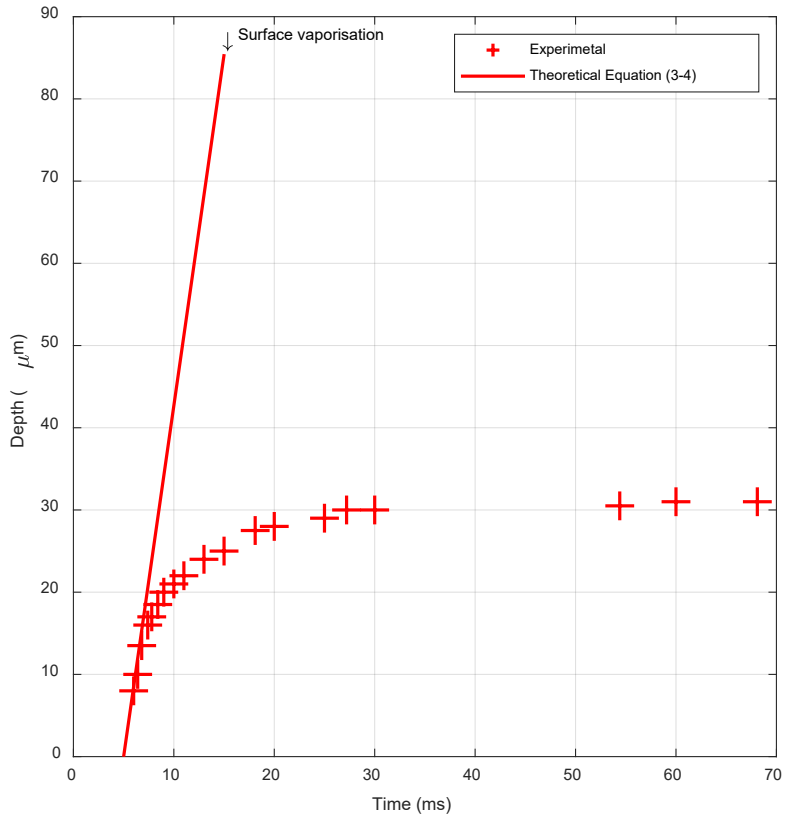

Figure 4-16 Melt depth as a function of melting time: Theory and experiment.

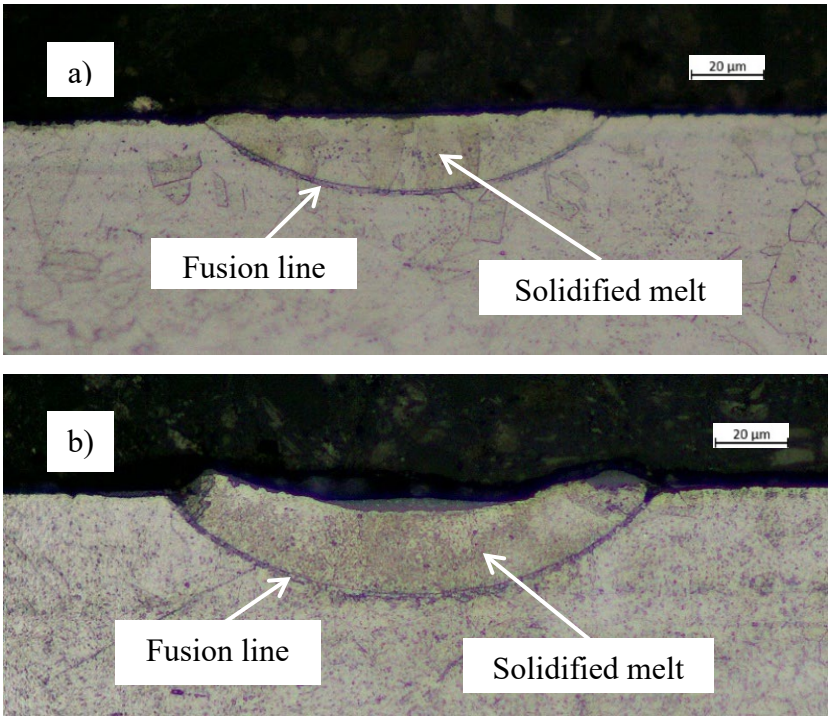

Figure 4-17 Micrograph cross-section of melting only without ejection laser at a) 9 ms and b) 27.2 ms melting times with maximum melt depth of 20 and 30 µm, respectively.

It is clear from Figure 4-16 that optimum efficiency does not occur at the theoretical maximum melt-depth. In order to find this optimum, the specific energy required for melting, $E_{\text{melt\_exp}}$, was calculated for the range of experimental interaction times t_{exp} 6 to 68.1 ms defined such that,

$$E_{\text{melt\_exp}} = \frac{It_{\text{exp}}}{z\rho} \tag{4-2}$$

where z is the maximum experimental melt depth.

Noting that the energy absorbed by the surface after time, t, by the laser is, $E = IAt$, after manipulation of Equations (3-4), (3-5) and (3-7) from Cohen's analysis, the theoretical specific energy required to melt material, $E_{\text{melt\_theory}}$, was found that is given by Equation (4-3) and presented with $E_{\text{melt\_exp}}$ in Figure 4-18.

$$E_{\text{melt\_theory}} = 7.14L_{\text{m}}\frac{t}{(t - t_{\text{m}})} \tag{4-3}$$

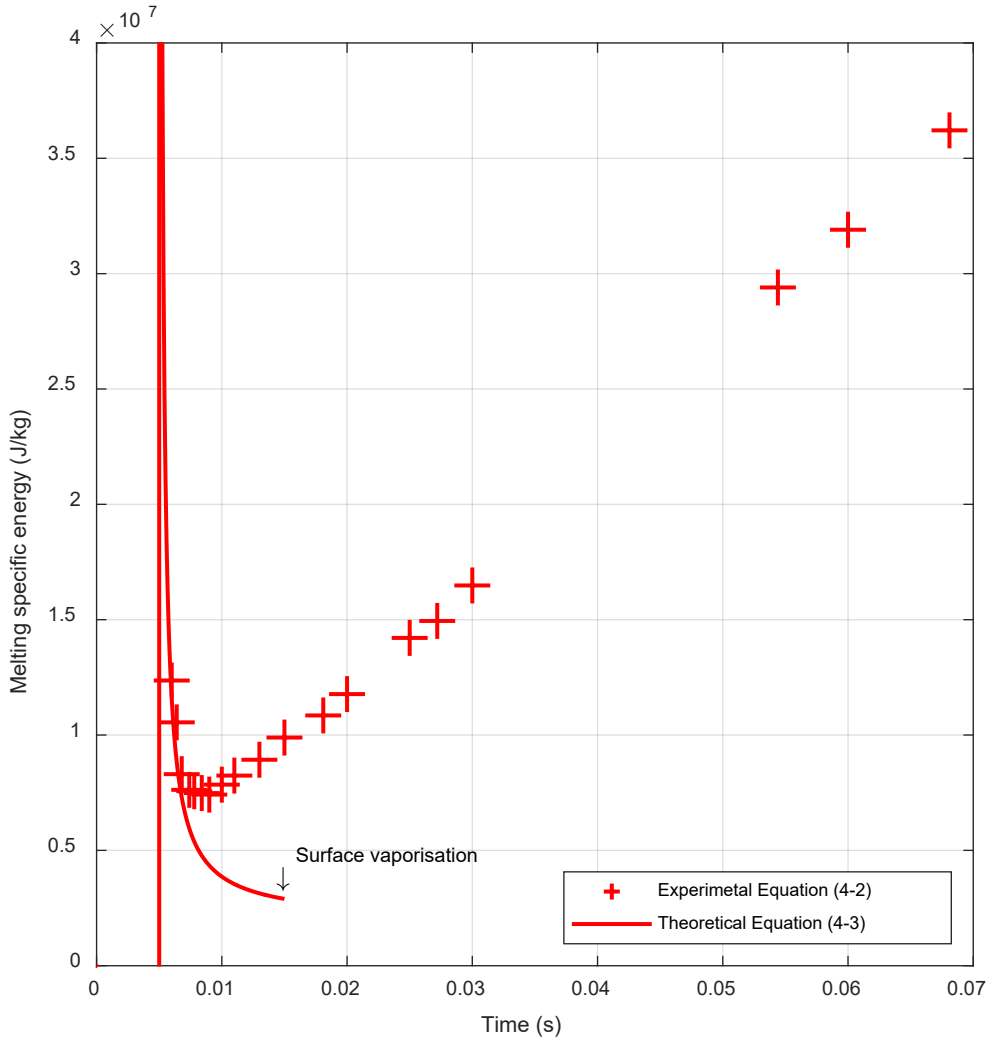

Figure 4-18 Comparing experimental and theoretical results of melting specific energy

Figure 4-18 shows that the lowest specific energy is observed at 9 ms, not 15 ms as Cohen's analysis predicts. At this 9 ms melting time, the melt depth is approximately 20 µm and was used for the DLM comparison explained in Section 4.4.3.

4.4.2.2 DLM method

The DLM method was used to eject material at experimental melting times in the range of 9-60 ms. The ejection laser pulse was maintained at 50 mJ and laser fluence of 53 J/cm^2. Table 4-3 gives results from Alicona measurements for the different melting times the melt depth, hole depth by DLM and the residual melt thickness. The combined DLM method created holes with 18-28 µm maximum depth range. Four repeats were made of each DLM melt time to calculate the mean and standard deviation.

Table 4-3 DLM method results

Melting time (ms)	9	11	13	15	20	25	30	60
Melt depth (µm)	20.0	22.0	24.0	25.0	28.0	29.0	30.0	31.0
Hole depth mean (standard deviation) (µm)	18.4 (0.4)	19.9 (0.9)	21.8 (0.1)	22.9 (0.3)	25.0 (0.3)	25.6 (0.3)	26.5 (0.3)	27.4 (0.5)
Residual melt thickness (µm)	1.6	2.1	2.2	2.1	3.0	3.4	3.5	3.6

3D surface profiles of the DLM holes were generated using the Alicona Infinite-Focus microscope. The profiles were used to measure the depth of the holes as shown in Figure 4-19. The maximum melt depth is used in the calculation. Figure 4-20 shows 3D images of the hole created at 9 ms melting time. The 3D image shows that the molten material was ejected by the effect of molten pool surface vaporisation using the 5 ns pulse, with a small amount of redeposited material at the workpiece surface along the periphery of the created hole.

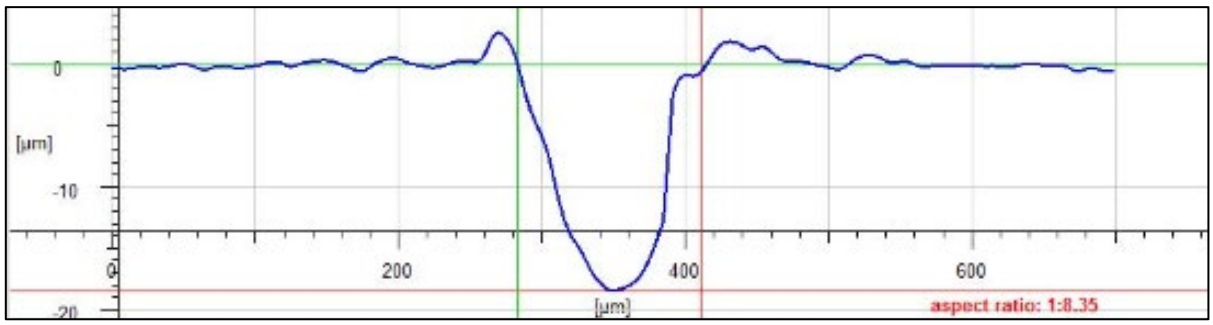

Figure 4-19 2D surface profile taken by Alicona from the centre of the hole created in DLM method at 9 ms melting time

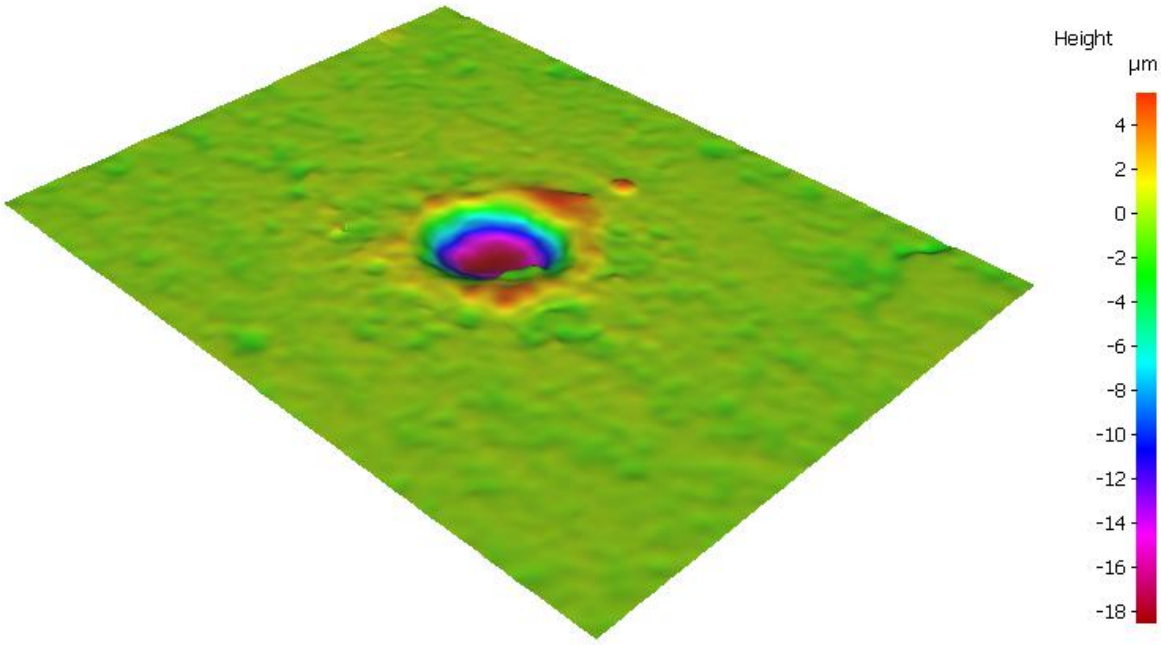

Figure 4-20 3D surface profile of DLM method at 9 ms melting time

Cross-sectional images of the DLM hole, created at 9 ms melting time, are shown in Figure 4-21. This figure provides additional evidence of clean material ejection to the 3D surface profiles. There is a small amount of deposition of material at the edges of the features as would be expected by existing quasi-steady-state liquid ejection models of these types of processes (Robin and Nordin, 1976; Shui, 1978). However, there is an increase in the residual molten material is that not ejected as melt depth increases as presented in Table 4-3.

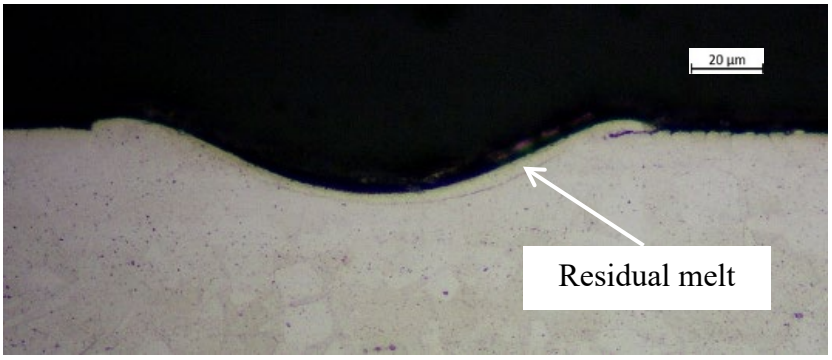

Figure 4-21 Micrograph cross-section of the hole created by DLM method at 9 ms melting time with a maximum hole depth of 17 µm.

Analysis of the material quality shows that the DLM holes were found free from microcracks and without any re-deposited material on the surface. Moreover, the micrographs show low porosity in the solidified molten material.

4.4.3 Discussion

The specific energy of experimental DLM results was calculated from the sum of the specific energy by a CW laser for the melting duration and the single ejection pulse given by:

$$E_{\text{total\_exp}} = \frac{It + I_{\text{absorbed\_eject}} t_{\text{eject}}}{\rho l} \tag{4-4}$$

Where l is the maximum DLM hole depth, t_{eject} is the ejection pulse duration and $I_{\text{absorbed\_eject}}$ is the absorbed irradiance of the ejection beam. $I_{\text{absorbed\_eject}} = (1-r_{\text{eject}})I_{\text{eject}}$, where I_{eject} is the irradiance of the ejection beam and r_{eject} is the reflection coefficient of ejection laser. The reflection coefficient value used in the calculations is taken from measurements by Bergstrom, Powell and Kaplan, (2007) for 316 stainless steel. This result is valid for Nd:YAG (532 nm) laser at room temperature. The roughness of the workpieces used in this work is similar to those used by Bergstrom, Powell and Kaplan, (2007) (see Section 3.2). Although it is known that reflectivity decreases with temperature increase (Xie *et al.*, 1997), the exact value for the ejection pulse on the melt pool is unknown, and room temperature values will be assumed. The reflectivity value used was 56.2% for the ejection laser.

The results from the theoretical lossless vaporisation model Equation (3-1), DLM theoretical model E_{melt} Equation (3-7) plus E_{eject} in Equation (3-10), experimental DLM results in Equation (4-4), and the conventional processing results from Gay *et al.* (2009), Leitz *et al.* (2011), and Herfurth *et al.* (2007) are shown in Figure 4-22. The figure shows the energy (J) against the material removal mass (kg).

The results of DLM at different melt depth are presented to show its relation to the theoretical DLM curve (black line). At the most efficient melting time of 9 ms, the total energy absorbed by the workpiece in the DLM method is 9.73×10^{-7} J and the mean mass ejected by the DLM method is 1.15×10^{-13} kg giving specific energy of 8.46×10^{6} J/kg. Of the total energy in the optimised DLM method, 95% of the energy was delivered in the melting process and 5% in the ejection process.

This result compares favourably with other researchers who have studied the removal of material conventionally from stainless steel via vaporisation processes (Herfurth *et al.*, 2007; Gay *et al.*, 2009; Leitz *et al.*, 2011) detailed in Section 4.2.2.

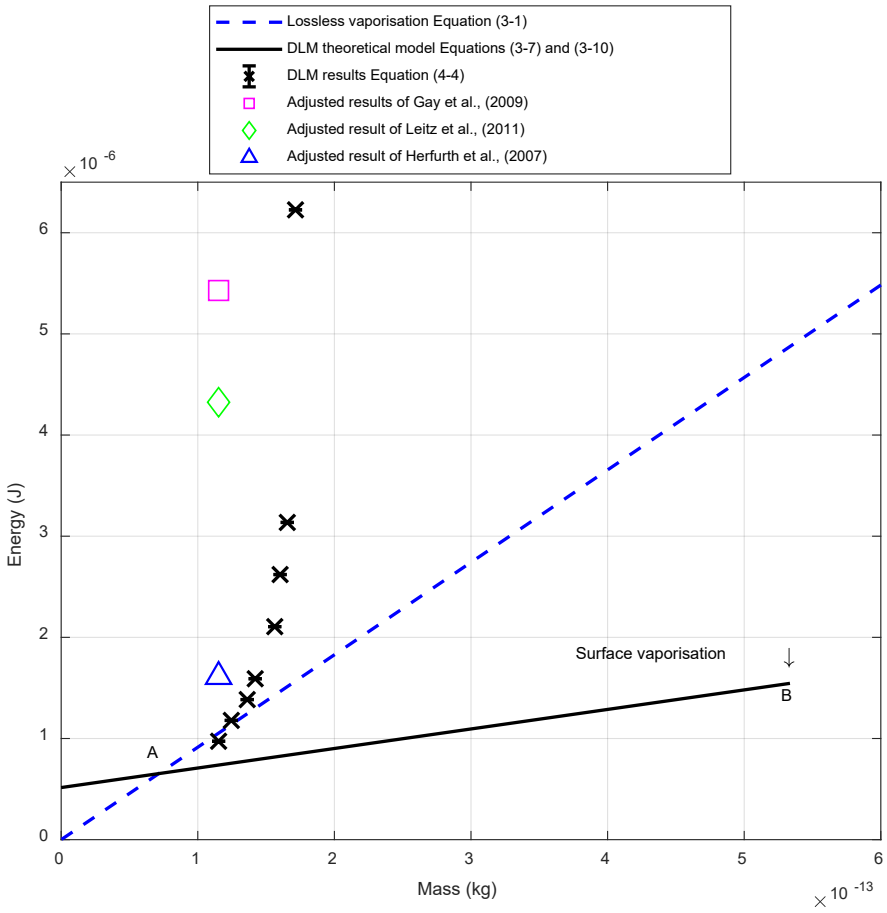

Figure 4-22 Comparison of DLM and conventional processing energy efficiency.

As mentioned in Section 4.2.2, the theoretical model of the lossless vaporisation presented in Figure 4-22 is used to describe the energy required for mass removal by direct vaporisation (ablation). The curve is presented for 316 stainless steel and other types of stainless steel despite a slight difference in the material properties. This lossless vaporisation curve was compared to the results from literature in the following order from high to low specific energy Gay *et al.* (2009), Leitz *et al.* (2011), and Herfurth *et al.* (2007).

It is clear from Figure 4-22 that there is a significant difference in specific energy between these processes from literature. This may be justified by the difference in the laser irradiance that determines the dominant mechanism to be vaporisation or melt ejection (Chan and Mazumder, 1987). For the same laser milling process and the same material, Herfurth *et al.* (2007) used less laser irradiance than Gay *et al.* (2009). Other parameters play an important role in the material removal efficiency such as frequency, scanning speed (Herfurth *et al.*, 2007) and pulse duration determines the energy lost via conduction and the amount of melt material that becomes a recast material at the end of the process (Zhang and Faghri, 1999).

The DLM result at the most efficient melting time, 9 ms, was compared to the results from the literature to show the improvement in the material removal efficiency that this work aims to achieve. All the results of Herfurth *et al.* (2007), Gay *et al.* (2009), and Leitz *et al.* (2011) were presented for the same DLM method mass at melting time 9 ms to make a clear comparison. It is shown in Figure 4-22 that the energy used in DLM is 60% of the energy used by Herfurth *et al.* (2007), 23% of the energy used by Leitz *et al.* (2011), and 18% of the energy used by Gay *et al.* (2009), to remove the same mass.

4.4.4 Summary of DLM Experiments in Stationary Mode

This section presented a combined analysis of an energy model and experimental data. It has also directly compared the energy efficiency of this process to conventional machining and shown evidence of clean material removal.

Two lasers were used in this study, a continuous wave laser to create a molten pool with melt depths from 8 to 31 μm, while a nanosecond pulse laser was used to eject the molten material by vaporising the molten pool surface to generate recoil pressure. Theoretical calculations were performed for the melt pool size against the melting process and compared with the experimental melt depths. The highest melting efficiency was found at 9 ms melting time generating 20 μm melt depth. The pulsed laser was applied on the molten pool surface in the DLM method resulting in an ejection of 90% of the molten material. This created holes in the surface of 316 stainless steel at a specific energy of 8.46×10^6 J/kg. The calculation of melting energy presented was used to identify that total energy used in the DLM method. It was found that 95% is the energy used in melting and 5% in ejection. It was also shown theoretically that there would be a reduction in total energy consumption of 3 times comparing DLM method to vaporisation machining. This was confirmed by comparing the DLM results of this work to conventional laser processing found in the literature. The results showed that the method presented is able to increase material removal efficiency compared with the conventional processes by approximately 2 to 6 times.

4.5 Summary and Conclusion

Conventional laser micromachining was studied on 316 stainless steel. The results of specific energy for laser milling experiments and available experimental data of stainless steel from the literature were identified and compared. The milling process was shown to be less efficient than conventional laser micromachining. This is because it was not optimised for all

the parameters and was limited by the available maximum pulse energy in the fibre laser. The machining quality for milling process experiment showed residual molten material inside the created pocket. Initial DLM was conducted in moving mode and showed that the DLM method can eject the molten material. As required, DLM was conducted on the more applicable stationary mode allowed direct comparison with other processes in the literature. It showed that the method presented can increase material removal efficiency compared with the conventional micromachining. This work shows that a nanosecond pulse can achieve the impulse required for ejection in the models of Robin and Nordin (1976) and Shui (1978). While this work presents the results of a more efficient material ejection process, it does not fully explain the physical mechanism for the ejection process. In the following chapter, the ejection mechanism is studied.

5 MELT EJECTION MECHANISM

The previous chapter presented the results of an efficient material ejection using DLM method. The experimental results showed that a nanosecond pulse can achieve the impulse required for melt ejection. However, the results do not fully explain the physical mechanism for the melt ejection process. This chapter provides insight into the mechanism of melt ejection. The following section presents models of melt ejection found in the literature and their application to DLM. The analysis in this chapter starts by investigating the dynamics of the melt ejecta using high-speed camera imaging. This is followed by theoretical and experimental results of the new model to facilitate its incorporation into the existing models from the literature of melt ejection mechanism.

5.1 Literature Review of Melt Ejection Models

After the novel DLM experiment proposed by Fox (1975), a theoretical investigation was made of the melt ejection mechanism (Robin and Nordin, 1976; Shui, 1978; Yuan *et al.*, 2018).

Robin and Nordin investigated, theoretically, Fox's initial experiment to calculate the minimum impulse required for melt ejection. In Robin & Nordin's model, it is assumed that the molten material is ejected from the irradiated surface as an annular flow and arbitrarily assumed the thickness of flow is one-tenth of the hole radius as illustrated in Figure 5-1. It also assumed that the molten material at the surface is thin enough to be fully ejected by the pulse laser and the material is accelerated to its terminal velocity during the pulse time.

Robin and Nordin estimated a minimum impulse of 2×10^{-5} N·s required to eject an aluminium melt layer. Microsecond duration laser pulses, with intensities greater than 10^{8} W/cm^2 can generate impulses 10 to 12×10^{-3} N·s (Metz et al., 1975) which significantly exceed the minimum impulse threshold. This suggests that low energy short pulses should be capable of molten material ejection and above this value of peak irradiance the difference in the impulse response of different materials is insignificant (Phipps et al., 1988).

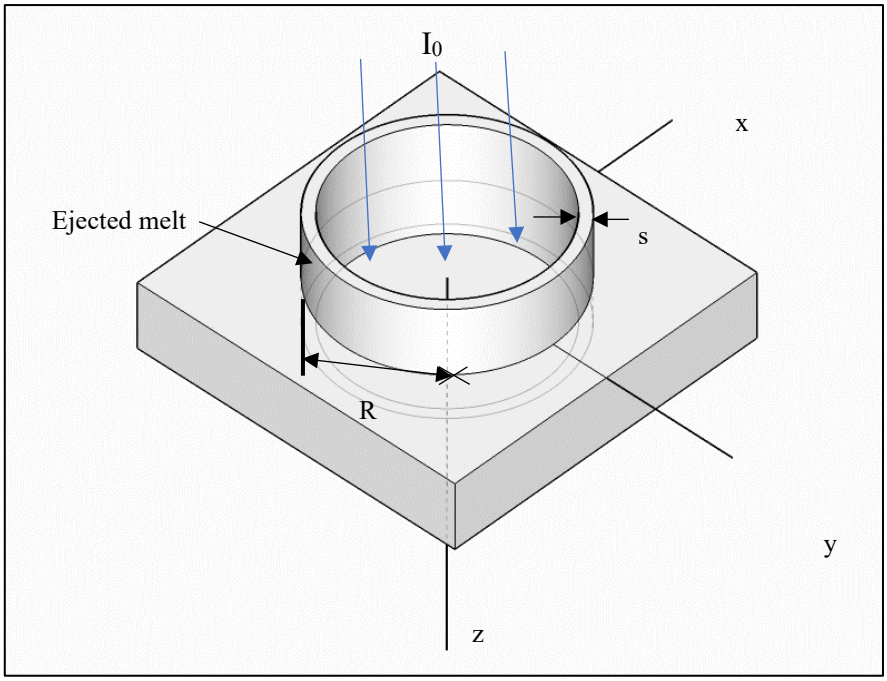

Figure 5-1 Schematic illustration of Robin & Nordin's model for melt ejection.

In Robin and Nordin's model, the minimum impulse required to remove the melt material was calculated based on momentum conservation. The time considered in this calculation was the time to create the melt layer, not the time required to eject the material. The minimum impulse is estimated based on the assumption that ejection time is much less than the time used to melt this layer to ensure rapid removal of the material for a sequence of ejection pulses during the melting. The results are based on previous experimental results of an impulse generated by the same irradiance used in the calculation.

Another model was developed by Shui (1978) to estimate the pressure, effective time and specific impulse to achieve specific melt removal fraction from the molten material produced by CW laser. This model considers the transient behaviour of melt that is not considered in Robin and Nordin's model. Shui assumed that the fluid material as if it is between two plates and is removed by the action of moving of the upper plate applying pressure to the lower fixed plate as shown in Figure 5-2. An unrealistic large momentum for melt ejection is predicted by Shui's model that contradicts Robin and Nordin's model and Fox's experiment.

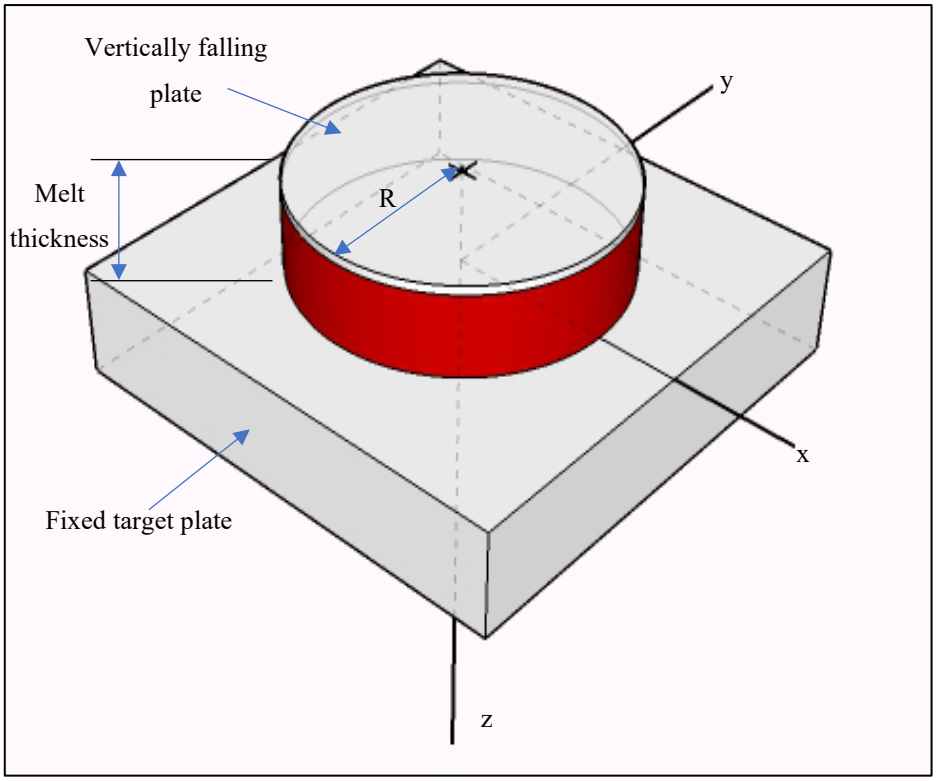

Figure 5-2 Schematic illustrations for Shui's melt ejection model.

Recently, Yuan *et al*., (2018) studied the influence of the spot size combination on the micromachining morphology in the DLM method which provides further insight into the melt ejection problem. Their results showed that the molten material is ejected when the ejection pulse diameter is larger than the melt pool diameter which is consistent with Fox's and the DLM experiments in this research. Yuan et al. showed that the molten material is removed more uniformly, and a little amount is solidified at the edge of the created void. On the other hand, when the ejection pulse diameter is smaller than the melt pool diameter, the molten material is accumulated around the hole edges caused by the melt flow with a volume higher than the hole due to the phase change. The melt flow appears to occur because the temperature and the recoil pressure at the melt pool centre are much higher than its value at the melt edges. This makes a significant difference in the surface tension. The Marangoni effect migrates the material from the low surface tension to the high surface tension at the sides. This contradicts with the assumption made by Robin and Nordin for the ratio between the two laser spot sizes.

Yuan *et al*. investigated the ejection using a shadowgraph technique showing the shockwave on the melt surface that generates the recoil pressure causing the material migration. This shockwave is generated by the plasma created during the melting process that expands

rapidly by the action of ejection nanosecond laser. For the results when the nanosecond laser covers the entire molten pool surface and the recoil pressure confines the melt flow to the sides, the images show strong turbulence on the surface. The images from Yuan *et al*. do not show the ejected molten material, however, and in their analysis, it is not clear how the molten material is ejected. They argue that the melt splashes by the mechanical effect of the recoil pressure when it is higher than the surface tension.

The mechanisms involved in melt ejection using DLM method are rather complex and are at present poorly understood. There is still uncertainty in the ejection models. Robin and Nordin (1976) and Shui (1978) assume the molten material is ejected from the melt pool periphery without considering the pressure gradient from the melt pool centre. Yuan *et al*.'s images do not show the ejected molten material and it is not clear how the molten material is ejected. Accordingly, it is suggested to study the effects of the pressure pulse created by rapid surface vaporisation.

In this research, it is hypothesised that the material is ejected by the effect of the compression pulse generated at the surface and travelled through the target material. Part of this pulse is reflected at the liquid-solid interface depending on the difference in impedances between solid and liquid phases. Subsequently, it is converted into a tension pulse at the free surface. Upon this tension pulse, spallation can occur ejection of the molten material takes place when the tensile pulse stress exceeds the tensile strength of the liquid material. Theoretical analysis and simulation of the acoustic pulse are introduced in this chapter. The presented hypothesis was validated theoretically (simulation) and experimentally. Also, sectioning of the melt pool and machined workpiece features provides some useful evidence of the ejection mechanism.

5.2 Imaging of Ejection Process using High-speed Camera

In order to understand the behaviour of the ejecta, the melt ejection process in DLM method was first investigated using a high-speed camera imaging with the capability of 10,000 frames per second was used. The images are analysed for the direction of the melt ejecta and the ejected melt velocity.

5.2.1 Experimental Setup of High-speed Camera

In this experiment, the same experimental setup in the stationary mode of DLM method was employed as explained in Section 4.4.1. Also, this experiment was conducted on the same 316 stainless steel workpiece at the optimum melting time 9 ms that produced 20 μm melt

depth. Figure 5-3 illustrates the experimental setup. The ejecta was imaged using Photron Fastcam SA-3 camera with accompanied Photron software (Photron Fascam Viewer) at a rate of 10000 frames per second with 1 × 2 mm frame dimensions. During the imaging process, an LED light was used to illuminate the target imaging area. Two filters were placed in front of the camera to protect the camera from laser damage and allow only the LED illumination wavelength through: A notch filter removes 532 nm ejection laser wavelength; a short-pass filter transmits all wavelengths shorter than 900 nm that (i.e is less than the wavelength of the melting laser 1064 nm). The high-speed camera starts taking images by the start irradiation time of the ejection laser (Nd:YAG laser).

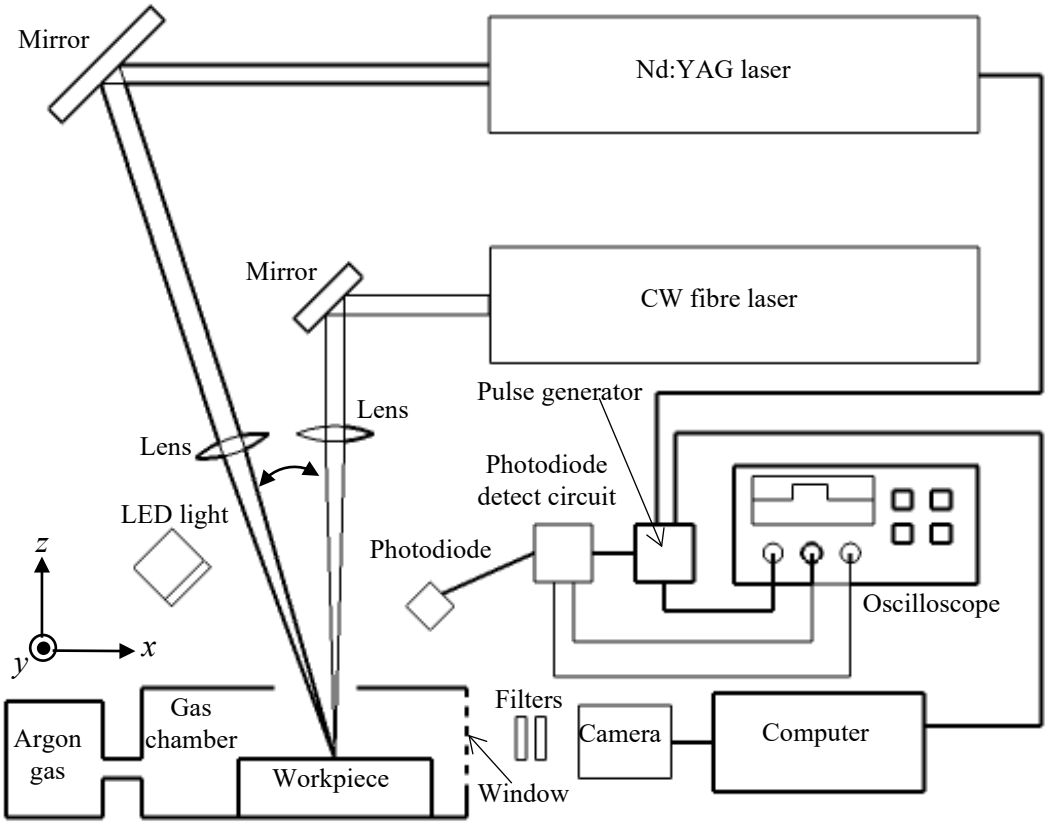

Figure 5-3 Schematic of the DLM and high-speed camera setup.

5.2.2 Results of High-Speed Camera Imaging

Results obtained by tracking of individual droplet through successive frames from high-speed camera photography film at 10000 frames per second and 98μs exposure time are shown in Figure 5-4. The frame in Figure 5-4-a shows the plasma created above the workpiece surface

by the effect of ejection nanosecond laser. The frames in Figure 5-4-b-d shows the motion-blurred, ejected droplets. The droplet velocity can be estimated by dividing the length of these images by the exposure time. For example, those visible in the frames b-d have velocities in the range of 2-8 m/s. The two-dimensional image shows the ejection of the droplets at different angels.

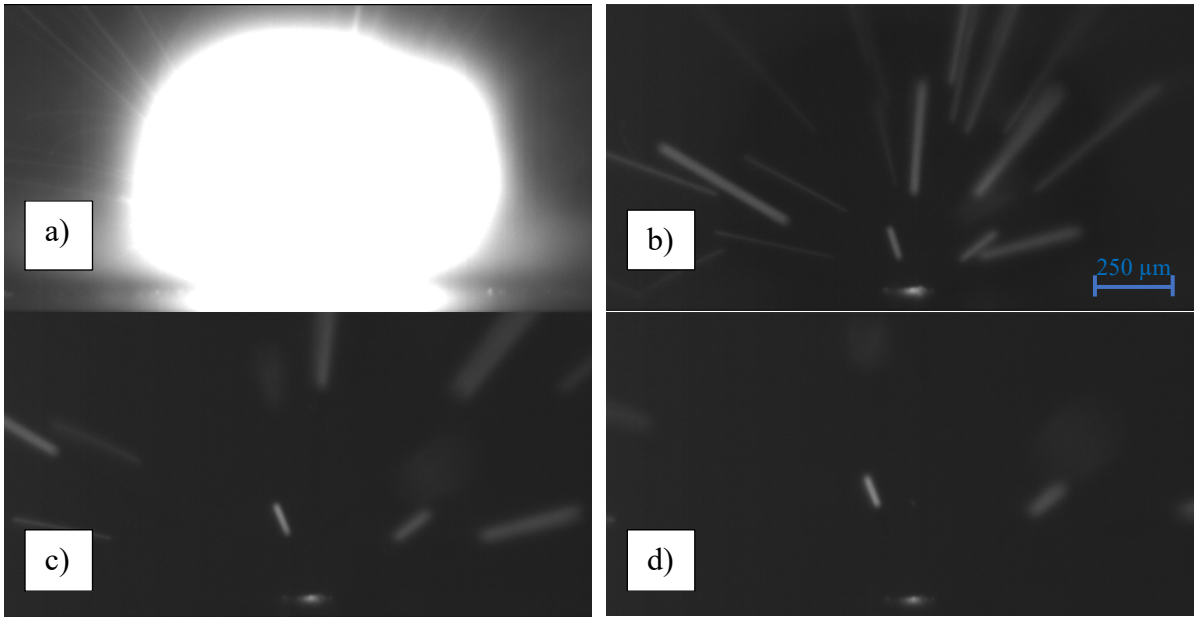

Figure 5-4 Sequence of frames for the ejection process taken by high-speed camera with frame separation of 100 µs and 1×2 mm frame dimensions.

These images give information about ejection behaviour. For instance, the images show that the molten material is ejected in discrete droplets at different angles that contradicts with the models introduced by (Robin and Nordin, 1976; Shui, 1978); as both models assumed that the molten material flows from the melt pool periphery. While these images may not quite prove the hypothesis concerning the limited capability of the high-speed camera to be operated at very higher frame rates that shows the time of start ejection from the start effect of the ejection pulse laser, it indicates that further investigations are required to prove the hypothesis. The rest of this chapter explores more insight into the pressure pulse mechanism of melt ejection.

5.3 Melt Ejection by the Effect of Acoustic Pulse

5.3.1 Acoustic Pulse Theory

When the material is subjected to tensile stress, if sufficiently high, a fragment is ejected from the free surface of the material in a process called spallation (Grigoryev *et al.*, 2018).

Spallation is most often considered in the solid phase, but it can exist in liquids, including metal melts. Liquid spallation can be thought of as a cavitation process with the growth of vapour nuclei in a metastable stretched liquid (Povarnitsyn *et al.*, 2007). Laser irradiation can create a shock wave causing this spallation (De Rességuier et al., 2007) at a short pulse duration of a few nanoseconds or less and high strain rate (De Rességuier *et al.*, 2011). The cavity of vapour is created in the liquid when it is subjected to extremely large tension. Once the generated tensile stress exceeds the melt material tensile strength, the melt material is spalled after a picosecond range delay time; resulting in a fracture in the melt pool and mechanically ejection of the spalled melt (Luo *et al.*, 2009).

For the DLM experiment illustrated in Figure 5-5, the surface vaporisation by the effect of ejection laser imparts a substantial recoil pressure on the melt pool surface that generates a compression pulse propagates inside the liquid material.

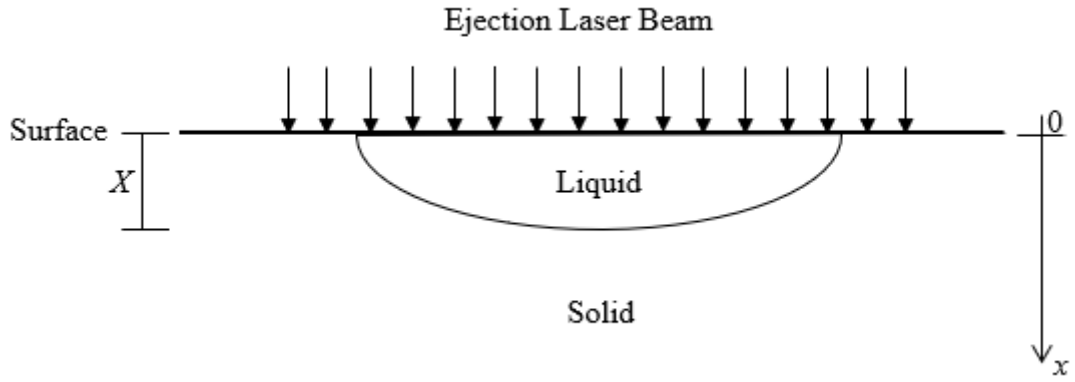

Figure 5-5 Schematic illustration of ejection laser interaction with the melt pool surface in the DLM method.

In this section, a one-dimensional acoustic pulse model is used to show how this transient compressive stress is converted to tensile stress, causing material spallation. This model simulates the acoustic pulse as a function of time and position. The melt spall takes place when the magnitude of the tensile stress exceeds the tensile strength of the material (Struleva et al., 2016) in a plane parallel to the liquid-solid interface (Moshe et al., 2000).

It is assumed that the pulse takes a Gaussian distribution as the temporal distribution of nanosecond pulse, taken from the specification of the used Nd: YAG laser, takes approximately Gaussian shape with FWHM pulse duration t_{eject} of 5 ns. Also, it is assumed that the material is isotropic and homogenous within the melt pool and the solid regions.

Let us first calculate the recoil pressure pulse generated at the melt pool surface by the effect of surface vaporisation by ejection laser. As the vaporisation temperature is reached, the recoil pressure acts on the vapour-liquid interface with maximum magnitude at the centre of melt pool given by the Clausius-Clapeyron's relation:

$$P_{\max} = P_{\text{amb}} exp\left[\frac{M\Delta H_{\text{v}}(T_{\text{v}})}{k_{\text{B}}}\left(\frac{1}{T_{\text{v}}} - \frac{1}{T_{\text{s}}}\right)\right] \tag{5-1}$$

which is valid up to the critical temperature. P_{amb} is the ambient pressure (101,325 Pa), M is the molar mass, $\Delta H_{\text{v}}(T_{\text{v}})$ is the vaporisation enthalpy at vaporisation temperature which is ($=L_{\text{v}}/N_{\text{A}}$) where L_{v} is the latent heat of vaporisation and N_{A} is Avogadro constant, T_{v} is the vaporisation temperature under the pressure P_{amb}, T_{s} is the material surface temperature and k_{B} is Boltzmann constant.

Molar mass M =55.7 gms/mole is calculated in Equation (5-2) using the average composition by weight of 316 stainless steel as given in Table 5-1.

Table 5-1 The chemical composition of 316 stainless steel (wt%) (Weiss and Stickler, 2007).

C	Cr	Ni	Mo	Mn	Si	Fe
0.066	17.4	12.3	2.05	1.57	0.21	balance

$$M = 1/\left(\frac{C\%}{M_{\text{C}}} + \frac{Cr\%}{M_{\text{Cr}}} + \frac{Ni\%}{M_{\text{Ni}}} + \frac{Mo\%}{M_{\text{Mo}}} + \frac{Mn\%}{M_{\text{Mn}}} + \frac{Si\%}{M_{\text{Si}}} + \frac{Fe\%}{M_{\text{Fe}}}\right) \tag{5-2}$$

The recoil pressure given in Equation (5-1) is surface temperature-dependent. The high irradiance 10.6 GW/cm^2 from the ejection laser can increase the surface temperature to or exceeding the material critical temperature (Chang and Warnor, 1996). In this case, the surface temperature is assumed to be the critical temperature of 9230 K (Chawla *et al.*, 1981) for 316 stainless steel. The saturation compression pressure on the surface was calculated in Equation (5-1) to be 4.77 GPa.

As mentioned before, this compression pulse is partly converted into tensile stress at a certain time and position inside the melt pool. The theoretical calculation of this tensile stress pulse will be used in Section 5.3.2. Now, let us identify the tensile strength of the material, which is a temperature and strain rate-dependent that increases with the strain rate increase while it decreases with the temperature increase. Due to the unavailable data for 316 stainless steel in

literature, the data of iron that is the main content of this alloy, is used. The tensile strength of iron melt was calculated theoretically by Mayer & Mayer (2015) for a wide range of temperature and strain rate and found in the range of 0.5 to 5 GPa. This result was supported by an experiment conducted by Struleva et al., (2016) for the strain rates (4–9)×10^8 s^{-1} and temperature about 3000 K giving 0.5–1.3 GPa tensile strength. Now, the magnitude of the recoil pressure at the melt pool surface and the maximum spall strength of the melt have been identified to be 4.77 and 1.3 GPa, respectively.

The Gaussian compressive pulse generated at the melt pool surface (x=0) is assumed to be given by,

$$P_1(0, t_a) = P_{max} \exp\left(-\frac{4\ln(2)\, {t_a}^2}{{t_{eject}}^2}\right) \tag{5-3}$$

where P_{max} is the maximum pressure given in Equation (5-1), t_a is the time from the pulse start and t_{eject} is the FWHM pulse time.

This Gaussian compressive pulse generated at the melt pool surface and propagating in the positive x-direction inside the liquid toward the liquid-solid interface (see Figure 5-5) as a function of time and distance is therefore,

$$P_1(x, t_a) = P_{max} \exp\left(-\frac{4\ln(2)\, (x - c_l t_a)^2}{{L_l}^2}\right) \tag{5-4}$$

where x is the distance from the melt pool surface, c_l is the speed of sound in liquid and L_l is the FWHM pulse length in the liquid region (L_l = FWHM = $c_l t_a$).

Let us now introduce the concept of acoustic impedance. The acoustic impedance Z is the resistance to sound propagating the medium that is the product of the medium density and the speed of sound of the medium (Z=ρc). Suppose an incident planar acoustic pulse travelling with specific impedance (Z_A=$\rho_A c_A$) in medium A encounters the interface between medium A and medium B. Part of the incident pulse is reflected back into medium A with a reflection coefficient given in Equation (5-5) and the rest is transmitted to medium B with specific impedance (Z_B=$\rho_B c_B$) with transmission coefficient (T_{pulse}=1-R_{pulse}). Figure 5-6 illustrates the reflection and transmission of the incident pulse at the interface.

$$R_{pulse} = \frac{Z_B - Z_A}{Z_B + Z_A} \tag{5-5}$$

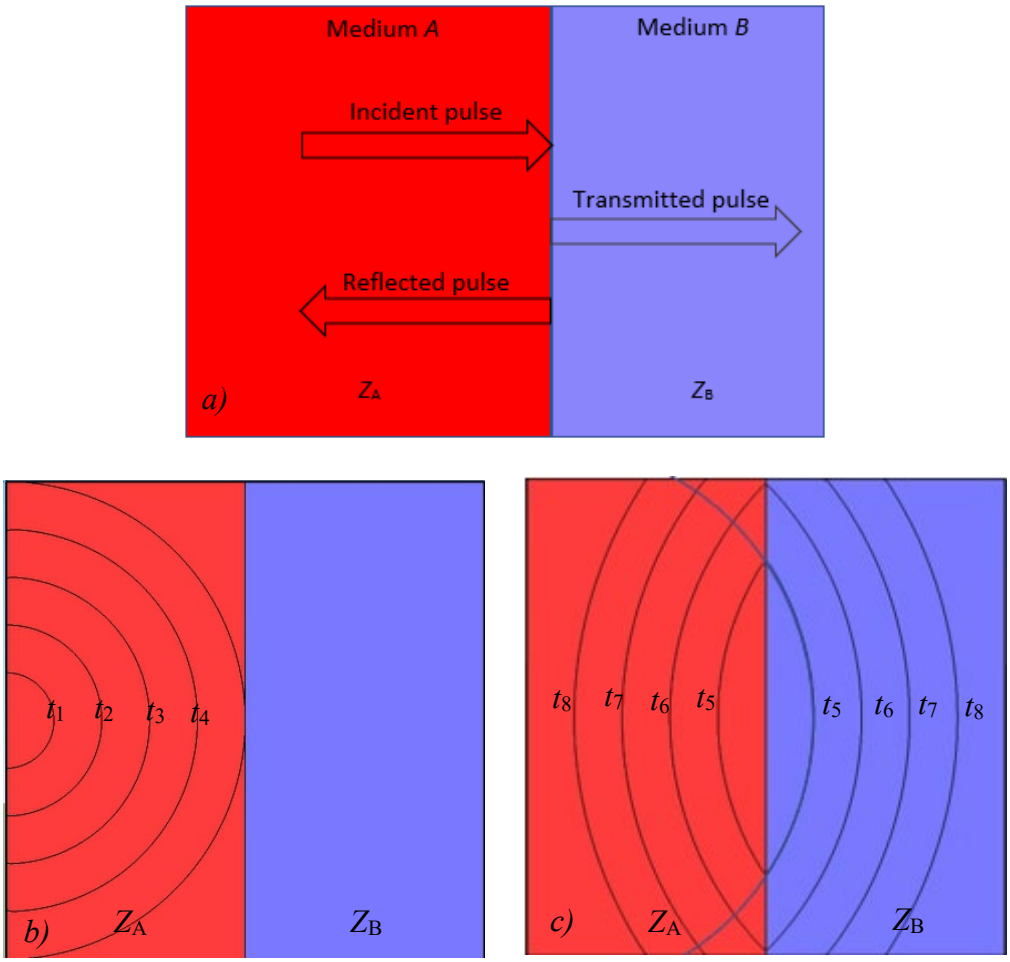

Figure 5-6 a) Reflection and transmission of an acoustic pulse at normal incidence to an interface between two mediums with different acoustic impedances, b) 2-D diagram of the for the pulse propagating in the medium at different time from the pulse start time (A), c) shows the reflected and transmitted parts of the pulse at the interface.

Returning to the acoustic model (simulation) in this study, P_1 crosses the melt pool in the positive x-direction until arrives at the liquid-solid interface. Because the compressive pulse P_1 mismatch from low (liquid) to high impedance (solid), P_1 is partly reflected and converted into a compressive pulse, P_2, given in Equation (5-6). The second part from P_1 is transmitted as compressive pulse, P_{T1}, that propagates in the solid given in Equation (5-7). P_{T1} is attenuated when travels in the thick solid part. P_2 propagates in the negative x-direction and once arrives at the free boundary (melt pool surface) it is fully reflected and is converted into a tensile stress pulse, P_3, given in Equation (5-8) as the air impedance is very low compared to the impedance of liquid metal. This tensile stress pulse, P_3, propagates in the positive x-direction and when arrives at the liquid-solid interface, it is partly reflected as tensile pulse, P_4, given in Equation (5-9). P_4 propagates in the negative x-direction. The second part of P_3

is transmitted as tensile pulse, P_{T2}, given in Equation (5-10) propagates in the solid region. P_{T2} is attenuated as travels in the thick solid part.

The fractional factors in the Equations (5-6) to (5-10) are the reflection coefficient R_{pulse}, calculated in Equation (5-5), represents the ratio between the reflected pulse at medium *B* and the incident pulse from medium *A* at normal incidence.

$$P_2(x, t_a) = 0.24P_{max}\exp\left(-\frac{4\ln(2)\,(x + c_l t_a)^2}{{L_l}^2}\right) \tag{5-6}$$

$$P_{T1}(x, t_a) = 0.76P_{max}\exp\left(-\frac{4\ln(2)\,(x - c_s t_a)^2}{{L_s}^2}\right) \tag{5-7}$$

$$P_3(x, t_a) = -0.24P_{max}\exp\left(-\frac{4\ln(2)\,(x - c_l t_a)^2}{{L_l}^2}\right) \tag{5-8}$$

$$P_4(x, t_a) = -0.058P_{max}\exp\left(-\frac{4\ln(2)\,(x + c_l t_a)^2}{{L_l}^2}\right) \tag{5-9}$$

$$P_{T2}(x, t_a) = -0.183P_{max}\exp\left(-\frac{4\ln(2)\,(x - c_s t_a)^2}{{L_s}^2}\right) \tag{5-10}$$

where L_s is the FWHM pulse length in the solid region (L_s = FWHM = $c_s t_a$) and c_s is the speed of sound in solid.

The net pulse, *P*, inside the liquid is given in Equation (5-11) which is the superposition of compressive and tensile stress pulses components at $0 > x > X$, where *X* is the maximum melt depth shown in Figure 5-5.

$$P(x, t_a) = P_1(x, t_a) + P_2(x, t_a) + P_3(x, t_a) + P_4(x, t_a) \tag{5-11}$$

It is assumed that the material properties in the molten phase and the solid phase are temperature independent, although the density and speed of sound are significantly temperature-dependent, for simplicity the mean densities and speed of sound were taken for 316 stainless steel in the liquid to be 6530 kg/m^3 and 3441 m/s at 2350 K, respectively, and in the solid region to be 7624 kg/m^3 and 4818 m/s at 1000 K, respectively, as listed in Table 5-2.

Table 5-2 Density and speed of sound in liquid and solid phases for 316 stainless steel.

Property	Unit abbreviation	Symbol	Value
Density (Leibowitz et al., 1976)	kg/m^3	ρ_s ρ_l	7624 (at 1000 K) 6530 (at 2350 K)
Speed of sound (Chawla et al., 1981)	m/s	c_s c_l	4818 (at 1000 K) 3441 (at 2350 K)

In the following section, simulation of these compressive and tensile pulses will be shown at different times and the positions within the material and compared with the experimental results of DLM method.

5.3.2 Simulation and Experimental Results

From the previous chapter, it was noticed that the residual molten material in the DLM method that was not ejected increases as melt depth increases. The results of different melt depths of 14, 20, 28 μm were chosen from the DLM results as an example to study the acoustic pulse.

The results based on a one-dimensional simulation of the spallation process show the evolution of the pressure profile at time and position in the *x*-direction along the polar laser beam axis induced by a Gaussian laser pulse of $t_{\text{eject}} = 5$ ns. First, the result of 20 μm melt depth is presented as an example in Figure 5-7 to show the full detail for the evolution of the pressure profile in a sequence of figures at a different time from the start of ejection laser until melt spallation occurs. The figures show the regions of air, melt pool (liquid) and the solid in addition to the liquid-air and liquid-solid interfaces in solid brown colour. The distance between these interfaces equals the melt depths, *X*. Arrows are presented as an indication of the travel direction of the acoustic pulses. The tensile strength necessary for spallation of the material is also presented. The spallation zone is presented in the last figure in the simulation when the spallation occurs. The time presented in the graphs represents the time from the start of ejection nanosecond laser pulse.

Figure 5-7 depicts the original pressure distribution, P_1, (long dashed black line) when the ejection nanosecond laser starts with a maximum amplitude of 4.77 GPa. The original pulse is illustrated as if it exists in the air, but in reality, it is generated at the air-liquid interface. Note, part of the Gaussian beam exists inside the liquid material at t=0 because the profile is

mathematically simulated by a Gaussian function taking the actual laser FWHM pulse duration of 5 ns.

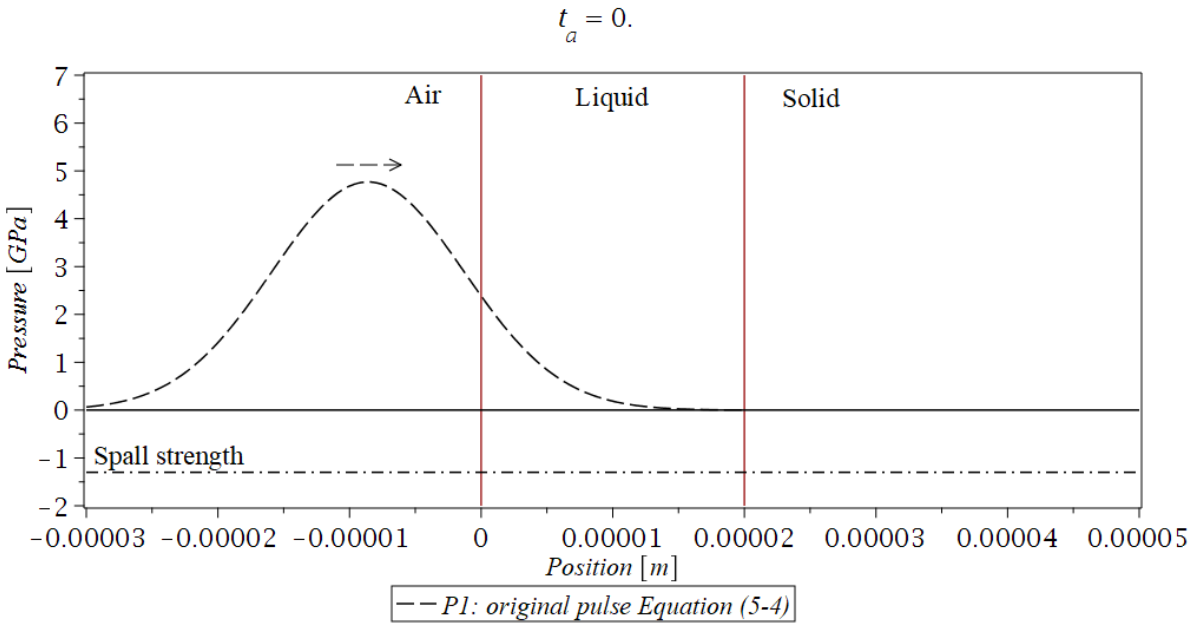

Figure 5-7 The profile of original compressive pressure pulse at staring time of ejection laser.

After the start of the ejection laser, the compressive pulse, P_1, propagates inside the liquid in the positive x-direction as shown in Figure 5-8. The net compressive pulse inside the liquid, P, in blue colour takes only the value of the original compressive pulse, P_1.

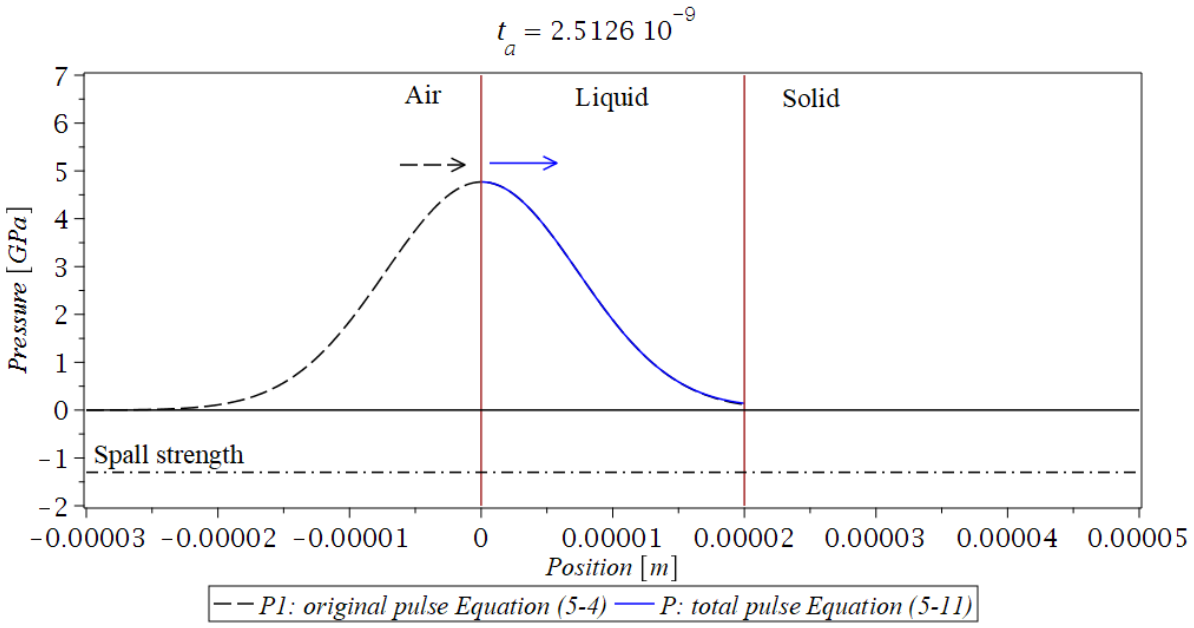

Figure 5-8 Propagating of the original pulse inside the liquid region.

Figure 5-9 shows when the original compressive pulse, P_1, arrives at the liquid-solid interface, it is divided into two parts: the reflected compressive pulse, P_2, in red colour that propagates inside the liquid in the negative x-direction and the transmitted compressive pulse into the solid region, P_{T1}, (grey colour) that propagates in the positive x-direction and later is attenuated. The net compressive pulse, P, propagating in the positive x-direction inside the liquid (blue colour) is the superposition of compressive stress pulses components P_1 and P_2. This time is the end of FWHM laser pulse time, 5 ns.

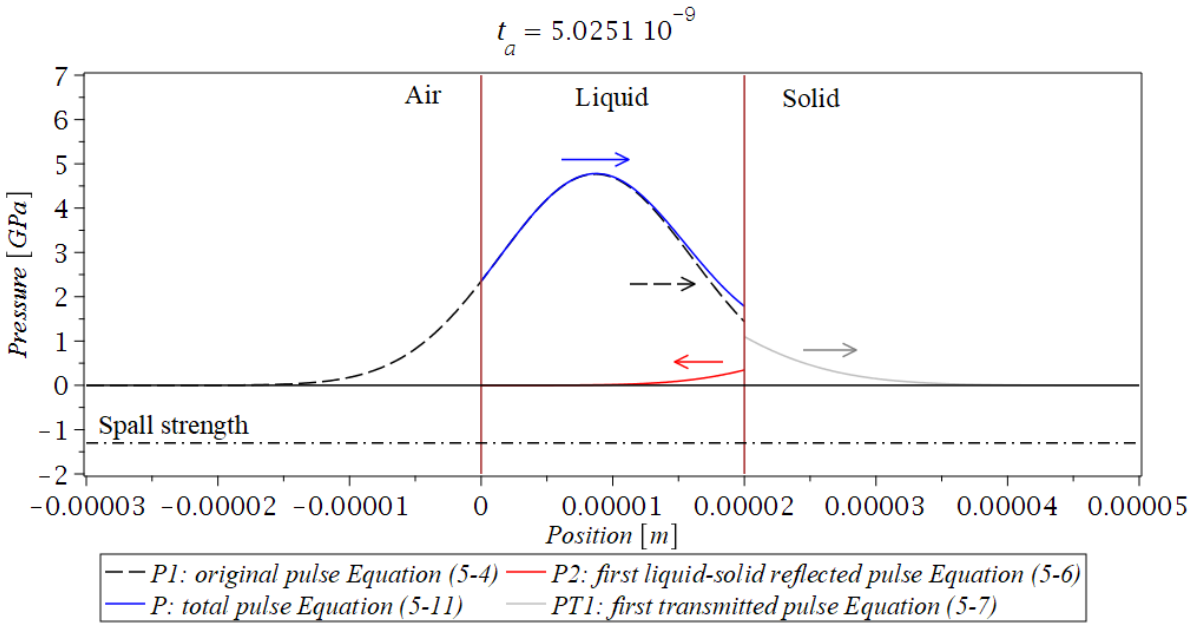

Figure 5-9 The evolution of the pressure profiles at the end of laser pulse time (FWHM), t = 5 ns.

Then the net compressive pulse, P, reaches its maximum amplitude (approximately 5.91 GPa) at the liquid-solid interface at t = 8 ns as shown in Figure 5-10 that is the sum of maximum amplitude of the original pulse P_1 (4.77 GPa) and the maximum amplitude of the reflected compressive pulse P_2 (1.14 GPa) i.e 0.24×4.77 GPa. This occurs when the middle of the pulses P_1 and P_2 are on the liquid-solid interface.

After that, the net compressive pulse drops down near the liquid-solid interface since most of the original pulse, P_1, is transmitted to the solid and the reflected compressive pulse, P_2, is moving toward the liquid-air interface in the negative direction as shown in Figure 5-11. The compressive pulse, P_2, propagates in the negative x-direction and once arriving at the liquid-air interface it is totally reflected (due liquid-air reflection coefficient is approximately unity) generating a tensile stress pulse, P_3, (green) that propagates in the positive x-direction. The

incoming positive pulse, P_2, is cancelled by the reflected negative pulse, P_3, causing a local standing pulse of zero pascals in the vicinity of the free surface.

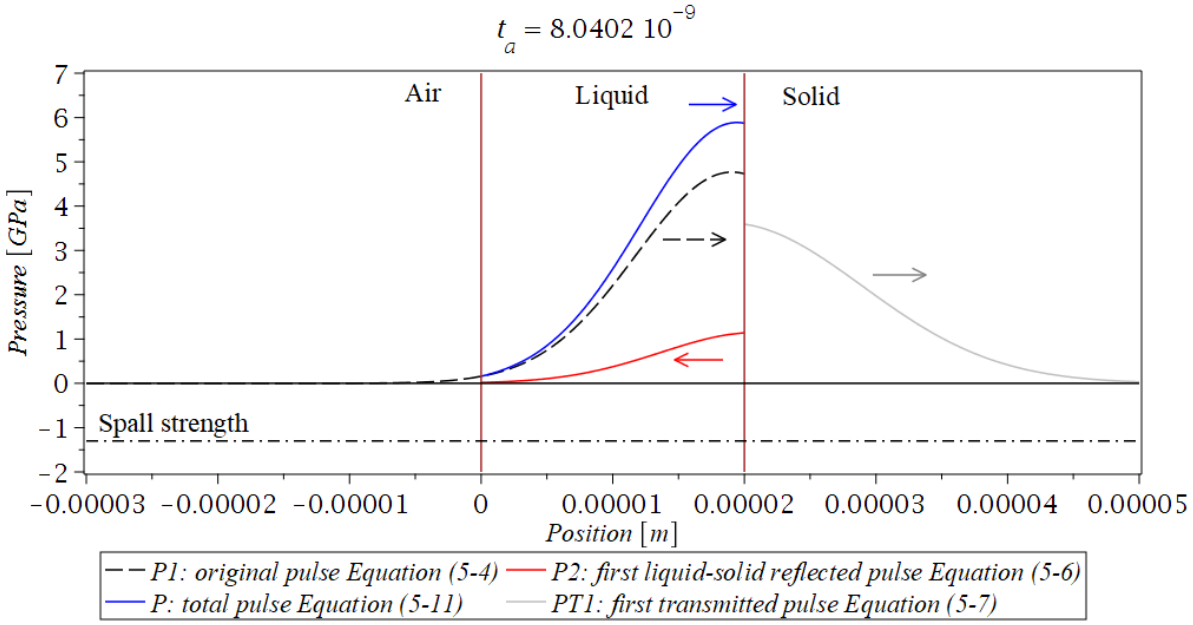

Figure 5-10 The evolution of the pressure profiles when the net compressive pulse, P, reaches its maximum amplitude at the liquid-solid interface.

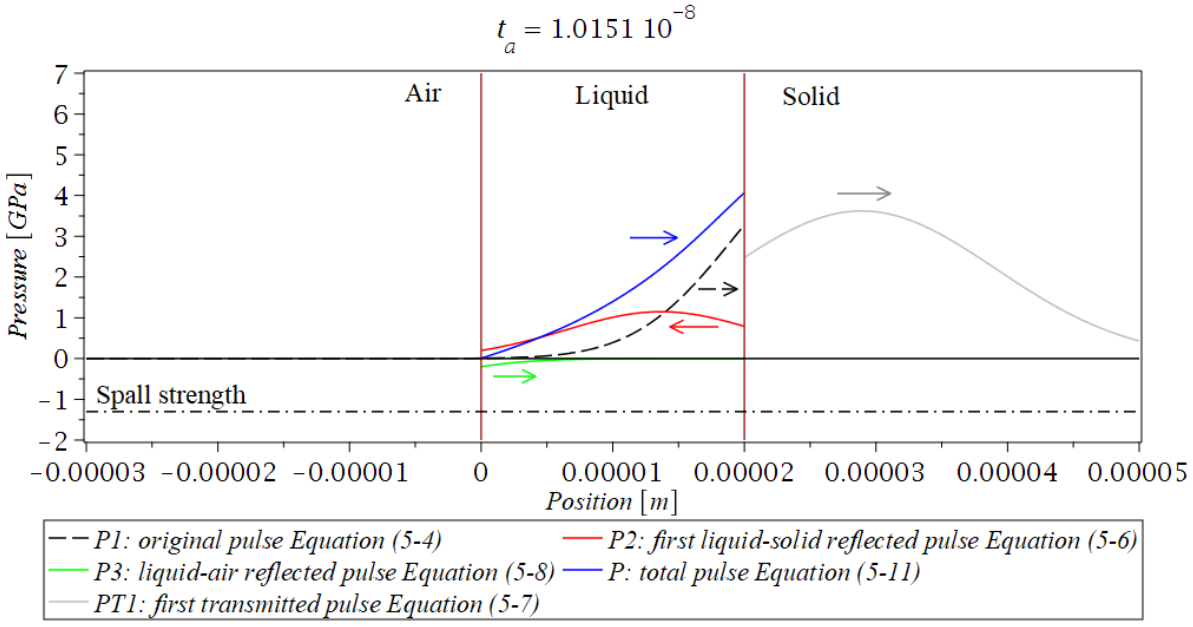

Figure 5-11 Profiles evolutions at 10 ns.

At t_a = 14 ns, as can be seen in Figure 5-12, the compressive P_2 and tensile P_3 pulses cancel each other resulting in a complete destructive interference. The figure shows that the transmitted pulse, P_{T1}, is fully existing in the solid region. P_1 does not exist at this time since it is totally converted to a transmitted and reflected pulses.

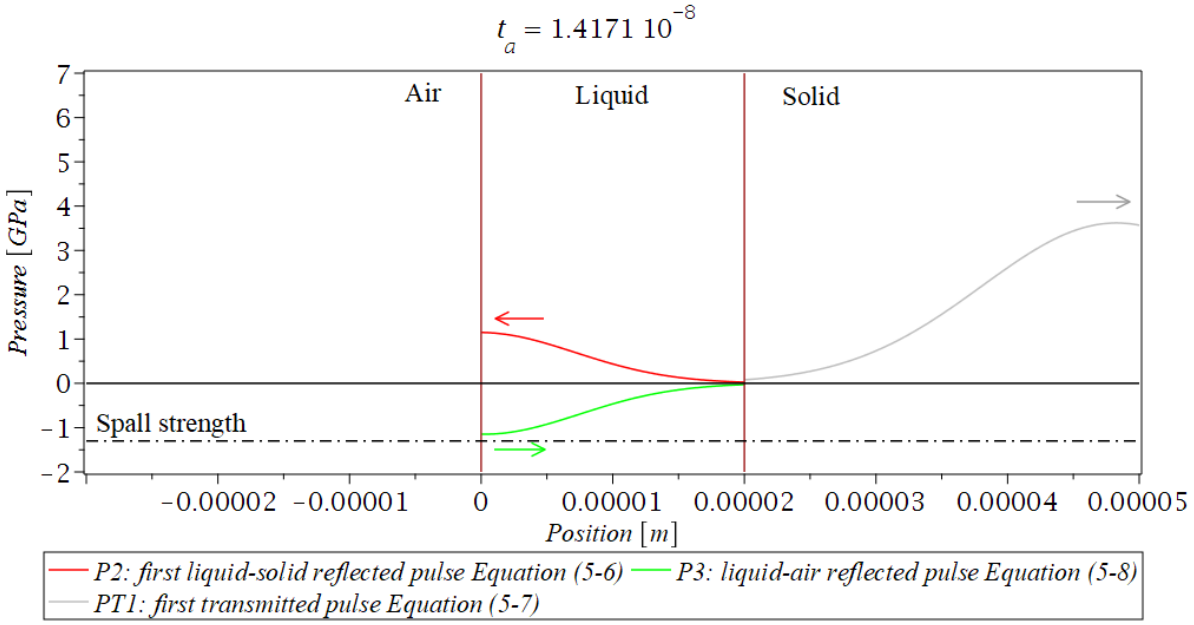

Figure 5-12 Standing pulse in the liquid region.

The net pulse, P, starts appears as tensile stress as shown in Figure 5-13 as a result of travelling of P_2 and P_3 in negative and positive directions, respectively. It can be seen that P amplitude is less than material spall strength (1.3 GPa).

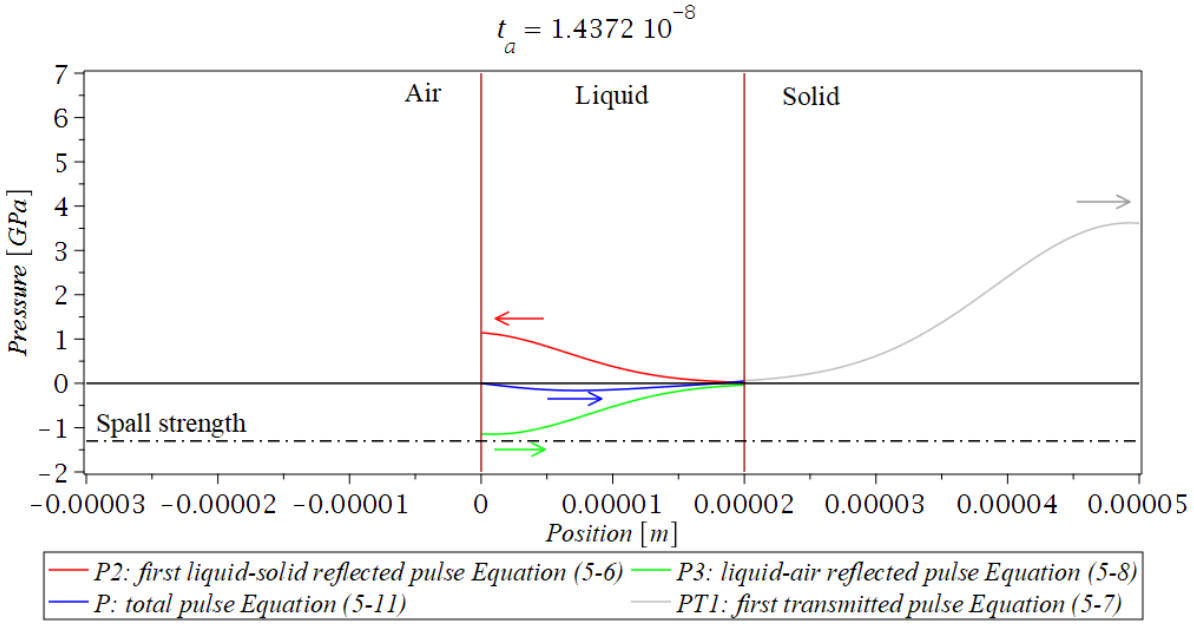

Figure 5-13 Profiles evolutions when the net pulse, P, starts appears as tensile stress.

Figure 5-14 shows the tensile pulse, P_3, moves in the positive x-direction causing an increase in the amplitude of the net tensile pulse, P. Once P_3 arrives at the liquid-solid interface it is divided into two pulses: a transmitted tensile pulse, P_{T2}, (cyan colour) into the solid region; a

reflected tensile pulse, P_4, moving in the negative x-direction that is tiny and does not appear in the figure. P is still not reaching the spall strength target.

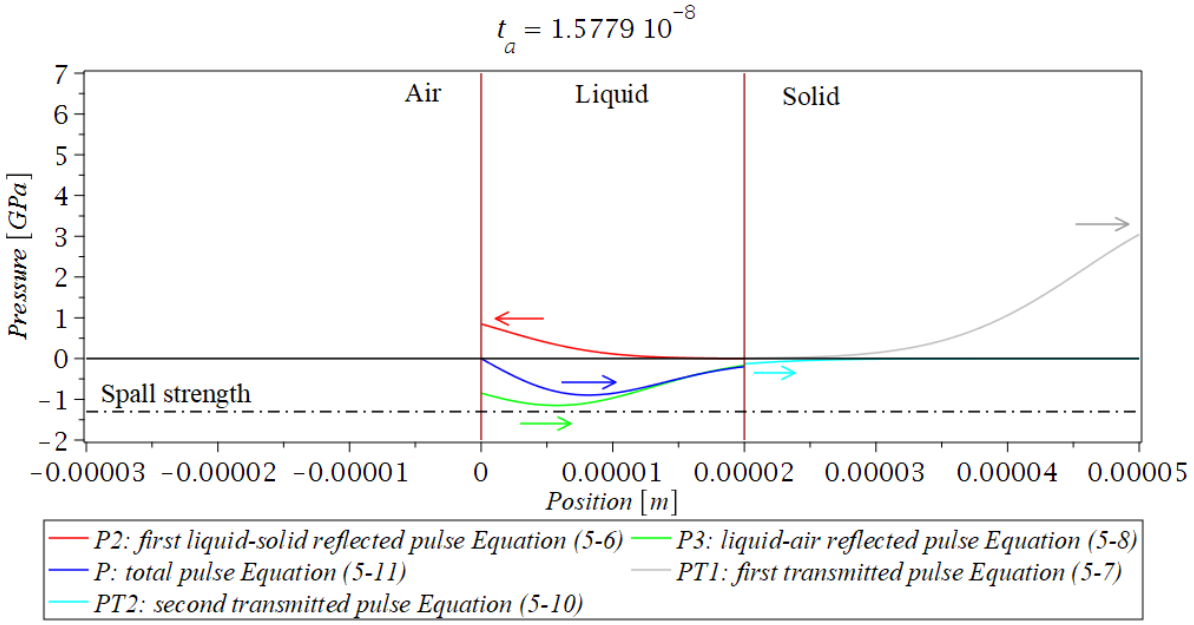

Figure 5-14 Increase in the net tensile pulse amplitude.

A few nanoseconds later, the increase in the amplitude of P_4 (purple) near the liquid-solid interface increases the net tensile pulse, P, until reaching approximately 1.3 GPa in the vicinity of the liquid-solid interface as can be seen in Figure 5-15.

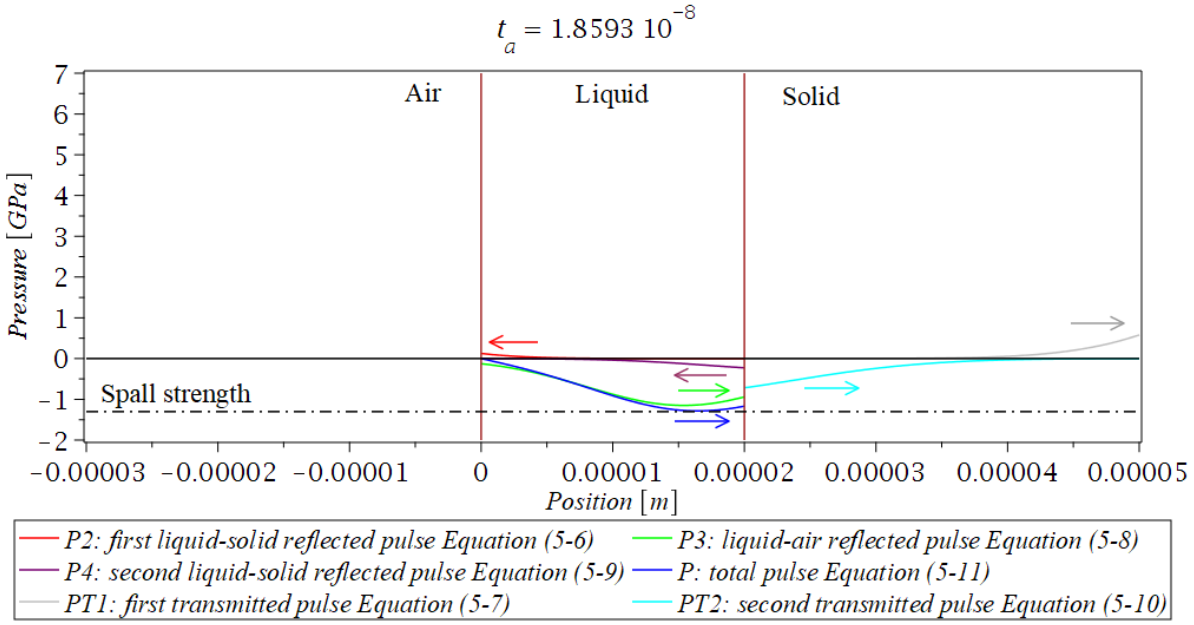

Figure 5-15 The evolution of the profiles when the net tensile stress reaches the target spall strength.

Figure 5-16 shows only the net tensile stress pulse, P, at the same time of Figure 5-15. The net pulse profile approaching near the liquid-solid interface causes material stretching due to its tensile stress, P. The spallation condition is satisfied near the liquid-solid interface as a result of the superposition of two tensile pulses moving toward each other: P_3 and P_4. As a result, the cavity is formed, which is marked as the dotted zone.

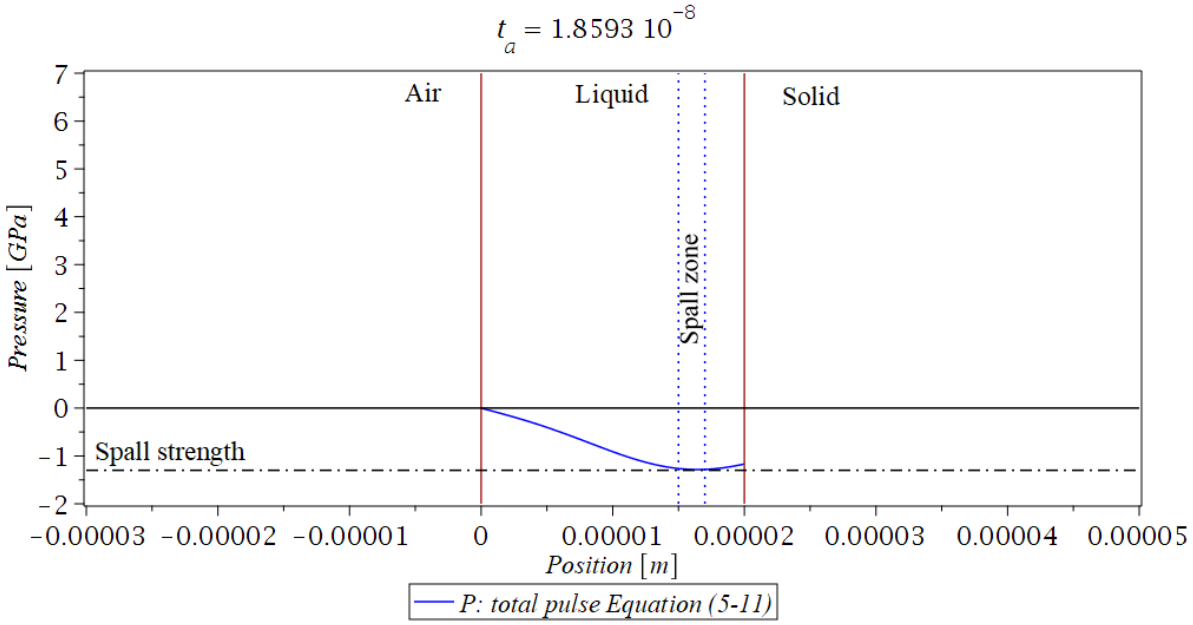

Figure 5-16 The formation of the spallation zone at 17 µm distance from the liquid free surface for20 µm melt depth.

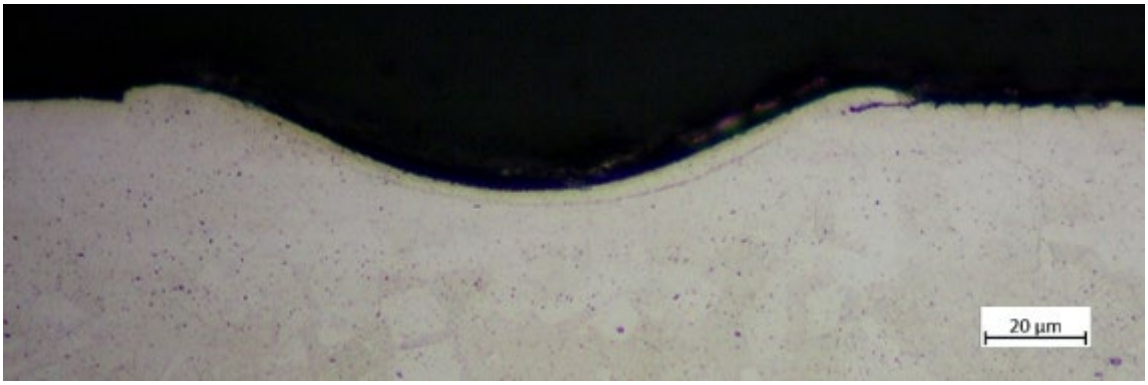

Figure 5-17 Micrograph cross-section of DLM method: maximum melt depth of 20 µm and hole with a maximum depth of 17 µm.

From the above theoretical calculation of the maximum tensile stress, it was found that the tensile stress can exceed the tensile strength of the material. This result is compared with the results of DLM method experiment for the same melt depth. The cross-section of the hole for 20 µm melt depth in Figure 5-17 confirms the theoretical analysis of the position of the maximum tensile stress. In which, the spallation occurs approximately at the same distance

17 µm and ejects the molten material leaving behind approximately 3 µm residual molten material inside the hole.

The same simulation analysis is conducted for the 14 and 28 µm melt depth from DLM method and is presented in Figure 5-18 and Figure 5-20, respectively, at the final stage when the spallation takes place.

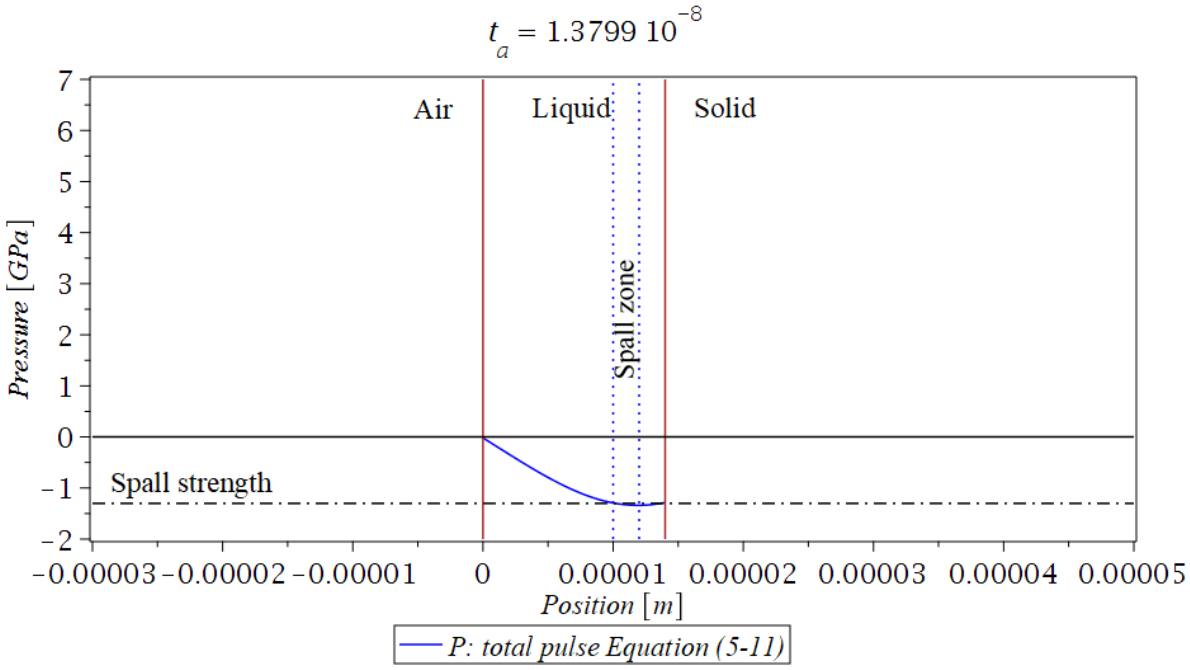

Figure 5-18 The formation of the spallation zone at 12 µm distance from the liquid free surface for14 µm melt depth

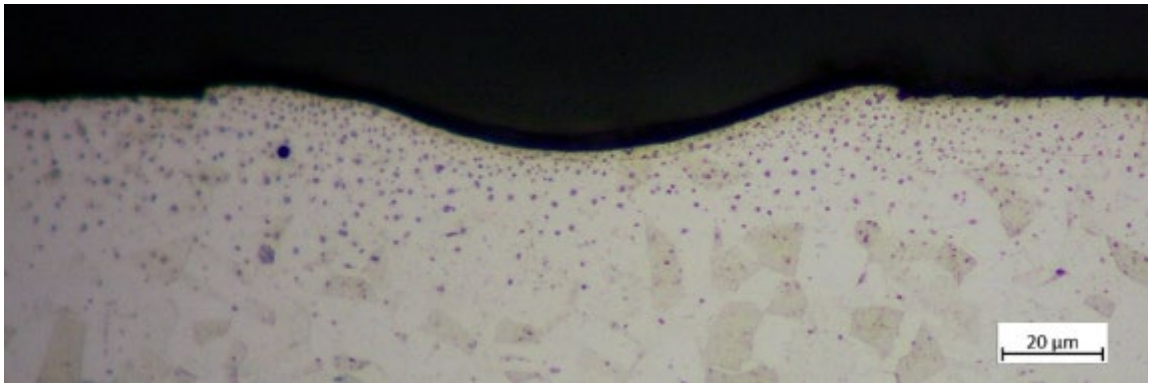

Figure 5-19 Micrograph cross-section of DLM method: maximum melt depth of 14 µm and hole with a maximum depth of 12 µm.

The simulation result of 14 µm liquid depth is compared with the DLM result for the same melt depth. The cross-section shows an agreement with the simulation of the position of the

maximum tensile stress. The spallation occurs approximately at the same distance 12 µm and ejected the molten material leaving behind approximately 2 µm residual molten material inside the hole.

The simulation result of 28 µm liquid depth is compared with the DLM result for the same melt depth. The cross-section shows an agreement with the simulation of the position of the maximum tensile stress. The spallation occurs approximately at the same distance 24 µm and ejected the molten material leaving behind approximately 4 µm residual molten material inside the hole.

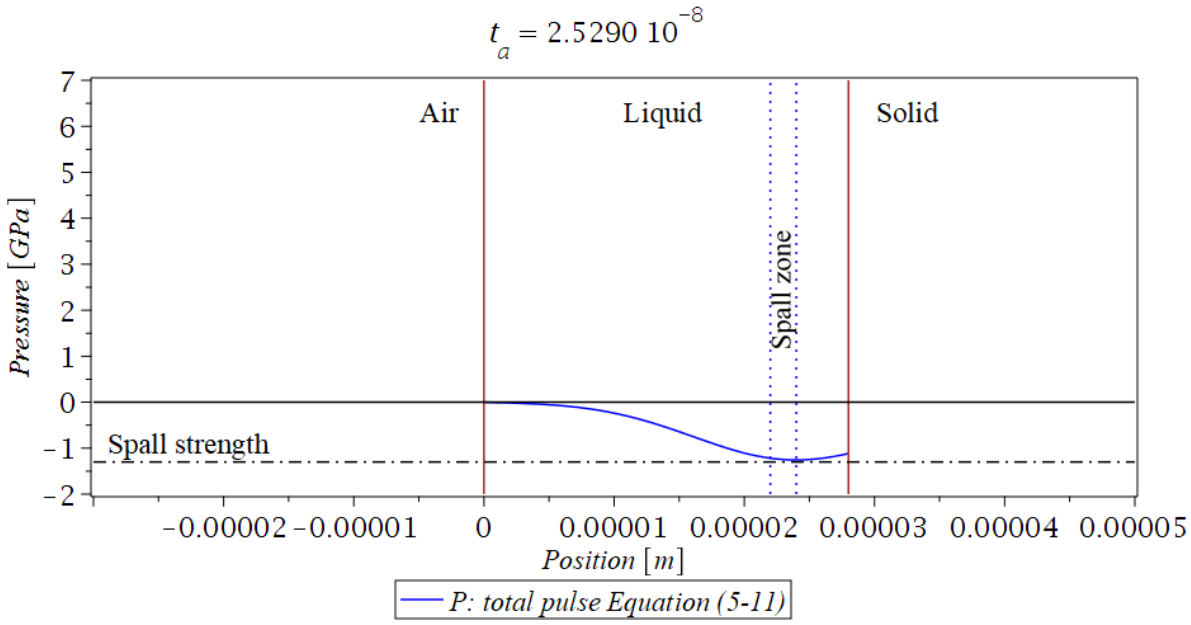

Figure 5-20 The formation of the spallation zone at 24 µm distance from the liquid free surface for 28 µm melt depth.

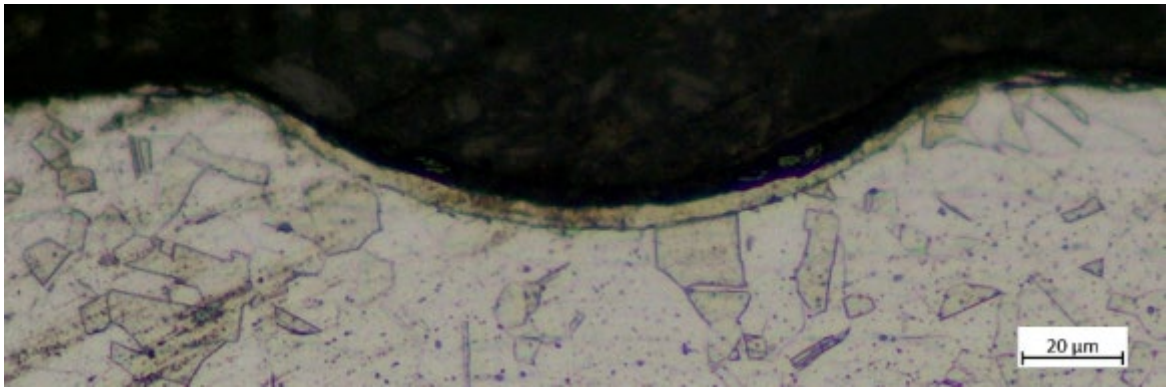

Figure 5-21 Micrograph cross-section of DLM method: maximum melt depth of 28 µm and hole with a maximum depth of 24 µm

For the melt depth of 14, 20, and 28 µm, the maximum tensile stress arises at a distance of 12, 17, 24 µm near the liquid-solid interface, respectively. The spallation occurs at

approximately 14, 19 and 25 ns from the start ejection laser for the melt depth of 14, 20, and 28 μm melt depths respectively. Table 5-3 summarise the simulation and experimental results for different melt depths.

Table 5-3 Experimental and simulation results of the spallation depths

Melt depth (μm)	14	20	28
Experimental hole depth (μm)	12	17	24
Experimental residual melt thickness (μm)	2	3	4
Simulation hole depth (μm)	12	17	24

5.3.3 Effect of Transmitted Compressive Pulse, P_{T1}, on the Spallation Process

The transmitted compressive pulse, P_{T1}, propagates inside the solid region. This pulse attenuates inside the solid region, and the final part is totally reflected as tensile stress from the free rear surface (solid-air interface). This reflected tensile pulse propagates again in the negative *x*-direction toward the solid-liquid interface and partly reflected as compressive stress. It is hypothesised that the melt spallation is not formed by the effect of this tensile pulse because the tensile stress created inside the liquid detailed in the previous section occurs before P_{T1} reaches the solid-liquid interface. The effect of the transmitted pulse, P_{T1}, on the spallation process was tested by conducting the DLM experiment at 20 μm melt depth on 3 mm thickness 316 stainless steel sample. Two samples were used: the first sample is shown in (Figure 5-22-a) which was used in the previous chapter. The second sample was machined from its back surface as shown in (Figure 5-22-b). The sample illustrated in (Figure 5-22-b) was machined in this shape to reflect and attenuate the transmitted pulse on the side AB. The experiment was conducted under the same conditions except for the sample shapes. To validate the hypothesis, the DLM experiments in both samples were imaged using the high-speed camera in the same setup described in Section 5.2.1.

Videos showed in both samples shapes the melt was ejected without significant difference. Figure 5-23 shows the Sequence of frames for the ejection process for the experiment (b) while the result of the experiment (a) is presented in Figure 5-4. Thus, the hypothesis is accepted that the melt is not spalled by the effect of tensile stress generated from the transmitted pulse, P_{T1}.

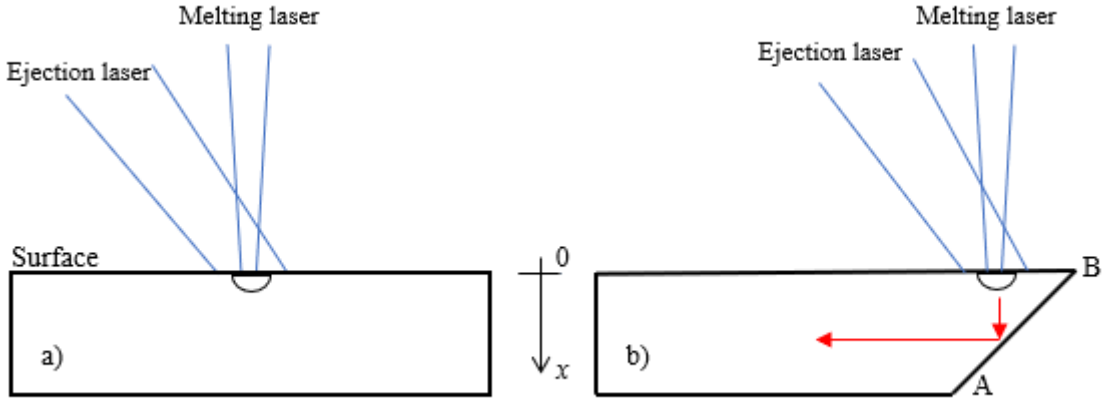

Figure 5-22 Samples shapes in the experiment of testing the transmitted compressive pulse inside solid. Red arrows indicate the direction of pressure pulse that attenuates in the solid region.

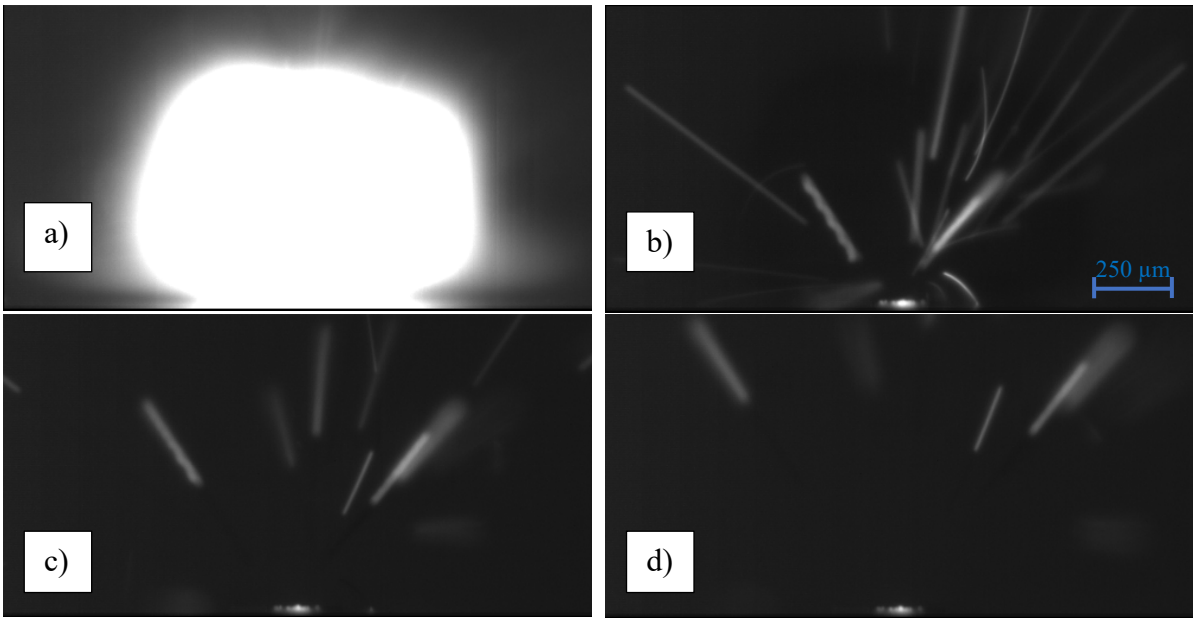

Figure 5-23 Sequence of frames for the ejection process for the experiment b in Figure 5-22 taken by a high-speed camera with a frame separation of 100 µs and 1×2 mm frame dimensions.

5.3.4 Effect of Pressure Pulse Created at the Free Solid Back Surface on Spallation.

In Section 5.3.2, the results show that the molten material is ejected once the ejection laser is triggered on the melt pool surface. In this section, the hypothesis of the melt ejection by the effect of the tensile pulse is validated by introducing the nanosecond ejection laser on the back surface of the sample as illustrated in Figure 5-24.

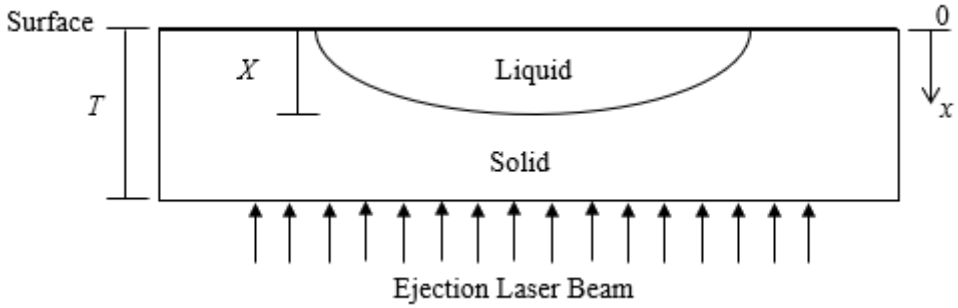

Figure 5-24 Schematic illustration of ejection laser interaction at the back surface of the sample.

5.3.4.1 Experimental setup

The same two lasers used in the DLM method was used in this experiment on the same synchronisation setup described in the previous chapter at the stationary mode. A CW fibre laser to create a molten pool and a Q-switched Nd:YAG laser (ejection laser). Nevertheless, the focus position of the two laser beams is different in this experiment. As illustrated in Figure 5-25 the melting laser is on the top surface of the sample while the ejection laser was focused on the back surface of the sample. Both lasers were delivered with an incidence angle of 90˚ to the workpiece surface. In this experiment, the workpiece is mounted on a stationary stage. This stage is designed to allow both lasers to reach the workpiece. Therefore, the experiment was conducted in an air atmosphere. The melting process was conducted at a power of 26.4 W, the irradiance of 49 kW/cm^2 and 9 ms melting time to create the melt pool. The ejection laser pulse was shoot at the end of melting time even was introduced at the back surface. This is because the time for the pulse to cross the sample to the top surface is in nanosecond range that is negligible compared with the melting time of 9 ms. To reduce the attenuation effect, this experiment was conducted on a thin stainless steel workpiece of thickness T = 50 µm.

In this experiment, the effect of the combination of both lasers in the DLM method was investigated as a means to test the hypothesis of liquid phase spallation by the effect of pressure pulse generated at the back solid surface of the workpiece. The geometry and metallurgical features of the hole created by DLM were analysed using an optical microscope. All images were taken from the centre cross-section. Workpieces were prepared for microstructural analysis by cold mounting in epoxy, mechanically grinding using series of

papers of 320, 600, 1200 and 4000 grit SiC grades, polishing using 9, 3 and 0.050 µm diamond suspension and etching using Kalling's No. 2 for approximately 5 s.

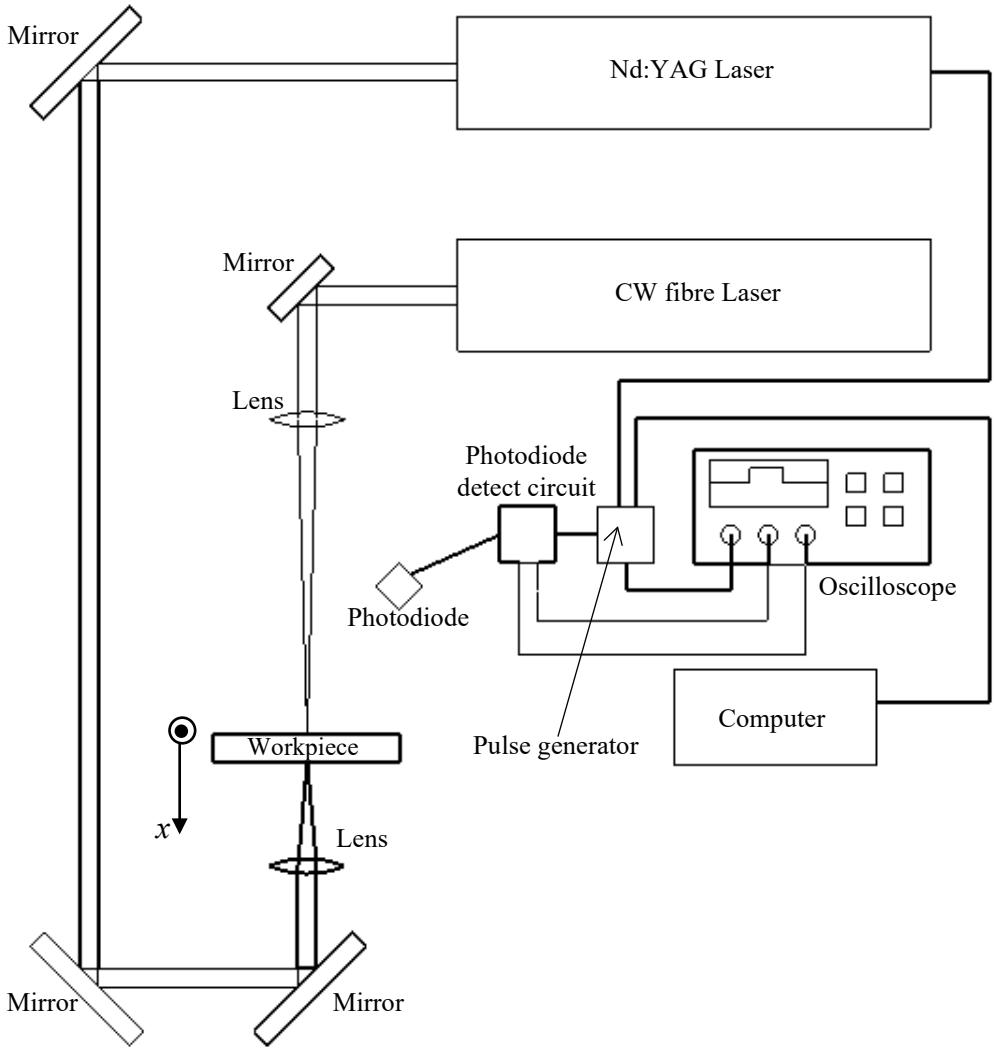

Figure 5-25 Schematic of the DLM setup to test the pressure pulse on the back of the workpiece.

5.3.4.2 Theory

In this experiment, surface vaporisation by the effect of ejection laser imparts substantial recoil pressure on the back surface of the sample that generates a compression pulse propagates inside the solid material.

The transient stress that causes material spallation is studied in this section using the one-dimensional pulse model of the evolution of the pulses generated inside the material. This model simulates the acoustic pulse as a function of time and position. The same assumption for the front surface ejection described in Section 5.3.1 is taken for the Gaussian distribution

of the pulses generated inside the material and the assumption of the material that is isotropic and homogenous within the solid and the liquid regions. The same pressure maximum magnitude of the original pulse, P_{max}, 4.77 GPa calculated in Equation (5-1) in Section 5.3.1 was taken in the current experiment despite a slight difference in the material properties. Moreover, the ejection laser is introduced on a solid material not as in the DLM method in the previous chapter where the ejection laser was introduced on pre-laser melting high surface temperature. The magnitude of the original pulse is reduced by the effect of attenuation, however, this effect is ignored in the simulation.

The same value of tensile strength 1.3 GPa tensile strength for iron used in Section 5.3.1 was used in this analysis.

The Gaussian compressive pulse generated at the back surface (x=T) is given by,

$$P_{\mathrm{A}}(T, t_{\mathrm{a}}) = P_{\max}\exp\left(-\frac{4\ln(2)\,{t_{\mathrm{a}}}^2}{{t_{\mathrm{eject}}}^2}\right) \tag{5-12}$$

This Gaussian compressive pulse generated at the back surface propagates in the negative x-direction inside the solid toward the solid-liquid interface as a function of time and distance (see Figure 5-24) is given by,

$$P_{\mathrm{A}}(x, t_{\mathrm{a}}) = P_{\max}\exp\left(-\frac{4\ln(2)\,(x + c_{\mathrm{s}}t_{\mathrm{a}})^2}{{L_{\mathrm{s}}}^2}\right) \tag{5-13}$$

After P_A crosses the solid region in the negative x-direction, this compressive pulse arrives at the solid-liquid interface. Because the compressive pulse, P_A, mismatches from high (solid) to low impedance (liquid), P_A is partly reflected and is converted into a tensile pulse P_B given in Equation (5-14). P_B is attenuated as travels and bounces back and forth along the solid region. The second part from P_A is transmitted as compressive pulse, P_C, that propagates in the liquid as given in Equation (5-15). P_C propagates in the negative x-direction and once arrives at the free boundary (melt pool surface), it is fully reflected and is converted into a tensile stress pulse, P_D, given in Equation (5-16). This tensile stress pulse, P_D, propagates in the positive x-direction and when arrives at the liquid-solid interface, it is partly reflected as a tensile pulse, P_E, given in Equation (5-17). P_E propagates in the negative x-direction. The

second part of P_D is transmitted as tensile pulse, P_F, given in Equation (5-18) propagates in the solid in the positive x-direction and is attenuated when propagates in the solid region.

$$P_B(x, t_a) = -0.24P_{max}\exp\left(-\frac{4\ln(2)\,(x - c_s t_a)^2}{{L_s}^2}\right) \quad (5\text{-}14)$$

$$P_C(x, t_a) = 0.76P_{max}\exp\left(-\frac{4\ln(2)\,(x + c_l t_a)^2}{{L_l}^2}\right) \quad (5\text{-}15)$$

$$P_D(x, t_a) = -0.76P_{max}\exp\left(-\frac{4\ln(2)\,(x - c_l t_a)^2}{{L_l}^2}\right) \quad (5\text{-}16)$$

$$P_E(x, t_a) = -0.18P_{max}\exp\left(-\frac{4\ln(2)\,(x + c_l t_a)^2}{{L_l}^2}\right) \quad (5\text{-}17)$$

$$P_F(x, t_a) = -0.58P_{max}\exp\left(-\frac{4\ln(2)\,(x - c_s t_a)^2}{{L_s}^2}\right) \quad (5\text{-}18)$$

The net pulse, P_{net}, is given in Equation (5-19) which is the superposition of compressive and tensile stress pulses components at $0 > x > X$, where X is the maximum melt depth depicted in Figure 5-24.

$$P_{net}(x, t_a) = P_C(x, t_a) + P_D(x, t_a) + P_E(x, t_a) \quad (5\text{-}19)$$

The fractional factors in the equations (5-14) to (5-18) are the reflection coefficient R_{pulse}, calculated in Equation (5-5), represents the ratio between the reflected pulse at medium B and the incident pulse from medium A at normal incidence. To calculate the impedances for this stainless steel material the same values of the material density and the speed of sound for 316 stainless steel were taken.

In the following section, simulation of these compressive and tensile pulses will be presented at the time and the position within the material of DLM experiment of created 30 μm melt depth at the front surface by the melting laser.

5.3.4.3 Simulation Result

The detailed analysis of the spallation process is based on one-dimensional simulation results. The results show the evolution of the pressure profile at time and position in the *x*-direction along the polar laser beam axis induced by Gaussian laser pulse of τ = 5 ns of 30 µm melt depth. This analysis shows the full details for the evolution of the pressure profile in a sequence of figures at a different time from the start of ejection laser until spallation occurs.

Figure 5-26 shows the original pressure distribution P_A (long dashed black line). Once the ejection nanosecond laser starts with a maximum amplitude of 4.77 GPa. The original pulse is illustrated to show its shape in the air region that in reality does not exist. The profile shows part of the Gaussian beam is already exist inside the solid region even the laser has not started. This is due to the fact that the profile is presented based on mathematical simulation of a Gaussian function taking the actual laser FWHM pulse duration of 5 ns.

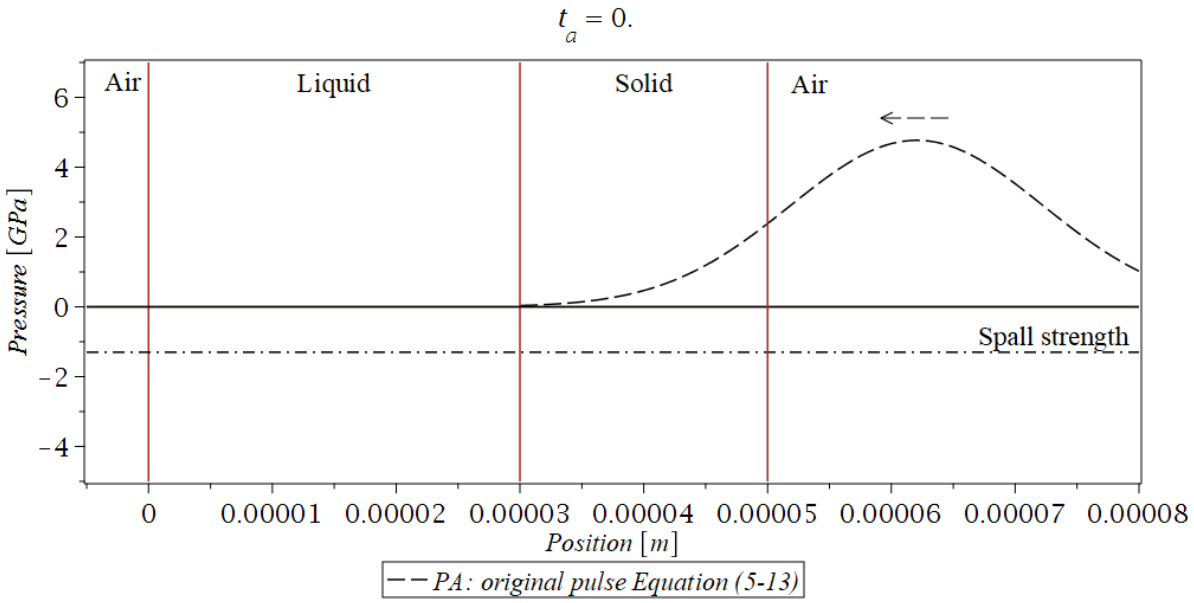

Figure 5-26 The original compressive pressure profile created at the back surface at staring ejection laser.

After the start of the laser pulse the compressive pulse, P_A, propagates inside the solid in the negative *x*-direction. The compressive pulse, P_A, arrives at the solid-liquid interface, it is divided into two parts: the reflected tensile pulse, P_B, in grey colour propagates inside the solid in the positive *x*-direction then is attenuated; the transmitted compressive pulse into the liquid region, P_C, propagates in the negative *x*-direction.

Once P_C arrives at the liquid-air interface it is totally reflected generating a tensile stress pulse, P_D, (green) that propagates in the positive *x*-direction Figure 5-27. The incoming

positive pulse, P_C, is cancelled by the reflected negative pulse, P_D, causing a local standing pulse of zero pascals in the vicinity of the free surface.

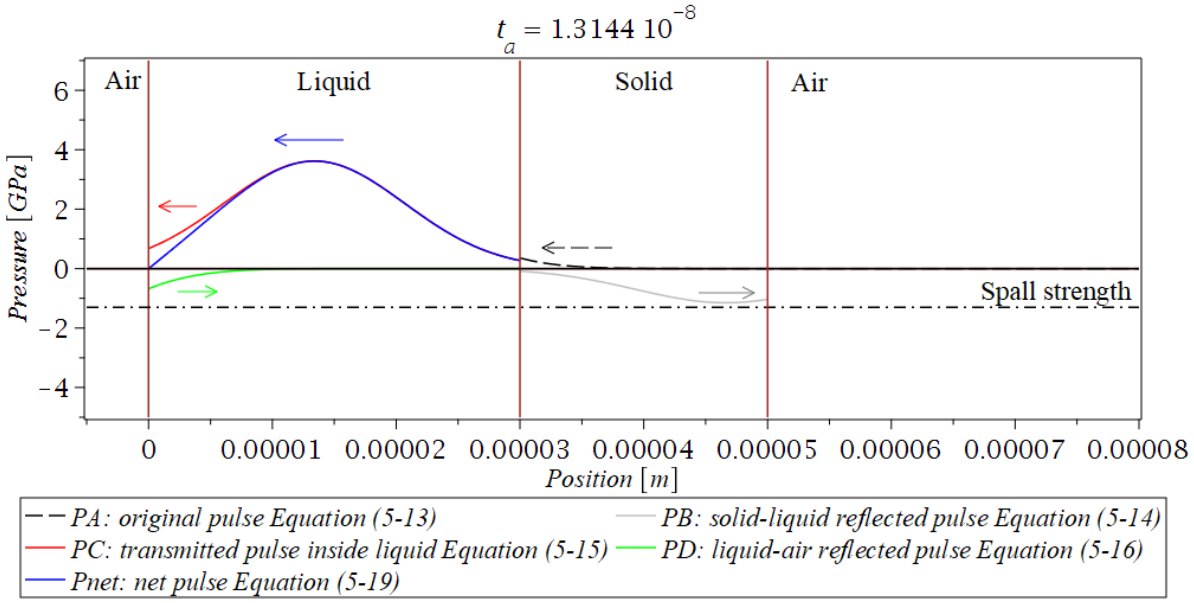

Figure 5-27 The reflection of the transmitted pulse at the liquid-air interface.

A t_a = 17 ns, as can be seen in Figure 5-28, the compressive P_C and tensile P_D pulses totally cancel each other resulting in a complete destructive interference causing a standing pulse of zero pascals.

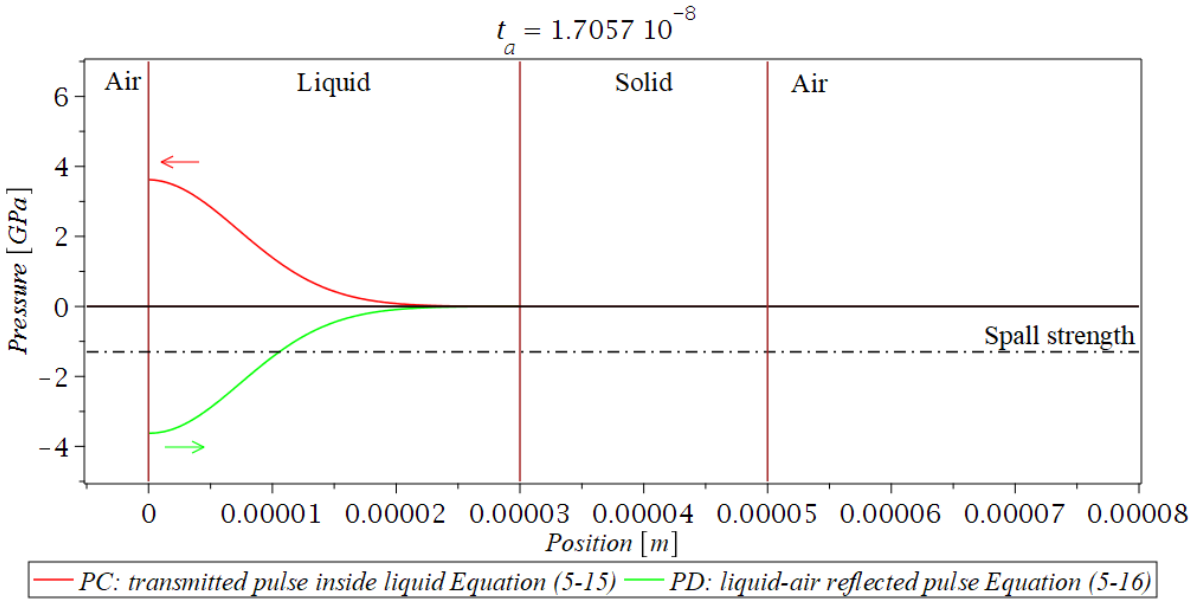

Figure 5-28 Standing pulse in the liquid region.

After that, the net pulse P_{net} starts appears as tensile stress as shown in Figure 5-29 but its amplitude is less than material spall strength (1.3 GPa).

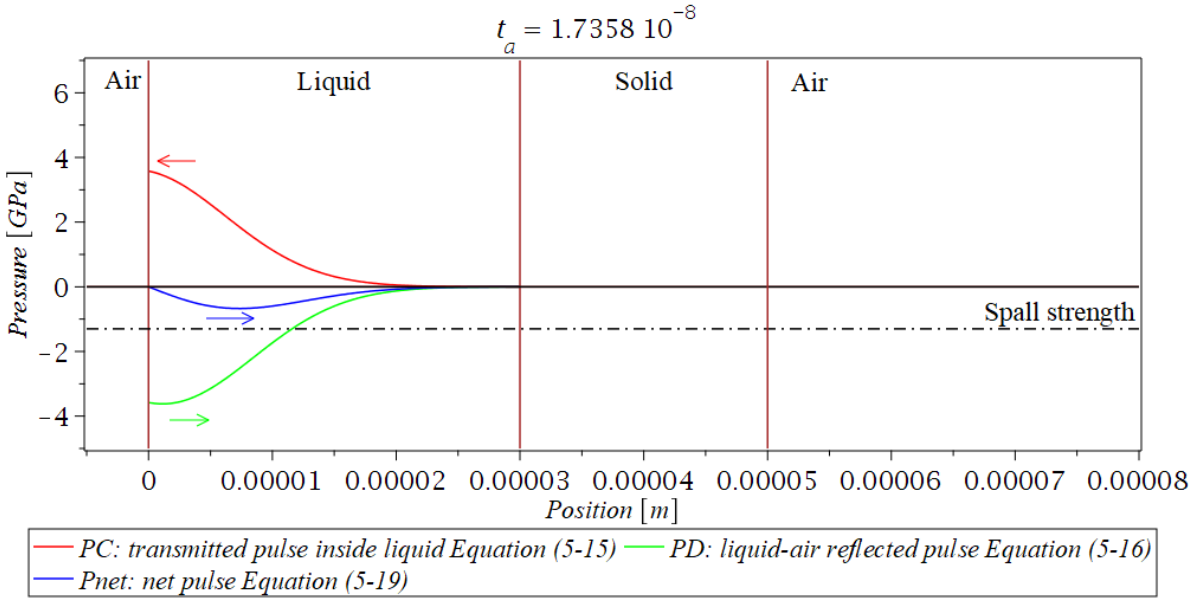

Figure 5-29 Profiles evolutions when the net pulse, P_{net}, starts appears as tensile stress.

Figure 5-30 shows the net tensile pulse, P_{net}, that is moving in the positive x-direction increases until reaching the target tensile strength. However, the experimental results will show later the spall does not occur at this position as this can be justified by the assumption that the magnitude of the pulse is not affected by attenuation which reduces the pulse magnitude.

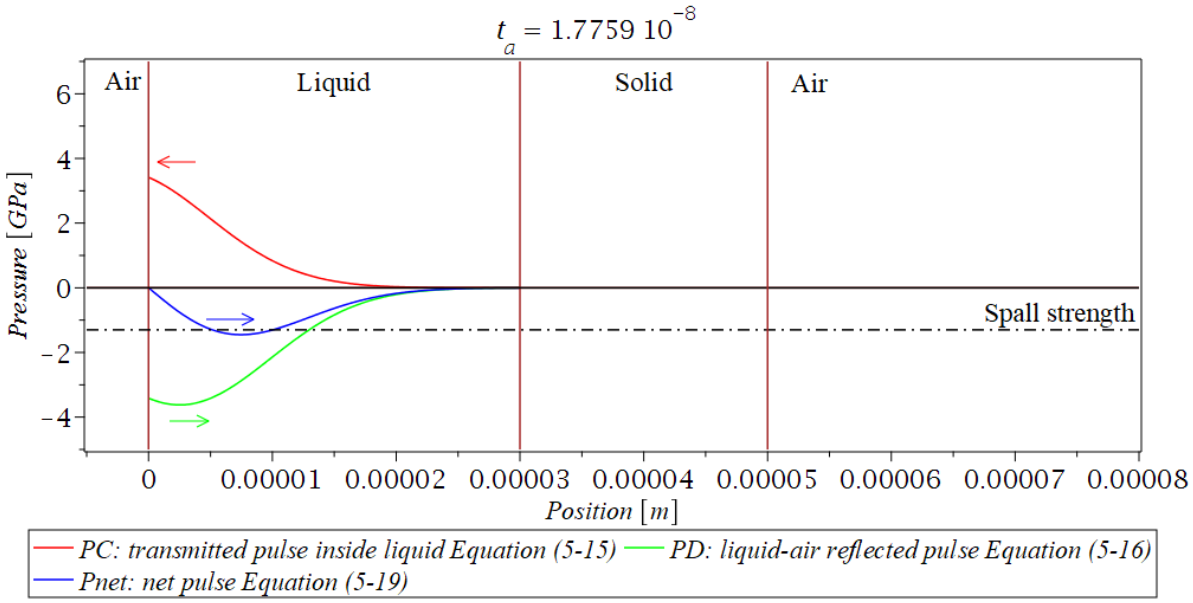

Figure 5-30 Increase in the net tensile pulse, P_{net}, amplitude.

Figure 5-31 displays the tensile pulse, P_{D}, moving in the positive x-direction causing an increase in the amplitude of the net tensile pulse, P_{net}, and once P_{D} arrives at the liquid-solid

interface it is divided into two pulses: a transmitted tensile pulse, P_F, (cyan colour) into the solid region and a reflected tensile pulse, P_E, moving in the negative x-direction that increases the amplitude of the net tensile pulse, P_{net}.

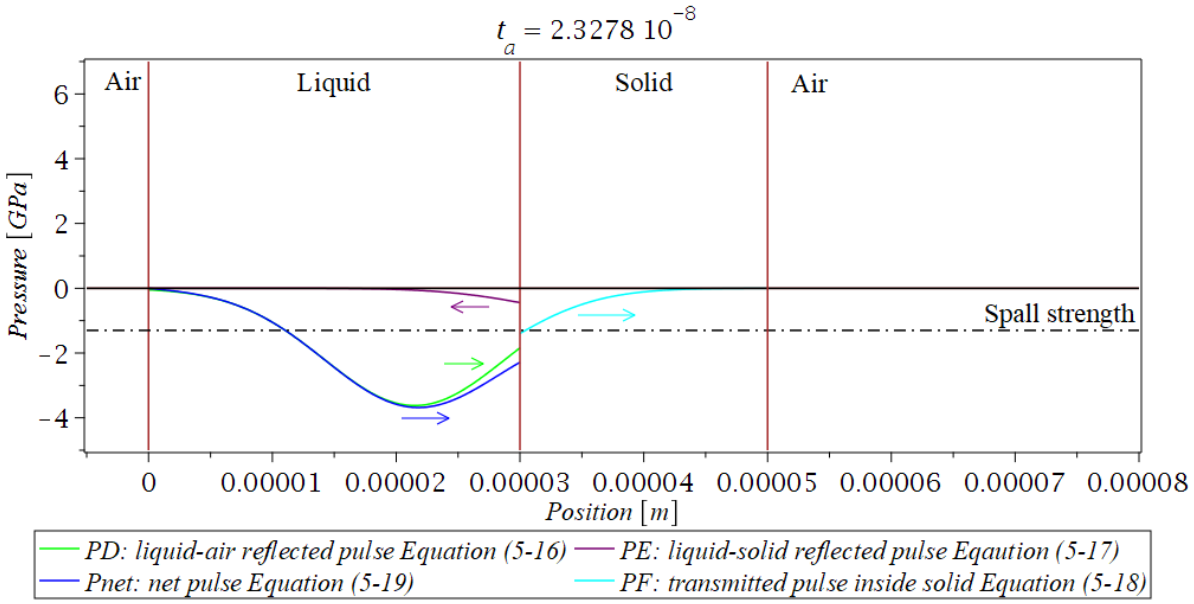

Figure 5-31 Reflection at the liquid-solid interface of P_D resulting in an increase in the amplitude of the net tensile pulse, P_{net}, near the solid-liquid interface.

Figure 5-32 shows the net pulse is increased until reaches at a position where the melt is spalled as the experimental results will show in the following section.

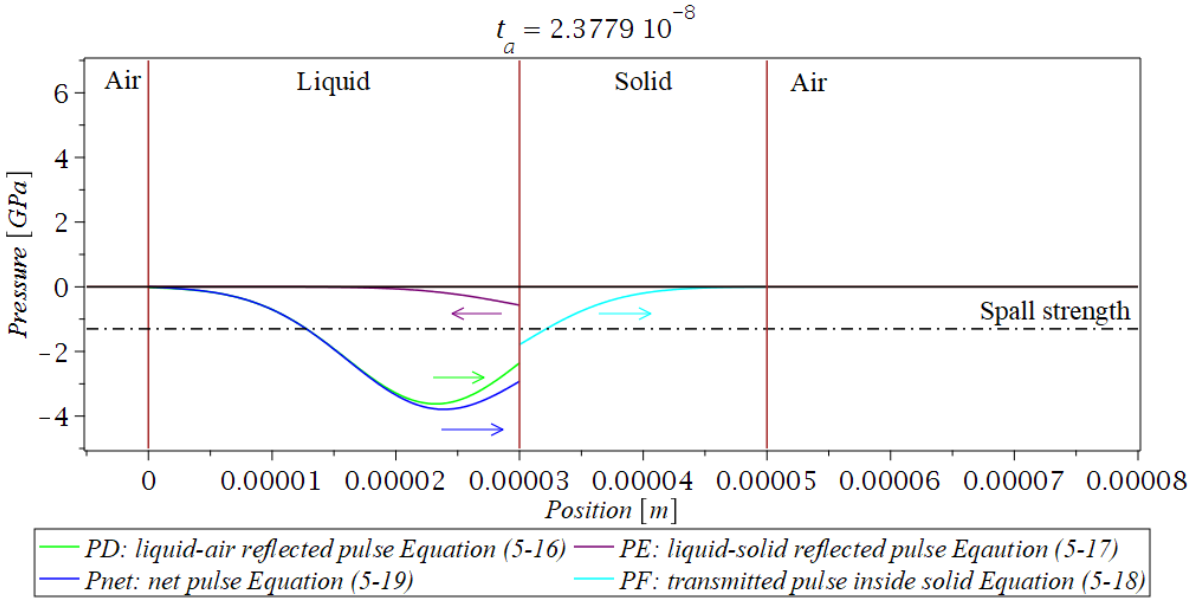

Figure 5-32 Evolution of profile at the position and time of the melt spall.

Figure 5-33 shows only the net tensile stress pulse P at the same time as Figure 5-32. The spallation condition is satisfied near the liquid-solid interface as a result of the superposition of two tensile pulses moving toward each other: P_D and P_E. As a result, the cavity is formed, which is marked as the dotted zone.

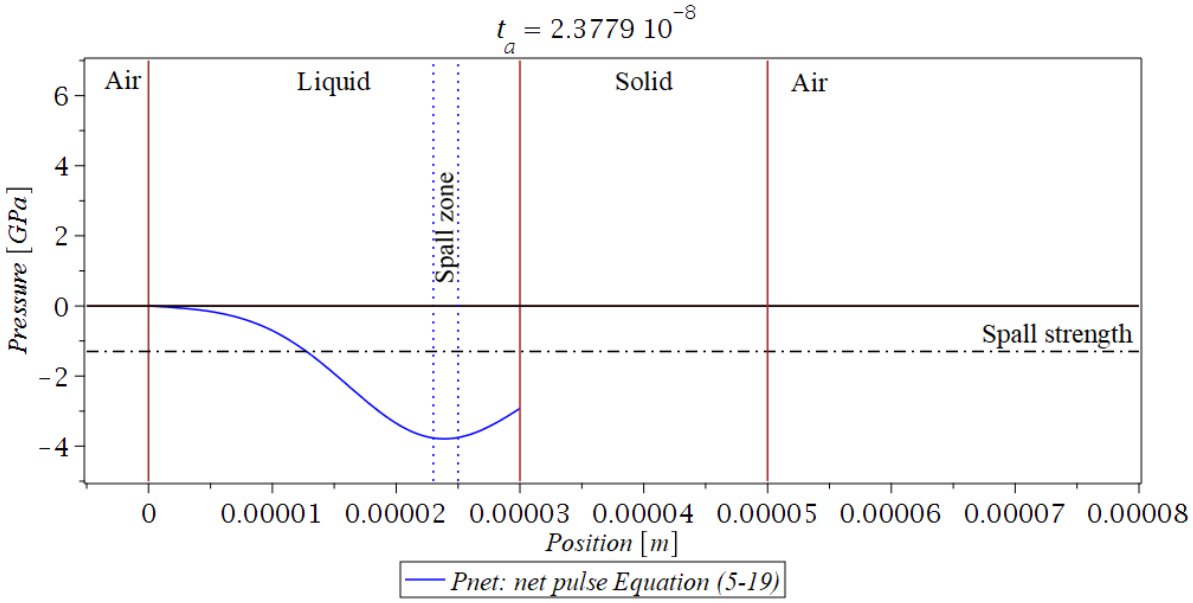

Figure 5-33 The formation of the spallation zone at 25 µm distance from the liquid free surface for30 µm melt depth.

5.3.4.4 Experimental Results

In this section, the results from the theoretical simulation are compared with the experimental results. The 3D surface profile of the DLM hole was generated using the Alicona Infinite-Focus, which were used to measure the depth of the hole. Figure 5-34 presents 3D images of the hole created with maximum depth of 25 µm at 9 ms melting time by ejecting molten material from 30 µm melt pool depth. The 3D image shows that the molten material was ejected by the effect of tensile stress produced from the compressive pulse generated at the back surface of the material using the 5 ns ejection pulse, without any redeposited material at the workpiece surface.

Cross-sectional images of the DLM hole, created by the effect of pressure generated by the ejection laser at the back surface of the material, is shown in Figure 5-35. This figure provides additional evidence of clean material ejection to the 3D surface profiles. However, not all the molten material was ejected and residual molten material along the bottom of the hole with a thickness of 5 µm from 30 µm melt pool depth. The effect of the ejection laser on the back solid surface can be seen in Figure 5-35 that the nanosecond pulse removed some

material. This may be compared with the effect of only the ejection laser, without pre-laser melting, observed on 316 stainless steel material in Section 4.3.3.2.

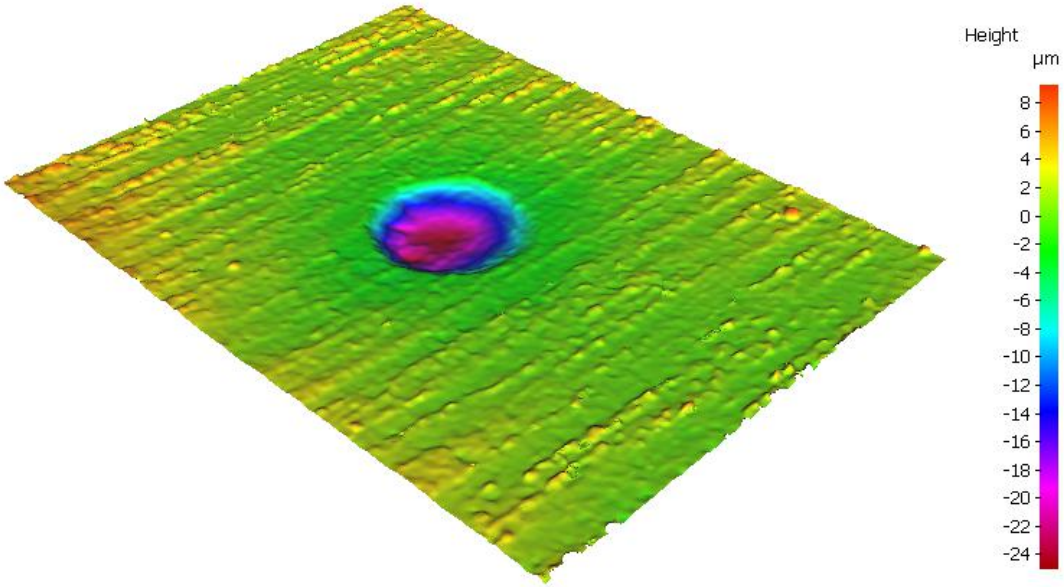

Figure 5-34 3D surface profile of the hole created in DLM method for the pressure at the back surface experiment

This experimental result illustrates that the molten material is spalled by the effect of a pressure pulse even this pressure was not imparted directly on the melt pool surface and introduced at the back solid surface. This provides strong evidence that supports the hypothesis that a tensile pulse is responsible for material ejection in the DLM method.

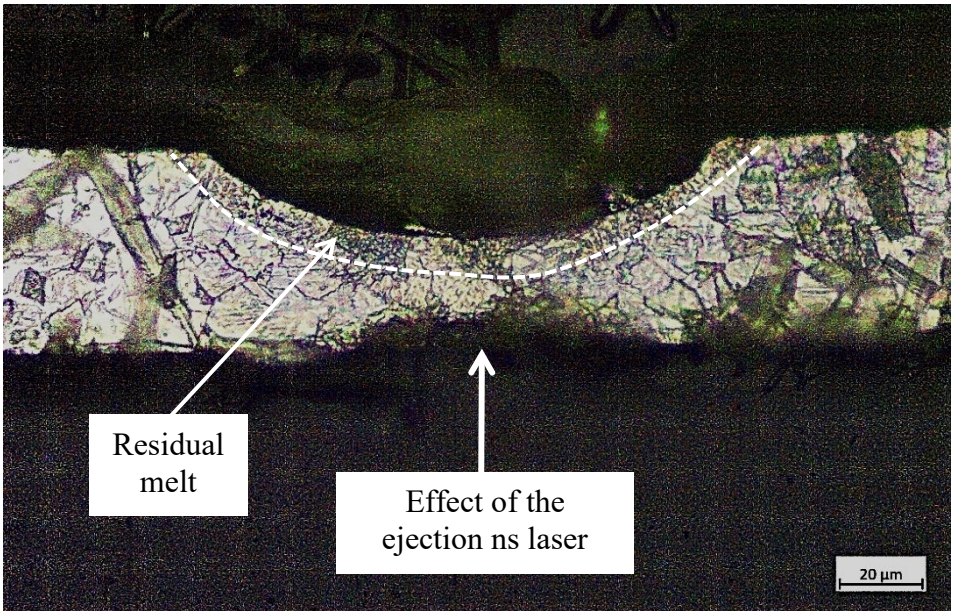

Figure 5-35 Micrograph cross-section of the hole created by the DLM method by the effect of back pressure introduced at the back surface of the material with a maximum hole depth of 25µm.

5.3.5 Summary and Conclusion

Theoretical models have been made by researchers to study the melt ejection mechanism in DLM method. However, their models contradict each other, and the experimental work done for the DLM method in literature and the conducted experiment in the previous chapter. In this work, it has been proposed to study the effect of the pressure pulse generated by the ejection laser on the melt ejection. A high-speed camera was used to show the behaviour of the ejected melt material. The spallation of a laser-melted material by nanosecond laser pulse was studied experimentally and theoretically. The propagation of the laser-generated pressure pulse inside the material was presented in detail. This pulse is converted at a certain time and position into tensile stress inside the melt material. It has been found in the pulse simulation that the spallation of the melt metal is triggered by increasing tensile stress produced in tensile pulses moving toward each other in the vicinity of the liquid-solid interface. When the amplitude of tensile pulse increases until exceeding the material strength, a cavity of vapour is generated inside the melt resulting in melt spallation to produce a hole in the DLM method. Two DLM methods were experimentally and theoretically demonstrated to test the hypothesis of the melt spallation by the effect of laser-generated pulse: one by introducing the ejection on the melt pool surface; another by introducing the ejection laser at the back solid surface material. It is shown in both the simulations and the experiments that the molten material is ejected close to the liquid-solid interface leaving behind a residual molten material along the bottom of the hole. This work provides strong evidence to prove the hypothesis that the material is ejected by the effect of the pressure pulse.

6 CONCLUSION AND RECOMMENDATIONS FOR FUTURE WORK

6.1 Conclusion

In this thesis, contributions have been made to the DLM method. Through studying the efficiency, quality characteristics and the mechanism of melt ejection. This chapter presents conclusions and key findings from these studies for each objective and outlines the contribution of this thesis to the knowledge of the DLM method. Limitations and recommendations for future work are also presented.

6.1.1 Objective 1 - To construct a theoretical model of laser micromachining by i) vaporisation (ablation) and ii) the combined melting and ejection in DLM method, initially neglecting the effects of heat loss to the HAZ using a one-dimensional conduction model.

In Chapters 3 a contribution has been made through presenting an analysis of the energy model for the DLM method. Theoretical calculations derived from a one-dimensional heating model were performed for the melt pool size against the melting process. In theory, the minimum required energy to remove the molten material was calculated from the surface energy at the liquid-solid interface that separates the liquid and creates new surfaces. It was found the energy necessary to eject the molten material can be considered to be negligible in comparison to the energy required to form the same mass of melt pool. Therefore, the energy model was focused on the melting process to optimise DLM energy. The key finding was that the most efficient melting occurs at the maximum melt depth when the surface starts vaporises. This was calculated for 316 stainless steel at absorbed laser irradiance of 13 kW/cm^2 to be melt depth of approximately 85 μm and a melting time of 15 ms. At this most efficient melting process, the theoretical calculation showed that there would be a reduction in total energy consumption of three times comparing DLM to conventional vaporisation that is in practice has been shown are at best 16 % efficient (Leitz *et al.*, 2011).

6.1.2 Objective 2 - To demonstrate and compare the relative energy efficiency of DLM method and laser ablation through experimentation and comparison to findings published in the literature.

The work in Chapter 4 is a combined analysis of experimental data of DLM method with the energy model from Chapters 3. Two lasers were used in the DLM work, a continuous wave

laser (fibre laser) to create a molten pool with melt depths from 8 to 31 μm, while a nanosecond pulse laser (Nd:YAG laser) was used to eject the molten material by vaporising the molten pool surface to generate recoil pressure. The Chapter presented results of surface treatment using the melting laser only, ejection laser only and both lasers combined in the DLM method. The experimental melt depths of the melting laser only were compared with the theoretical calculations. The experimental melt data align with the theoretical calculation at low melting time values. However, after that, the experimental results depart significantly from the linear theoretical trend when the melt pool depth increases beyond 20 μm at 9 ms melting time. This 9 ms was found to be the most efficient experimental melting time, however, it is less than the theoretical melting time of 15 ms. It is noted that melting model is a one-dimensional model of uniform heating and heat transfer is affected only by conduction that ignores the flow generated by surface tension driven convection known as the Marangoni effect, with a small contribution from the buoyancy force (Basu and DebRoy, 1992) and more efficient heat transfers the heat from the centre to the edge. The DLM method created holes with 18-28 μm maximum depth from 20-31 μm maximum melt depths at melting times in the range of 9-60 ms at the same order. At the optimised 9 ms melting time, of the total energy, 95% of the energy was delivered in the melting process and 5% in the ejection. The key finding from this result is that a good agreement was found between the experimental results with the theoretical calculation that predicted negligible energy required from ejection laser. The DLM results of this work were compared to conventional laser processing found in the literature. The results showed that the method presented can increase material removal efficiency compared with the conventional processes by approximately 2 to 6 times. This comparison confirms the theoretical reduction in total energy consumption of 3 times comparing DLM to vaporisation machining.

6.1.3 Objective 3 - To assess the quality of the DLM method using metallurgical techniques to show the effect of DLM on the machined workpiece.

This thesis presented in Chapter 4 an analysis of the geometry and metallurgical features via sectioning and imaging of the DLM holes. Analysis of the material quality shows that were found free from microcracks and with a small amount of redeposited material at the workpiece surface along the periphery of the created hole. Moreover, the micrographs show low porosity in the solidified molten material.

6.1.4 Objective 4 - To investigate the physical mechanism for the melt ejection through theoretical analysis and experimental results to provide insight into this mechanism.

Sectioning of the melt pool and machined workpiece features provides some useful insight into the ejection mechanism. The pulsed laser applied on the molten pool surface in the DLM method resulted in an ejection of approximately 90% of the molten material for melt depth of 20 μm at the optimised melting time of 9 ms. It was found in the DLM results an increase in the residual (non-ejected) molten material as melt depth increases. In addition, the DLM results showed that the molten material is ejected even when the nanosecond laser covers the entire molten pool surface and the recoil pressure confines the melt flow to the sides that is consistent with Fox's experiment and a recent study by Yuan et al., (2018). This finding led to the study of the melt ejection mechanism presented in Chapter 5. A high-speed camera was used to show the behaviour of the ejected melt material.

It was hypothesised in this research that the material is ejected by the effect of the acoustic compression pulse generated at the surface and travelled through the target material. This pulse is converted into a tensile pulse at a certain position inside the melt pool as a result of mismatching from high to low impedance during travelling inside the material. Upon this tensile pulse, spallation can occur and eject the molten material and takes place when the tensile stress exceeds the tensile strength of liquid material. The spallation of a laser-melted material by nanosecond laser pulse was studied experimentally and theoretically to find the magnitude and position of the tensile stress. DLM methods were experimentally and theoretically demonstrated in different setup regimes to test this hypothesis. The key finding is that both the simulations and experiments showed the molten material is ejected close to the liquid-solid interface leaving behind a residual molten material along the bottom of the hole. This work proves the hypothesis that the molten material is ejected by the effect of the tensile pulse generated inside the melt pool.

6.1.5 Contributions to the Knowledge

The main contributions of this research thesis are:

1. Even though previous studies of the DLM method showed improvement in the material removal efficiency, these studied ignored the energy consumed to produce the melt pool that is the major part of the required energy budget in DLM. This melting part can increase more material removal efficiency if it is carefully studied and optimised. In this thesis, a theoretical model of energy use during the melting

process part in DLM method has been developed. This model optimises the melting process and accordingly increases the efficiency of the DLM method.

2. Increasing the material removal efficiency using DLM experiment compared with conventional laser micromachining found in the literature.
3. Assessment of the quality of the DLM method using metallurgical techniques to show the effect of DLM on the machined workpiece.
4. The existing models of melt ejection mechanism from the literature contradict experimental work both in the literature and the experiments conducted in this thesis. In this thesis, it has been discovered that the molten material is removed by the effect of the tensile stress generated inside the melt pool that exceeds the tensile strength of the material resulting in melt spallation. The melt ejection mechanism advanced in this study represents an entirely novel contribution to the field.

This thesis makes a significant contribution to the knowledge of the field of the melt ejection process in the laser micromachining using the DLM method. The DLM efficiency has been increased through carefully choosing the melting process parameters. The melt ejection mechanism has been discovered. From industrial relevance, it is required further analysis in the melt ejection mechanism for drilling process using DLM method to show its applicability. However, these important findings give a better understanding of the DLM method and open the research for further investigations.

6.2 Recommendations for Future Work

This research, along with its many advantages, has certain limitations too. The following are some of the limitations faced and some recommendations for future work.

- Studying the effect of DLM on the quality of the machined material using other types of metals that can show the HAZ like low carbon steel. In this research, 316 stainless steel was used as a metal example. This alloy is an engineering material with many applications in the industry with an increase in the use of laser machining (Baddoo, 2008). This material was chosen due to the available research on stainless steel that makes suitable comparisons to literature works on conventional laser processing efficiency (Herfurth *et al.*, 2007; Gay *et al.*, 2009; Leitz *et al.*, 2011). In addition, stainless steel is well known thermophysical properties that are needed in the theoretical calculation. However, this stainless steel is austenitic that is not

transformable (Pouranvari and Marashi, 2009) accordingly no phase transformation can be observed in the HAZ that was used in the analysis as a quality indicator.

- Investigating the spallation process using a velocity interferometer system for any reflector (VISAR) system. This system is able to measure accurately the velocity of the sample surface (Hollenbach, 1972) that can be used to determine the pressure magnitude. It was very difficult to use this system in the limited space inside the laser machine cabinet. Therefore, it is recommended to use this process for more investigation in the spallation process by measuring the pressure and the spallation time from the ejection laser starts. Measuring the time is important as the analysis in Chapter 5 that shows the theoretical time of spallation depends on the melt depth.
- Studying the effect of the pulse duration time, pulse shape and pulse energy on the spallation process. The ND: YAG ejection laser was limited by one pulse duration time, Gaussian pulse shape and a small range of pulse energy. The pulse time is important in determining the spall zone. Shorter pulse makes the spallation near the free surface while longer pulse makes the spallation closer to the liquid-solid interface. DLM method showed ejection with residual molten martial inside the hole. If the pulse takes the square shape with flexible pulse duration time, it can be calculated to choose the pulse duration time for a certain melt depth to make the spallation exactly on the liquid-solid interface to remove the molten material without any residual. This increases more the DLM method efficiency. Wide range of pressure from ejection laser allows for more investigation of the spallation process for the same pulse duration time by lowering the pressure that results in a tensile pulse inside the liquid less than the material spall strength.

References:

Ahn, D., Seo, C. and Kim, D. (2012) 'Removal of metals and ceramics by combined effects of micro liquid jet and laser pulse', *Journal of Applied Physics*, 112(12). doi: 10.1063/1.4772614.

Von Allmen, M. (1976) 'Laser Drilling Velocity in Metals', *Journal of Applied Physics*, 47(12), pp. 5460–5463. doi: 10.1063/1.322578.

Baddoo, N. R. (2008) 'Stainless steel in construction: A review of research, applications, challenges and opportunities', *Journal of Constructional Steel Research*, 64(11), pp. 1199–1206. doi: 10.1016/j.jcsr.2008.07.011.

Basu, S. and DebRoy, T. (1992) 'Liquid metal expulsion during laser irradiation', *Journal of Applied Physics*, 72(8), pp. 3317–3322. doi: 10.1063/1.351452.

Behera, R. R. and Sankar, M. R. (2015) 'State of the Art on Under Liquid Laser Beam Machining', *Materials Today: Proceedings*, 2(4–5), pp. 1731–1740. doi: 10.1016/j.matpr.2015.07.007.

Bergstrom, D., Powell, J. and Kaplan, A. F. H. (2007) 'The absorptance of steels to Nd : YLF and Nd : YAG laser light at room temperature', *Applied Surface Science*, 253(11), pp. 5017–5028. doi: DOI 10.1016/j.apsusc.2006.11.018.

Bertolottl, M. and Concetta, S. (1981) 'Depth and velocity of the laser-melted front from an analytical solution of the heat conduction equation', *IEEE Journal of Quantum Electronics*, 17(10), pp. 1980–1989.

Brown, M.S. and Arnold, C.B., 2010. Laser precision microfabrication. *Springer Ser. Mater. Sci*, *135*(0933-03391), p.120.

Chan, C. L. and Mazumder, J. (1987) 'One-dimensional steady-state model for damage by vaporization and liquid expulsion due to laser-material interaction', *Journal of Applied Physics*, 62(11), pp. 4579–4586. doi: 10.1063/1.339053.

Chang, J. J. and Warnor, B. E. (1996) 'Laser-Plasma Interaction During Visible-Laser Ablation of Methods (Vol 69, Pg 473, 1996)', *Applied Physics Letters*, 69(15), p. 2298.

Chawla, T.C., Graff, D.L., Borg, R.C., Bordner, G.L., Weber, D.P. and Miller, D., 1981. Thermophysical properties of mixed oxide fuel and stainless steel type 316 for use in transition phase analysis. *Nuclear engineering and design*, *67*(1), pp.57-74.

Cheng, J., Liu, C.S., Shang, S., Liu, D., Perrie, W., Dearden, G. and Watkins, K., 2013. A review of ultrafast laser materials micromachining. *Optics & Laser Technology*, *46*, pp.88-102.

Choubey, A., Jain, R.K., Ali, S., Singh, R., Vishwakarma, S.C., Agrawal, D.K., Arya, R., Kaul, R., Upadhyaya, B.N. and Oak, S.M., 2015. Studies on pulsed Nd: YAG laser cutting of thick stainless steel in dry air and underwater environment for dismantling applications. *Optics & Laser Technology*, *71*, pp.6-15.

Ciurana, J., Arias, G. and Ozel, T. (2009) 'Neural network modeling and particle swarm optimization (PSO) of process parameters in pulsed laser micromachining of hardened AISI H13 steel', *Materials and Manufacturing Processes*, 24(3), pp. 358–368. doi: 10.1080/10426910802679568.

Cline, H. E. and Anthony, T. R. (1977) 'Heat treating and melting material with a scanning laser or electron beam', *Journal of Applied Physics*, 48(9), pp. 3895–3900. doi: 10.1063/1.324261.

Cohen, M. I. (1967) 'Melting of a half-space subjected to a constant heat input', *J. Franklin Inst.*, 283(4), pp. 271–285.

Dahotre, N. B. and Harimkar, S. (2008) *Laser Fabrication and Machining of Materials*. New York, NY: Springer.

Dhar, S., Saini, N. and Purohit, R. (2006) 'A review on laser drilling and its Techniques', in *International Conference on Advances in Mechanical Engineering*.

Dubey, A. K. and Yadava, V. (2008) 'Laser beam machining-A review', *International Journal of Machine Tools and Manufacture*, 48(6), pp. 609–628. doi: 10.1016/j.ijmachtools.2007.10.017.

Farooq, K. and Kar, A. (1998) 'Removal of laser-melted material with an assist gas', *Journal of Applied Physics*, 83(12), pp. 7467–7473. doi: 10.1063/1.367509.

Fleischer, J., Masuzawa, T.S.J.K.M., Schmidt, J. and Knoll, M., 2004. New applications for micro-EDM. *Journal of Materials Processing Technology*, *149*(1-3), pp.246-249.

Fox, J. A. (1975) 'A method for improving continuous wave laser penetration of metal targets', *Applied Physics Letters*, 26(12), pp. 682–684. doi: 10.1063/1.88024.

French, P.W., Naeem, M., Sharp, M. and Watkins, K.G., 2006, October. Investigation into

the influence of pulse shaping on drilling efficiency. In *International Congress on Applications of Lasers & Electro-Optics* (Vol. 2006, No. 1, p. 310). Laser Institute of America.

Fu, C. H., Liu, J. F. and Guo, A. (2015) 'Statistical characteristics of surface integrity by fiber laser cutting of Nitinol vascular stents', *Applied Surface Science*, 353, pp. 291–299. doi: 10.1016/j.apsusc.2015.06.105.

Gay, D., Cournoyer, A., Deladurantaye, P., Briand, M., Roy, V., Labranche, B., Levesque, M. and Taillon, Y., 2009, August. Micro-milling process improvement using an agile pulse-shaping fiber laser. In *Photonics North 2009* (Vol. 7386, p. 73860R). International Society for Optics and Photonics.

Genna, S., Leone, C., Lopresto, V., Santo, L. and Trovalusci, F., 2010. Study of fibre laser machining of C45 steel: influence of process parameters on material removal rate and roughness. *International Journal of Material Forming*, *3*(1), pp.1115-1118.

Ghany, K. A. and Newishy, M. (2005) 'Cutting of 1.2 mm thick austenitic stainless steel sheet using pulsed and CW Nd:YAG laser', *Journal of Materials Processing Technology*, 168(3), pp. 438–447. doi: 10.1016/j.jmatprotec.2005.02.251.

Ghany, K. A., Rafea, H. A. and Newishy, M. (2006) 'Using a Nd:YAG laser and six axes robot to cut zinc-coated steel', *International Journal of Advanced Manufacturing Technology*, 28(11–12), pp. 1111–1117. doi: 10.1007/s00170-004-2468-x.

Gower, M. C. (2000) 'Industrial applications of laser micromachining', *OPTICS EXPRESS*, 7(2), pp. 56–67. doi: 10.2351/1.5065770.

Le Harzic, R., Breitling, D., Weikert, M., Sommer, S., Föhl, C., Valette, S., Donnet, C., Audouard, E. and Dausinger, F., 2005. Pulse width and energy influence on laser micromachining of metals in a range of 100 fs to 5 ps. *Applied Surface Science*, *249*(1-4), pp.322-331.

Herfurth, H., Patwa, R., Lauterborn, T., Heinemann, S. and Pantsar, H., 2007, October. Micromachining with tailored nanosecond pulses. In *Photonics North 2007* (Vol. 6796, p. 67961G). International Society for Optics and Photonics.

Hollenbach, L. M. B. and R. E. (1972) 'Laser interferometer for measuring high velocities of any reflecting surface', *Journal of Applied Physics*, 43(11), pp. 4669–4675. doi: 10.1063/1.1660986.

Johnson, P. . and Christy, R. . (1974) ‘Optical constants of transition metals’, *Physical Review B*, 9(12), pp. 5056–5070. doi: 10.1103/PhysRevB.9.5056.

Kang, H. W., Lee, H. and Welch, A. J. (2008) ‘Laser ablation in a liquid-confined environment using a nanosecond laser pulse’, *Journal of Applied Physics*, 103(8). doi: 10.1063/1.2905314.

Kim, S., Kim, B.H., Shin, H.S. and Chu, C.N., 2009. Hybrid micromachining using a nanosecond pulsed laser and micro EDM. *Journal of micromechanics and microengineering*, *20*(1), p.015037.

Knight, C. J. (1979) ‘Theoretical Modeling of Rapid Surface Vaporization with Back Pressure’, *AIAA Journal*, 17(5), pp. 519–523. doi: 10.2514/3.61164.

Kray, D., Hopman, S., Spiegel, A., Richerzhagen, B. and Willeke, G.P., 2007. Study on the edge isolation of industrial silicon solar cells with waterjet-guided laser. *Solar Energy Materials and Solar Cells*, *91*(17), pp.1638-1644.

Krstulović, N., Shannon, S., Stefanuik, R. and Fanara, C., 2013. Underwater-laser drilling of aluminum. *The International Journal of Advanced Manufacturing Technology*, *69*(5-8), pp.1765-1773.

Kruusing, A. (2004) ‘Underwater and water-assisted laser processing: Part 1 - General features, steam cleaning and shock processing’, *Optics and Lasers in Engineering*, 41(2), pp. 307–327. doi: 10.1016/S0143-8166(02)00142-2.

Lehane, C. and Kwok, H. S. S. (2001) ‘Enhanced drilling using a dual-pulse Nd:YAG laser’, *Applied Physics A: Materials Science and Processing*, 73(1), pp. 45–48. doi: 10.1007/s003390100819.

Leibowitz, L., Chang, E.C., Chasanov, M.G., Gibby, R.L., Kim, C., Millunzi, A.C. and Stahl, D. (1976) *Properties for LMFBR safety analysis*.

Leitz, K.H., Redlingshöfer, B., Reg, Y., Otto, A. and Schmidt, M., 2011. Metal ablation with short and ultrashort laser pulses. *Physics Procedia*, *12*, pp.230-238.

De Rességuier, T., Lescoute, E., Signor, L., Loison, D., Dragon, A., Boustie, M., Cuq-Lelandais, J.P. and Berthe, L., 2010. Laser shock experiments to investigate and to model various aspects of the response of metals to shock loading. In *EPJ Web of Conferences* (Vol. 10, p. 00023). EDP Sciences.

Li, C. F., Johnson, D. B. and Kovacevic, R. (2003) 'Modeling of waterjet guided laser grooving of silicon', *International Journal of Machine Tools and Manufacture*, 43(9), pp. 925–936. doi: 10.1016/S0890-6955(03)00063-4.

López, J.M.L., Bakrania, A., Coupland, J. and Marimuthu, S., 2016. Droplet assisted laser micromachining of hard ceramics. *Journal of the European Ceramic Society*, *36*(11), pp.2689-2694.

Low, D. K. Y., Li, L. and Byrd, P. J. (2001) 'The influence of temporal pulse train modulation during laser percussion drilling', *Optics and lasers in engineering*, 35(3), pp. 149–164.

Luo, S.N., An, Q., Germann, T.C. and Han, L.B., 2009. Shock-induced spall in solid and liquid Cu at extreme strain rates. *Journal of Applied Physics*, *106*(1), p.013502.

Lv, X., Pan, Y., Jia, Z., Li, Z. and Ni, X., 2018. Through-hole energy-density threshold of silicon induced by combined millisecond and nanosecond pulsed laser. *AIP Advances*, *8*(5), p.055025.

Madic, M. and Radovanovic, M. (2012) 'Analysis of the heat affected zone in CO2 laser cutting of stainless steel', *Thermal Science*, 16(suppl. 2), pp. 363–373. doi: 10.2298/TSCI120424175M.

Majumdar, J. D. and Manna, I. (2003) 'Laser processing of materials', in *Sadhana*, pp. 495–562. doi: 10.1109/isdrs.2001.984587.

Markcoons, D. J. W. and Voisey, K. T. (2018) 'An Investigation to Determine if the Laser Drilling Capabilities of a 2 kW Fibre Laser can be Enhanced Using Pulse Train Shaping', *Lasers in Engineering*, 39(0), pp. 17–33.

Mayer, A. E. and Mayer, P. N. (2015) 'Continuum model of tensile fracture of metal melts and its application to a problem of high-current electron irradiation of metals', *Journal of Applied Physics*, 118(3). doi: 10.1063/1.4926861.

Mazumder, J. (1991) 'Overview of melt dynamics in laser processing', *Optical Engineering*, 30(8), p. 1208. doi: 10.1117/12.55899.

McNally, C.A., Folkes, J. and Pashby, I.R., 2004. Laser drilling of cooling holes in aeroengines: state of the art and future challenges. *Materials Science and Technology*, *20*(7), pp.805-813.

Meijer, J. (2004) ‘Laser beam machining (LBM), state of the art and new opportunities’, *Journal of Materials Processing Technology*, 149(1–3), pp. 2–17. doi: 10.1016/j.jmatprotec.2004.02.003.

Metz, S.A., Hettche, L.R., Stegman, R.L. and Schriempf, J.T., 1975. Effect of beam intensity on target response to high− intensity pulsed CO2 laser radiation. *Journal of Applied Physics*, *46*(4), pp.1634-1642.

Mishra, S. and Yadava, V. (2015) ‘Laser Beam MicroMachining (LBMM) – A review’, *Optics and Lasers in Engineering*, 73, pp. 89–122. doi: 10.1016/j.optlaseng.2015.03.017.

Moshe, E., Eliezer, S., Henis, Z., Werdiger, M., Dekel, E., Horovitz, Y., Maman, S., Goldberg, I.B. and Eliezer, D., 2000. Experimental measurements of the strength of metals approaching the theoretical limit predicted by the equation of state. *Applied Physics Letters*, *76*(12), pp.1555-1557.

Muhammad, N., Whitehead, D., Boor, A. and Li, L., 2010. Comparison of dry and wet fibre laser profile cutting of thin 316L stainless steel tubes for medical device applications. *Journal of Materials Processing Technology*, *210*(15), pp.2261-2267.

Orazi, L., Cuccolini, G., Fortunato, A. and Tani, G., 2010. An automated procedure for material removal rate prediction in laser surface micromanufacturing. *The International Journal of Advanced Manufacturing Technology*, *46*(1-4), pp.163-171.

Petkov, P.V., Dimov, S.S., Minev, R.M. and Pham, D.T., 2008. Laser milling: pulse duration effects on surface integrity. *Proceedings of the Institution of Mechanical Engineers, Part B: Journal of Engineering Manufacture*, *222*(1), pp.35-45.

Pham, D.T., Dimov, S.S., Petkov, P.V. and Petkov, S.P., 2002. Laser milling. *Proceedings of the Institution of Mechanical Engineers, Part B: Journal of Engineering Manufacture*, *216*(5), pp.657-667.

Phipps Jr, C.R., Turner, T.P., Harrison, R.F., York, G.W., Osborne, W.Z., Anderson, G.K., Corlis, X.F., Haynes, L.C., Steele, H.S., Spicochi, K.C. and King, T.R., 1988. Impulse coupling to targets in vacuum by KrF, HF, and CO2 single-pulse lasers. *Journal of Applied Physics*, *64*(3), pp.1083-1096.

Pouranvari, M. and Marashi, S. P. H. (2009) ‘Similar and dissimilar RSW of low carbon and austenitic stainless steels: effect of weld microstructure and hardness profile on failure mode’, *Materials Science and Technology*, 25(12), pp. 1411–1416. doi:

10.1179/026708309x12459430509292.

Povarnitsyn, M.E., Itina, T.E., Sentis, M., Khishchenko, K.V. and Levashov, P.R., 2007. Material decomposition mechanisms in femtosecond laser interactions with metals. *Physical Review B*, *75*(23), p.235414.

Richerzhagen, B., Kutsuna, M., Okada, H. and Ikeda, T., 2003, February. Water-jet-guided laser processing. In *Third International Symposium on Laser Precision Microfabrication* (Vol. 4830, pp. 91-94). International Society for Optics and Photonics.

Rizvi, N. H. and Apte, P. (2002) 'Developments in laser micro-machining techniques', *Journal of Materials Processing Technology*, 127(2), pp. 206–210. doi: 10.1016/S0924-0136(02)00143-7.

Robin, J. E. and Nordin, P. (1976) 'Improved cw laser penetration of solids using a superimposed pulsed laser', *Applied Physics Letters*, 29(1), pp. 3–5. doi: 10.1063/1.88864.

De Rességuier, T., Signor, L., Dragon, A., Boustie, M., Roy, G. and Llorca, F., 2007. Experimental investigation of liquid spall in laser shock-loaded tin. *Journal of applied physics*, *101*(1), p.013506.

Russel L. McCally (1984) 'McCally.pdf', *Applied optics*, 23(14), p. 2227.

Sarfraz, S., Shehab, E., Salonitis, K., Suder, W. and Sajid, M., 2018, July. Towards cost modelling for laser drilling process. In *Proceedings of the 25th ISPE Inc. International Conference on Transdisciplinary Engineering, Modena, Italy* (pp. 3-6).

Sheng, P. S. and Joshi, V. S. (1995) 'Analysis of heat-affected zone formation for laser cutting of stainless steel', *Journal of Materials Processing Technology*, 53(3–4), pp. 879–892. doi: 10.1016/0924-0136(94)01761-O.

Shui, V. H. (1978) 'Effect of induced pressure and impulse on cw laser penetration of solids', *Physics of Fluids*, 21(12), pp. 2174–2178. doi: 10.1063/1.862175.

Grigoryev, S.Y., Lakatosh, B.V., Krivokorytov, M.S., Zhakhovsky, V.V., Dyachkov, S.A., Ilnitsky, D.K., Migdal, K.P., Inogamov, N.A., Vinokhodov, A.Y., Kompanets, V.O. and Sidelnikov, Y.V., 2018. Expansion and fragmentation of a liquid-metal droplet by a short laser pulse. *Physical Review Applied*, *10*(6), p.064009.

Silvennoinen, M., Kaakkunen, J.J.J., Paivasaari, K. and Vahimaa, P., 2013. Water spray assisted ultrashort laser pulse ablation. *Applied surface science*, *265*, pp.865-869.

Solana, P., Kapadia, P., Dowden, J., Rodden, W.S., Kudesia, S.S., Hand, D.P. and Jones, J.D., 2001. Time dependent ablation and liquid ejection processes during the laser drilling of metals. *Optics Communications*, *191*(1-2), pp.97-112.

Indhu, R., Vivek, V., Sarathkumar, L., Bharatish, A. and Soundarapandian, S., 2018. Overview of Laser Absorptivity Measurement Techniques for Material Processing. *Lasers in Manufacturing and Materials Processing*, *5*(4), pp.458-481.

Steen, W. M. and Mazumder, J. (2010) *Laser Material Processing*. 4th edn. New York: springer science & business media. doi: 10.1007/978-1-84996-062-5.

Struleva, E.V., Ashitkov, S.I., Komarov, P.S., Khishchenko, K.V. and Agranat, M.B., 2016, November. Strength of iron melt at high extension rate during femtosecond laser ablation. In *J. Phys. Conf. Ser* (Vol. 774, p. 012098).

Su, Y., Li, Z. and Mills, K. C. (2005) 'Equation to estimate the surface tensions of stainless steels', *Journal of Materials Science*, 40(9–10), pp. 2201–2205. doi: 10.1007/s10853-005-1933-8.

Sun, Z. and Ion, J. C. (1995) 'Laser welding of dissimilar metal combinations', *Journal of Materials Science*, 30(17), pp. 4205–4214. doi: 10.1007/BF00361499.

Swinehart, D. F. (1962) 'The Beer-Lambert law', *Journal of Chemical Education*, 39(7), pp. 333–335. doi: 10.1021/ed039p333.

Tangwarodomnukun, V., Wang, J., Huang, C.Z. and Zhu, H.T., 2014. Heating and material removal process in hybrid laser-waterjet ablation of silicon substrates. *International Journal of Machine Tools and Manufacture*, *79*, pp.1-16.

Teixidor, D., Ferrer, I., Ciurana, J. and Özel, T., 2013. Optimization of process parameters for pulsed laser milling of micro-channels on AISI H13 tool steel. *Robotics and Computer-Integrated Manufacturing*, *29*(1), pp.209-218.

Thompson, K. P., Ren, Q. S. and Parel, J. (1992) 'Therapeutic and Diagnostic Application of Lasers in Ophthalmology', *Proceedings of the IEEE*, 80(6), pp. 836–860.

Treusch, H. G. and Herziger, G. (1986) 'Metal Precision Drilling with Lasers', *High Power Lasers and Their Industrial Applications*, 0650(October 1986), p. 220. doi: 10.1117/12.938103.

Venkatesan, K., Ramanujam, R. and Kuppan, P. (2014) 'Laser Assisted Machining of

difficult to cut materials : Research Opportunities and Future Directions - A comprehensive review', *Procedia Engineering*. Elsevier B.V., 97, pp. 1626–1636. doi: 10.1016/j.proeng.2014.12.313.

Voisey, K.T., Kudesia, S.S., Rodden, W.S.O., Hand, D.P., Jones, J.D.C. and Clyne, T.W., 2003. Melt ejection during laser drilling of metals. *Materials Science and Engineering: A*, *356*(1-2), pp.414-424.

Walther, K., Brajdic, M. and Kreutz, E. W. (2008) 'Enhanced processing speed in laser drilling of stainless steel by spatially and temporally superposed pulsed Nd:YAG laser radiation', *International Journal of Advanced Manufacturing Technology*, 35(9–10), pp. 895–899. doi: 10.1007/s00170-006-0768-z.

Wang, Z., Qin, Y., Yang, S., Shi, B., Wang, H. and Chen, H., 2017, May. Material removal during double-pulsed (ms and ns) laser drilling. In *Fourth International Symposium on Laser Interaction with Matter* (Vol. 10173, p. 1017324). International Society for Optics and Photonics.

Weiss, B. and Stickler, R. (2007) 'Phase instabilities during high temperature exposure of 316 austenitic stainless steel', *Metallurgical and Materials Transactions B*, 3(4), pp. 851–866. doi: 10.1007/bf02647659.

Xie, J., Kar, A., Rothenflue, J.A. and Latham, W.P., 1997. Temperature-dependent absorptivity and cutting capability of CO2, Nd: YAG and chemical oxygen–iodine lasers. *Journal of Laser Applications*, *9*(2), pp.77-85.

Xu, X. (2002) 'Phase explosion and its time lag in nanosecond laser ablation', in *Applied Surface Science*, pp. 61–66. doi: 10.1016/S0169-4332(02)00304-5.

Yilbas, B. S., Davies, R. and Yilbas, Z. (1992) 'Study into penetration speed during CO2 laser cutting of stainless steel', *Optics and Lasers in Engineering*, 17(2), pp. 69–82. doi: 10.1016/0143-8166(92)90013-W.

Yuan, B.S., Zhang, Y., Zhang, W., Dong, Y. and Jin, G.Y., 2018. The effect of spot size combination mode on ablation morphology of aluminum alloy by millisecond-nanosecond combined-pulse laser. *Materials*, *11*(8), p.1419.

Zhang, J.H., Lee, T.C., Ai, X. and Lau, W.S., 1996. Investigation of the surface integrity of laser-cut ceramic. *Journal of materials processing technology*, *57*(3-4), pp.304-310.

Zhang, Y. and Faghri, A. (1999) ‘Vaporization, melting and heat conduction in the laser drilling process’, *International Journal of Heat and Mass Transfer*, 42(10), pp. 1775–1790. doi: 10.1016/S0017-9310(98)00268-3.